主論文

Study of Parity Violation in Neutron Resonance Reactions in Nuclei

Yasuyuki Matsuda

A dissertation submitted in partial fulfillment of
the requirements for the degree of

Doctor of Science

Department of Physics
Faculty of Science
Kyoto University

Abstract

In order to study the origin of large enhancement of the parity violation effect in neutron resonance absorption reactions, the longitudinal asymmetries in p-wave resonances have been measured for ^{121}Sb, ^{123}Sb and ^{127}I at LANSCE in the energy region of 1eV to 350eV.

We constructed a polarized proton filter for polarizing the neutron beam, a spin flipper to reverse the direction of neutron spin and a neutron detector which consisted of liquid scintillator arrays. A new computer code which uses multi-level formula to calculate the neutron cross sections and employs response functions of our experimental apparatus has been developed and used for the analysis of the experimental data.

We have found that five of seventeen p-wave resonances in ^{121}Sb, one of five p-wave resonances in ^{123}Sb and seven of twenty p-wave resonances in ^{127}I have asymmetries which have statistical significance greater than 3σ. The signs of the asymmetries have been found to be random.

The experiment shows that the large enhancement of parity violating effect is not the phenomena only for few resonances but is a prevalent feature of p-wave resonances.

Based on the statistical view of the compound nucleus, the weak matrix element has been treated as a random variable according to a Gaussian distribution with the variance M^2. The weak spreading width $\Gamma_W = 2\pi M^2/D$, where D is the level density of the nuclei, has been determined from the experimental values of asymmetries. The obtained values of Γ_W for ^{121}Sb, ^{123}Sb and ^{127}I are $6.45^{+9.72}_{-3.66} \times 10^{-7}$eV, $1.23^{+15.0}_{-0.96} \times 10^{-7}$eV, and $2.05^{+1.94}_{-0.93} \times 10^{-7}$eV respectively. These values as well as the ones obtained from the other TRIPLE data are consistent with each other, and agree with estimated value based on the statistical view. This agreement as well as observed randomness of the signs of asymmetries makes the statistical treatment of weak matrix element convincing.

Contents

Chapter 1

Introduction

Parity is a discrete symmetry involving the spatial reflection of the coordinates at the origin. When the physical system is invariant under spatial reflection, parity is conserved.

Parity conservation had been regarded as a universal law until mid-1950s. In 1957, Wu et al. found evidence of parity violation in β decay of ^{60}Co[1]. Following experiments showed the fact that parity violation is a characteristic nature of the weak interaction, while parity is conserved in the strong and electromagnetic interactions.

The weak interaction and the electromagnetic interaction are unified in the "standard theory" and are described by the exchange of weak vector bosons, $W^{\pm}$ and Z^0, and the photons. $W^{\pm}$ carries the weak charged current, while Z^0 carries the weak neutral current.

Various experiments concerning leptonic and semi-leptonic weak interactions have been carried out, and the standard model has been confirmed. On the other hand, the nature of the hadronic weak interaction still remains obscure. The flavor conserving ($\Delta S = 0$) sector of the hadronic weak interaction is important for understanding the weak interaction because the weak neutral current between quarks can be studied only in this sector. The nucleon-nucleon interaction is the most suitable channel to study it. However, it is not easy to carry out such experiments because of the existence of strong interaction.

Since the Compton wavelength of the weak boson is extremely short compared to the distance between nucleons, direct exchange of the weak boson between nucleons is greatly suppressed. Therefore the weak interaction between nucleons is mainly

represented in terms of exchange of mesons(π, ρ, ω) ,in which one meson-nucleon vertex is weak and parity violating while the other vertex is strong and parity conserving. In this view, the weak meson-nucleon-nucleon coupling constants represent all of the characteristics of hadronic weak interaction.

Theoretical calculation of the weak coupling constants on the basis of the standard theory has been investigated by many theoreticians. Following the pioneering works by Michel[2], McKellar et al.[3] and Konuma et al.[4], the first comprehensive calculation was done by Desplanques, Donoghue and Holstein (DDH) in 1980[5]. They parameterized 7 weak coupling constants and predicted the "best value"s. Since then, several models [6][7][8][9][10] have been proposed to calculate the weak coupling constants in different approaches. Some of the results of these calculations are different from each other by one order of magnitude.

In order to study the hadronic weak interaction, several parity nonconserving(PNC) observables in hadronic reactions shown below have been measured experimentally:

- longitudinal asymmetry A_L which is the difference of the cross sections with incident positive- and negative- helicity particles, divided by the sum of the cross sections.
- the asymmetry A_γ of the γ-rays emitted in the radiative capture reaction with respect to the spin of the incident particle.
- the circular polarization P_γ of the γ-rays emitted from unpolarized nuclei.
- the spin rotation $d\phi/dz$ of the transversely polarized incident particle in the target material.

Since the PNC observables in the nucleon-nucleon interactions can be calculated directly in terms of weak coupling constants, such experiments give the simplest way to study weak coupling constants. The PNC effect in the nucleon-nucleon interaction is observed by Lobashov et al. for the first time[11]. In this experiment P_γ in the $\vec{n} + p \rightarrow d + \gamma$ reaction was measured. Potter et al. succeeded in measuring A_L in the proton-proton scattering reaction[12].

Table 1.1 summarizes recent experimental results on A_L, A_γ and P_γ in nucleon-nucleon interactions.

Reaction channel	PNC observable	Asymmetry	Reference
$p+p \rightarrow p+p$	A_L at 15MeV	$(-1.7 \pm 0.8)\times 10^{-7}$	[13]
	A_L at 45MeV	$(-2.31 \pm 0.89)\times 10^{-7}$	[14]
	A_L at 45MeV	$(-1.50 \pm 0.22)\times 10^{-7}$	[15]
	A_L at 800MeV	$(+2.4 \pm 1.1)\times 10^{-7}$	[16]
$n+p \rightarrow d+\gamma$	A_γ with cold neutron	$(-1.5 \pm 4.8)\times 10^{-8}$	[17]
	P_γ with cold neutron	$(1.8 \pm 1.8)\times 10^{-7}$	[18]

Table 1.1: Experimental results of PNC asymmetries in the N-N system

These asymmetries, which are of the order of 10^{-7}, are consistent with theoretical calculations, but the accuracies of these results are not sufficient to discriminate theoretical models.

The study of the PNC effect in light nuclei has been made by several groups. Most of the experiments deal special transitions involving close lying states which are relatively isolated and have opposite parities and same spin. These states are called parity doublets. The PNC interaction induces small parity admixture in the parity doublets, and the interference of the doublets produces PNC effects in the transition from the doublets to its decaying state.

The advantage of such experiments is in the enhancement of PNC effects due to small energy splitting of parity doublets and the difference of decay amplitudes. Typical energy splitting is $5 \sim 500$keV and $\sqrt{\Gamma_{PC}/\Gamma_{PNC}}$ is of the order of $10 \sim 100$, where Γ_{PC} and Γ_{PNC} are parity conserving and parity nonconserving decay widths respectively. The combined enhancement reaches about 10^3 so that PNC effects of order of 10^{-4} are observed. It is possible to calculate the weak coupling constant from these results, since only the doublet states and the state to which they decay must be taken in to account in these reactions.

Successful measurements of P_γ or A_γ with the nuclei ^{18}F[19][20], ^{19}F[21][22], and ^{21}Ne[23] were carried out in this context. The experimental results are shown in Table 1.2.

Concerning the weak interaction in heavy nuclei, Abov et al.[24] measured A_γ in the radiative neutron capture reaction of ^{113}Cd, and obtained as $A_\gamma = (-4.1 \pm$

PNC observable		Asymmetry	Reference
^{18}F	$P_\gamma(1081keV)$	$(1.7 \pm 5.8) \times 10^{-4}$	[19]
		$(2.7 \pm 5.7) \times 10^{-4}$	[20]
^{19}F	$A_\gamma(110keV)$	$(-8.5 \pm 2.6) \times 10^{-5}$	[21]
		$(-6.8 \pm 2.1) \times 10^{-5}$	[22]
^{21}Ne	$P_\gamma(2789keV)$	$(8 \pm 14) \times 10^{-4}$	[23]

Table 1.2: Experimental results of PNC asymmetries with light nuclei (see the text)

$0.8) \times 10^{-4}$ in 1964. Since then, several PNC measurements have been done with heavy nuclei. However the extraction of the weak coupling constant from these experiments is difficult because structures of heavy nuclei are so complicated that the calculation of wave functions involved in the reaction is impossible.

In 1980s, new light was shed on the study of parity violation in heavy nuclei. Alfimenkov et al. at Dubna[25] measured longitudinal asymmetries on p-wave resonances of several nuclei. They found a surprising large asymmetry at the 0.734-eV p-wave resonance in ^{139}La, that is, $A_L = (7.3 \pm 0.5) \times 10^{-2}$. A_L were also measured for several other nuclei, and found to be $(0.45 \pm 0.13) \times 10^{-2}$ for the 1.35-eV p-wave resonance of ^{117}Sn, $(2.4 \pm 0.4) \times 10^{-2}$ for the 0.88-eV p-wave resonance of ^{81}Br, and $(-0.82 \pm 0.22) \times 10^{-2}$ for the 4.53-eV p-wave resonance of ^{111}Cd [25]. They measured the helicity dependence of the cross section by detecting transmitted neutrons (transmission method). A KEK-Kyoto group measured A_L by means of the detection of γ-rays in radiative capture reactions (γ-ray detection method) and also by the transmission method. They obtained $(9.5 \pm 0.3) \times 10^{-2}$ for the 0.734-eV p-wave resonance of ^{139}La[26][27]. The discrepancy between the Dubna result and the KEK-Kyoto result was studied by Shimizu et al.[28] by measuring the angular dependence of A_L with γ-ray energy-threshold level of $1MeV$. They found that such angular dependence is consistent with zero within experimental errors, therefore the value obtained by the γ-ray detection method should be identical with the value obtained by the transmission method. The results of KEK-Kyoto group were confirmed by Bowman et al.[29] by the transmission method.

This enormously large PNC effect can be explained by the interference between p-wave and neighboring s-wave resonances ("s-p mixing") [30][31][32][33]. In this

model, the longitudinal asymmetry A_L at p-wave resonance is written as

$$A_L = \frac{2V_{sp}}{E_p - E_s}\sqrt{\frac{\Gamma_s}{\Gamma_p}}\sqrt{\frac{\Gamma_{p1/2}}{\Gamma_p}} \tag{1.1}$$

where Γ_s and Γ_p are the neutron widths of s-wave and p-wave resonances and E_s and E_p are corresponding resonance energies. $\Gamma_{p1/2}$ is the partial neutron width for incident neutron which have total angular momenta $j = 1/2$. V_{sp} is the matrix element of weak parity violating interaction between compound states. Very small energy splitting of two resonances (typically a few eV) and the large difference of neutron widths ($\sqrt{\Gamma_s/\Gamma_p} \sim 10^3$) give rise to the enhancement of the order of $10^5 \sim 10^6$. This model predicts that the large PNC effect can be found commonly in the neutron absorption reactions in the resonance regions of compound nuclei, and the signs of the asymmetries will be random.

The interest in these parity violation measurements has much increased because of the predictions[31][34] in which time-reversal invariant (TRI) violation is also enhanced at p-wave resonances. Stodolsky[35] proposed three configurations of the directions of the neutron spin and the target spin to search for P-odd T-odd terms in neutron transmission experiments. The advantage of the neutron transmission experiment is in the fact that we can study TRI violation free from final state interactions, because the incoming and outgoing particles are the same and have the same momentum.

The 0.734-eV resonance of ^{139}La, which has been found to have the largest asymmetry, is considered to be suitable for the TRI experiment. Intensive experimental efforts to polarize ^{139}La nuclei have been done. Recently Maekawa et al.[36] obtained about 20% polarization of ^{139}La in the Nd^{3+} doped $LaAlO_3$ crystal. Further improvements of the polarization have been tried in PSI[37].

In 1990, TRIPLE Collaboration measured asymmetries of p-wave resonances on ^{232}Th[38][39] and ^{238}U[40] targets, and reported "sign effect" of the asymmetry. All seven asymmetries in ^{232}Th were positive, and three of four asymmetries in ^{238}U were also positive. The tendency for the asymmetries to have the same sign is hardly understandable from the view point of the s-p mixing model which is based on the statistical nature of compound nuclei. Alternative mechanisms to explain the enhancement of parity violation giving the same sign have been proposed[41][42][43][44][45]. For understanding of this problem, more experimental studies are required.

An approach to study the nature of parity violation in p-wave resonances is to measure the angular correlations of γ-rays with respect to the direction of spin and momentum of the incident neutron[46][47]. Among them the correlation terms corresponding to $(\vec{\sigma}_n \cdot (\vec{k}_n \times \vec{k}_\gamma))$ and $(\vec{\sigma}_n \cdot \vec{k}_\gamma)$ are important, where σ_n is the spin of incident neutron, and k_n and k_γ denote the momentum of incident neutron and that of capture γ-rays respectively.

The terms corresponding to $(\vec{\sigma}_n \cdot (\vec{k}_n \times \vec{k}_\gamma))$ and $(\vec{\sigma}_n \cdot \vec{k}_\gamma)$ were studied by Matsuda et al. at the 0.734-eV p-wave resonance for ^{139}La target[48][49]. From these terms, we can extract the weak matrix element without ambiguity of the partial neutron width of the p-wave resonance. The preliminary result $|V_{sp}| = 3.3^{+6.4}_{-1.3}$meV is consistent with the expected value from the s-p mixing model. The same type of experiments were carried out also for ^{113}Cd[50] and ^{117}Sn[51].

Another approach is a statistical treatment of asymmetries of p-wave resonances based on the theory of compound nucleus.

From the viewpoint of the statistical model of the compound nucleus, the weak matrix elements are expected to be Gaussian random variables with zero mean. Measurements of asymmetries on many p-wave resonances of a nucleus give the distribution of the weak matrix elements, from which the variance of the distribution, M^2, can be extracted [52][53]. Then the weak spreading width Γ_W is defined as $\Gamma_W = 2\pi M^2/D$, where D is the average level spacing of the compound resonances. Based on the s-p mixing model, the value of Γ_W can be estimated to be of the order of 10^{-7}eV. More detailed studies have been done on the relation between the value of Γ_W or its mass dependence and the nature of parity violation in nuclei [54][55][56][57][58].

Therefore, it is very important to measure asymmetries of many resonances of various nuclei in the wide energy range with high statistics. Such experiments will answer the question if large asymmetries are commonly seen in p-wave resonances with random signs as the s-p mixing model predicts, or the "sign effect" is universal phenomena for various nuclei. From the measurement, the weak spreading width Γ_W can be determined for different nuclei. The comparison between Γ_W obtained from various nuclei and estimated ones based on the s-p mixing model is important to know whether the model is appropriate to describe parity violation in compound

nuclei. The study of mass dependence of Γ_W gives further information on parity violation in nuclei. The experimental determination of Γ_W is meaningful also for theoretical studies on the determination of weak coupling constant. In addition, such studies are important for foundation of the basis of future TRI tests.

The LANSCE facility[59][60] provides a long neutron flight path and a high-intensity pulsed neutron beam over wide energy range. We, TRIPLE Collaboration, took these advantages to measure PNC effects in many resonances of various nuclei with high statistics. The polarized proton filter which provides the neutron polarization of more than 80% in wide energy range[61], the high efficiency neutron spin flipper[62] and the neutron detector which can handle the counting rate of 500MHz [63] were newly constructed for the experiment.

Using these apparatus, we measured longitudinal asymmetries for the ^{232}Th, ^{238}U, ^{107}Ag, ^{109}Ag, ^{115}In and ^{113}Cd targets in 1993, and the ^{121}Sb, ^{123}Sb, ^{127}I, ^{131}Xe, ^{133}Cs, ^{106}Pd and ^{108}Pd targets in 1995. We chose nuclei in the mass regions of A ~100 and A ~230, in which we expected to find many p-wave resonances because of large p-wave strength function[64]. The measurements in different mass regions will give information regarding mass dependence of Γ_W.

The analysis of the data requires fitting the obtained neutron spectra with high accuracy. The analysis code which employs a multi-level cross section formula and proper response function of our beam line was developed for this experiment.

In this paper, we describe the detailed experimental procedure, analysis of data, and the results of the measurements on the target of ^{121}Sb, ^{123}Sb and ^{127}I nuclei. Then we discuss the statistical treatment of the parity violating asymmetries using the data on ^{121}Sb, ^{123}Sb and ^{127}I as well as other experimental data obtained by TRIPLE Collaboration.

The theoretical explanation for enhancement of parity violation is given in Chapter 2. The experimental procedure is presented in Chapter 3. The framework of the analysis is shown in Chapter 4. The analysis code developed for this experiment is described also in Chapter 4. Chapter 5 is devoted to the results of the experiment and discussion. The conclusion is given in Chapter 6.

Chapter 2

Theoretical Framework

The theoretical framework for this experiment is described in this chapter. In Section 2.1, the origin of the enhancement of parity violation in p-wave resonances is explained within the framework of the s-p mixing model. In Section 2.2, we introduce the weak spreading width Γ_W which is related to the strength of the weak interaction in nuclei.

2.1 Enhancement of the PNC Effect

Large parity violation observed in p-wave resonances is explained by interference between the p-wave and s-wave resonances (s-p mixing model) [30][31][32]. The longitudinal asymmetry P at a p-wave resonance is written as

$$\begin{aligned} P &\equiv \frac{\sigma_{p+} - \sigma_{p-}}{\sigma_{p+} + \sigma_{p-}} \\ &= \frac{2V_{sp}}{E_p - E_s}\sqrt{\frac{\Gamma_s}{\Gamma_p}}x, \end{aligned} \tag{2.1}$$

where σ_{p+} and σ_{p-} are the neutron cross sections of the p-wave resonance for helicity $+$ and $-$ states of incident neutrons. Γ_s and Γ_p are the neutron widths of s-wave and p-wave resonances. E_s and E_p are the resonance energies. $V_{sp} = \langle\Psi_s|H_W|\Psi_p\rangle$ is the matrix element of weak Hamiltonian H_W between compound states $|\Psi_s\rangle$ and $|\Psi_p\rangle$. x is defined as

$$x \equiv \sqrt{\frac{\Gamma_{p1/2}}{\Gamma_p}} = \sqrt{\frac{\Gamma_{p1/2}}{\Gamma_{p1/2} + \Gamma_{p3/2}}}, \tag{2.2}$$

where $\Gamma_{p1/2}$ and $\Gamma_{p3/2}$ are the partial neutron widths for total angular momenta of incident neutrons $j = 1/2$ and $j = 3/2$ respectively. For the nucleus whose spin is zero, x always equals unity.

Two kinds of enhancement mechanisms are considered to contribute to large magnitude of longitudinal asymmetries. One of them is the "dynamical enhancement " and the other is the "structural enhancement".

The "dynamical enhancement" originates in the statistical nature of the compound nuclei. The wave function of a compound state $|\Psi\rangle$ can be represented by a sum of many-particle excitation states $|\psi\rangle$ in the nuclear shell model as

$$|\Psi\rangle = \sum_i^N c_i|\psi_i\rangle, \tag{2.3}$$

where the magnitude of coefficient c_i is of the order of $1/\sqrt{N}$ as a result of the normalization of the wave function $|\Psi\rangle$. N is the number of the states contributing to a compound state, and is estimated as

$$N \sim \frac{\pi}{2}\frac{\Gamma_{spr}}{D}, \tag{2.4}$$

where D is the average level spacing between compound states. Γ_{spr} is the spreading width of the compound state and is approximately equal to the average level distance between single-particle levels. Typical values of Γ_{spr} ($\sim 3 \times 10^6$eV) and D ($\sim 3 \times 10$eV) make N to be the order of 10^5.

The weak matrix element V_{sp} can be written as

$$\begin{aligned} V_{sp} &= \langle \Psi_s | H_W | \Psi_p \rangle \\ &= \sum_{ij} c_i^* d_j \langle \psi_i | H_W | \psi_j \rangle. \end{aligned} \tag{2.5}$$

From the view point of the statistical model of the compound nucleus [65][66], the matrix element $\langle \psi_i | H_W | \psi_j \rangle$ is expected to be a random variable according to a Gaussian distribution with mean zero and variance $\langle H_W \rangle^2$. If we assume the weak Hamiltonian is a one-particle operator, the matrix element has a non-zero value only when ψ_j differs from ψ_i by the state of one particle, and has a zero value in other case. Therefore the number of summation in Equation (2.5) is of the order of N, not N^2.

Since V_{sp} is a sum of independent Gaussian-distributed random variables whose mean is zero, V_{sp} also obeys a Gaussian distribution with mean zero. Its variance M^2 is given as

$$\begin{aligned} M^2 &\equiv \overline{V_{sp}^2} \\ &= \sum_{ijkl} (c_i^* d_j \langle \psi_i | H_W | \psi_j \rangle)^* (c_k^* d_l \langle \psi_k | H_W | \psi_l \rangle) \\ &= \sum_{ij} (c_i c_i^*)(d_j^* d_j) |\langle \psi_i | H_W | \psi_j \rangle|^2 \\ &\quad + \sum_{i \neq k, j \neq l} (c_i^* c_j \langle \psi_i | H_W | \psi_j \rangle)^* (d_k^* d_l \langle \psi_k | H_W | \psi_l \rangle) \\ &\sim \frac{1}{N} \frac{1}{N} \langle H_W \rangle^2 \times N, \end{aligned} \tag{2.6}$$

$$M \sim \frac{1}{N} \langle H_W \rangle \times \sqrt{N}. \tag{2.7}$$

The magnitude of parity mixing between compound states is given as

$$\frac{M}{D} \sim \frac{\langle H_W \rangle}{\Gamma_{spr}} \times \sqrt{N}, \tag{2.8}$$

where $\langle H_W \rangle / \Gamma_{spr}$ is a typical magnitude of parity mixing between single particle states. This ratio is approximately the same as the ratio of the parity violating potential between nucleons and the parity conserving potential in the nucleus.

$\langle H_W \rangle / \Gamma_{spr}$ is estimated to be of the order of 10^{-7}. Equation (2.8) shows that the parity mixing between compound states is enhanced compared to the parity mixing between single particle states by $\sqrt{N}$. This enhancement is called "dynamical enhancement". A typical value of N, that is 10^5, gives enhancement of $10^2 \sim 10^3$.

The other enhancement factor, that is the "structural enhancement", comes from the ratio of the neutron widths of two compound states. Due to the centrifugal barrier, the neutron widths for s-wave and p-wave resonances are described as

$$\Gamma_s \propto kR, \qquad \Gamma_p \propto (kR)^3, \tag{2.9}$$

where k is the neutron momentum, and R is the radius of the nucleus. Therefore the "structural enhancement" is given as

$$\sqrt{\frac{\Gamma_s}{\Gamma_p}} \sim \frac{1}{kR}. \tag{2.10}$$

Typical values of $R \sim 10fm$ and $k \sim 10^{-3\sim4} fm^{-1}$ give the enhancement of the order of $10^2 \sim 10^3$.

The remaining factor in Equation (2.1), that is x, comes from the fact that only the $j = 1/2$ amplitude contributes to the longitudinal asymmetry[31]. It is necessary to determine x in order to obtain the weak matrix element V_{sp} for a specific pair of s- and p-wave resonances. Flambaum et al.[46] and Vanhoy et al.[47] showed that x can be determined from the measurement of the angular correlation of γ-rays at the p-wave resonance with polarized neutrons. Vanhoy et al.[67] showed that x can be obtained also by studying the PNC effect with a polarized target and unpolarized neutrons.

As noted above, the determination of x is important for studying the weak matrix element at a specific p-wave resonance. However, from the view point of the statistical model, the variance of the distribution of weak matrix elements M^2 or the weak spreading width Γ_W defined in following section is essential to investigate the nature of the weak Hamiltonian in the compound nucleus.

In this experiment, we have determined Γ_W by measuring asymmetries in many p-wave resonances in various nuclei in order to find the dependence of Γ_W upon the nuclei. The method used to extract Γ_W from the experimental data will be given in Section 4.2.

2.2 Weak Spreading Width

The weak spreading width Γ_W is defined as $\Gamma_W \equiv 2\pi M^2/D$ where M^2 is the variance of the weak matrix element described in Section 2.1, and D is the level spacing of compound states. Using Equation (2.4) and (2.8), Γ_W is written as

$$\begin{aligned} \Gamma_W &\equiv 2\pi \frac{M^2}{D} \\ &\sim 4\left(\frac{\langle H_W \rangle}{\Gamma_{spr}}\right)^2 \times \Gamma_{spr}. \end{aligned} \tag{2.11}$$

As shown in this expression, Γ_W is related to $\langle H_W \rangle / \Gamma_{spr}$, which is a typical magnitude of parity mixing between single particle states in nuclei. Therefore Γ_W is considered to express the strength of the weak Hamiltonian in nuclei. In addition, it can be compared to the experimental results obtained for different nuclei. Since Γ_{spr} is a few time 10^6eV, and $\langle H_W \rangle / \Gamma_{spr}$ is approximately 10^{-7}, Γ_W is estimated to be about 10^{-7}eV.

In 1991, Johnson et al. proposed a theoretical method to extract weak coupling constants between meson and two nucleons from the value of Γ_W[54]. An advantage of this approach is in the fact that it is not necessary to calculate the specific wave function of compound nuclei. Since then, a lot of theoretical efforts have been done in this direction [55][56][57].

Auerbach and Vorov studied the mass dependence of Γ_W using a microscopic statistical calculation of the weak interaction in nuclei[58] and found Γ_W to be proportional to $A^{1/3}$. They found also the fact that the dependence is sensitive to the model applied to describe the weak interaction in nuclei. They showed that if the doorway-state approximation is used to calculate Γ_W instead of the model of compound nucleus, Γ_W is proportional to A instead of $A^{1/3}$. They claimed that one-body part and two-body part of the weak Hamiltonian give different contributions to the A dependence.

The experimental determination of Γ_W, in particular the study of mass dependence of Γ_W, is important to understand the weak interaction in nuclei.

Chapter 3

Experimental Procedure

The present experiment was performed at LANSCE with an intense pulsed neutron beam. In order to measure longitudinal asymmetries in many p-wave resonances, an apparatus was developed and used for the experiment. The apparatus is made of a polarized proton filter to polarize neutrons longitudinally, a neutron spin flipper to rotate the direction of neutron spin by 180 degree, a neutron transmission detector to detect transmitted neutrons efficiently, and others. The characteristics and the performances of the apparatus are described in following sections.

3.1 Accelerator and Neutron Source

The experiment was carried out at MLNSC (Manuel Lujan Jr. Neutron Scattering Center) in LANSCE (Los Alamos Neutron Science CEnter). MLNSC has twelve flight paths which provide pulsed neutron beams in the energy range from 10^{-4}eV to 10^{4}eV. The pulsed beams, along with the long flight path, makes possible to apply the time-of-flight technique to the measurement of the neutron energy.

The LANSCE accelerator complex[59][68] consists of a H^- ion source, a 800MeV linac, a proton storage ring (PSR), and a spallation target. The pulsed neutron beam used for this experiment is provided from the spallation target. A schematic view of the complex is given in Figure 3.1.

The H^- ion beam is injected into the linac at 750keV. The beam is accelerated to 100MeV with 201MHz drift-tubes, and then to 800MeV with coupled cavities of 805MHz.

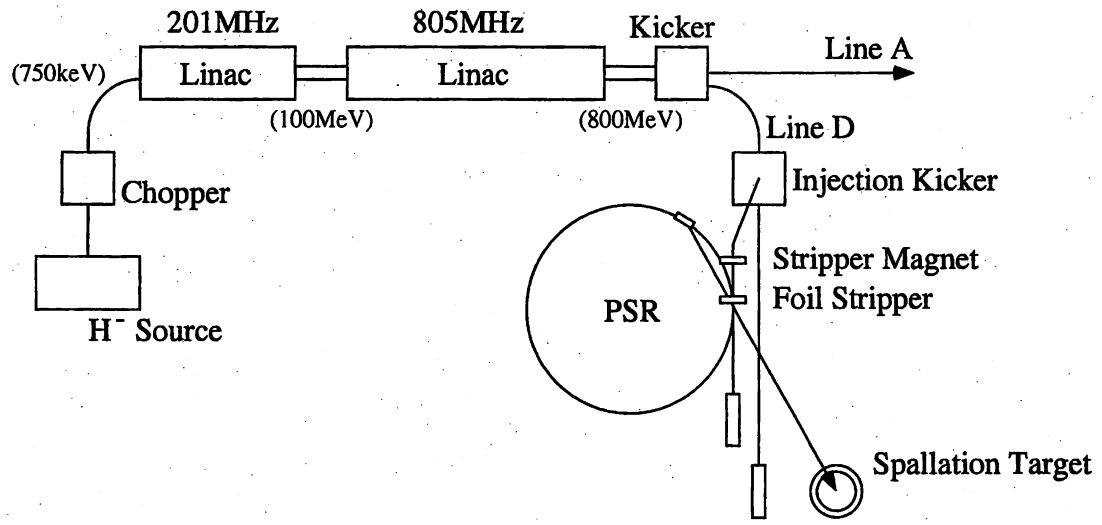

Figure 3.1: Schematic View of LANSCE accelerator complex

The time structure of the accelerated beam consists of macro-pulses with a repetition rate of 120Hz. The typical width of a macro-pulse is 625μsec. Each macro-pulse consists of 0.1nsec micro-pulses, which are separated from each other by about 5ns. There are approximately $1 \sim 2 \times 10^8$ protons in a micro-pulse.

The H^- beam is deflected with a kicker magnet and an injection magnet to be

transported to the PSR. The H^- ion is converted to H^0 by removing one electron in the strong magnetic field of the stripper magnet. The H^0 beam is then converted to the H^+ beam when it passes through a thin carbon foil.

At the injection, macro-pulses are chopped to produce 250ns pulses with 110ns intermissions. Since the circulation time of the beam in the PSR is 360ns, the macro-pulse is wrapped around the PSR until the complete macro-pulse is stored and a intense pulsed beam is created. The accumulated beam is extracted from the PSR and guided to the target system. The time structure of the proton burst at the target can be approximated by a Gaussian shape with standard deviation of 51nsec.

The average current of the beam is about 70μA on the target.

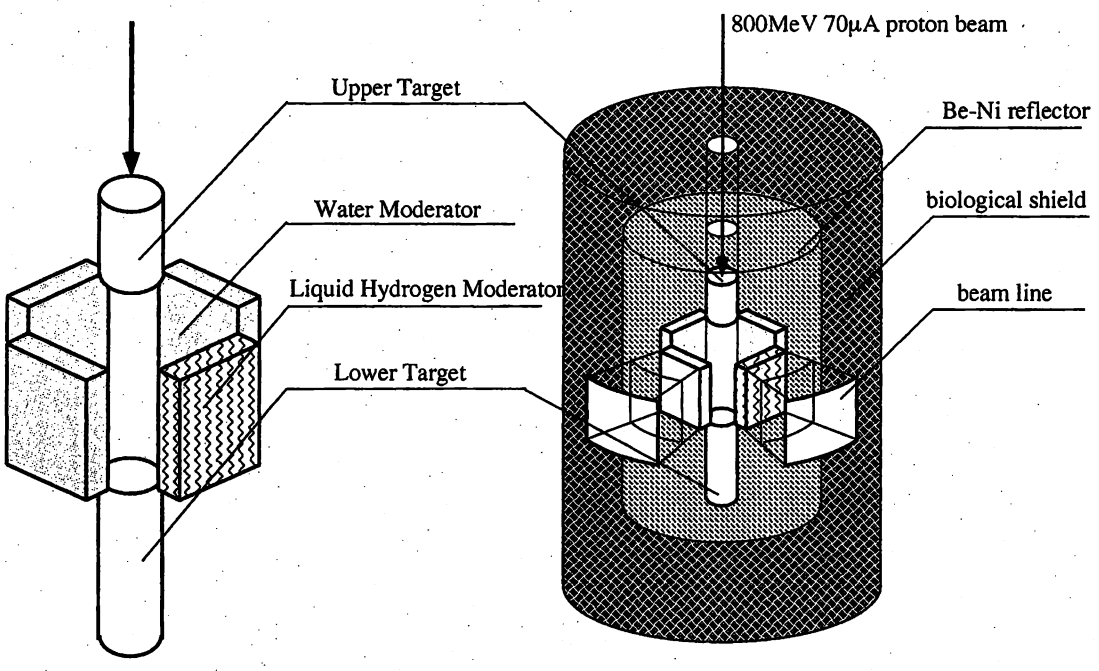

Figure 3.2: Schematic view of LANSCE target system

Figure 3.2 shows the LANSCE target system[69][70]. The LANSCE target system consists of two tungsten targets, water moderators, liquid hydrogen moderators, a Be-Ni reflector, and a biological shield.

Two tungsten targets are vertically separated from each other by 14cm along the proton beam. The size of the upper target is 10cm in diameter and 7.25cm in

length; the size of the lower target is 10cm in diameter and 27cm in length.

The targets are bombarded with the proton beam from the top. About 17 neutrons are produced per incident proton in the target due to the spallation process.

Four moderators are placed in "flux-trap" geometry around the void between the split targets. In this configuration, the backgrounds of γ-rays and high energy neutrons in the secondary neutron beamlines are much reduced compared to the conventional geometry, in which moderators are placed around the target, at the expense of 15$\sim$20 % reduction of the neutron beam intensity. Each moderator provides beams for three flight paths. Three of the four moderators are light water moderators, and the fourth moderator is a liquid hydrogen moderator at temperature of $\sim$20K. The water moderators provide thermal and epithermal neutrons, whereas the liquid hydrogen moderator provides cold neutrons.

The target and moderator are surrounded with the reflector which is made of Ni and Be in order to send back escaping neutron to moderation process. Then the reflector are surrounded with an iron-concrete biological shield. The outer radius of the biological shield is 4.6m.

3.2 Beam Line

Among twelve beam lines, The Flight Path 2 which is the longest beam line providing epithermal neutrons was used for the experiment. The beam line faces the water moderator. The intensity of neutrons at the beam line has been measured[71]. It can be written as

$$\Delta N = (5.8 \times 10^{-3}) \frac{\Delta E_n}{(E_n)^{0.9}} \frac{i}{\nu e} f \Omega, \tag{3.1}$$

where ΔN is the number of neutrons with energies between E_n and $E_n + \Delta E_n$ per beam burst, i is the average proton current, e is the proton charge in coulomb, f is the fraction of the moderator surface viewed by the detector through the collimators, ν is the number of beam burst per second, and Ω is the solid angle of the detector.

A schematic view of the beamline is shown in Figure 3.3. We installed a beam monitor, a neutron polarizer, a spin flipper, and a transmission target in the ER1 cave. We placed the neutron detector and related electronic modules in the 60m hut. A schematic view of the ER1 cave is shown in Figure 3.4. The air in the pipes between the end of the ER1 cave and the 60m hut was exhausted in order to reduce scattering loss of neutrons.

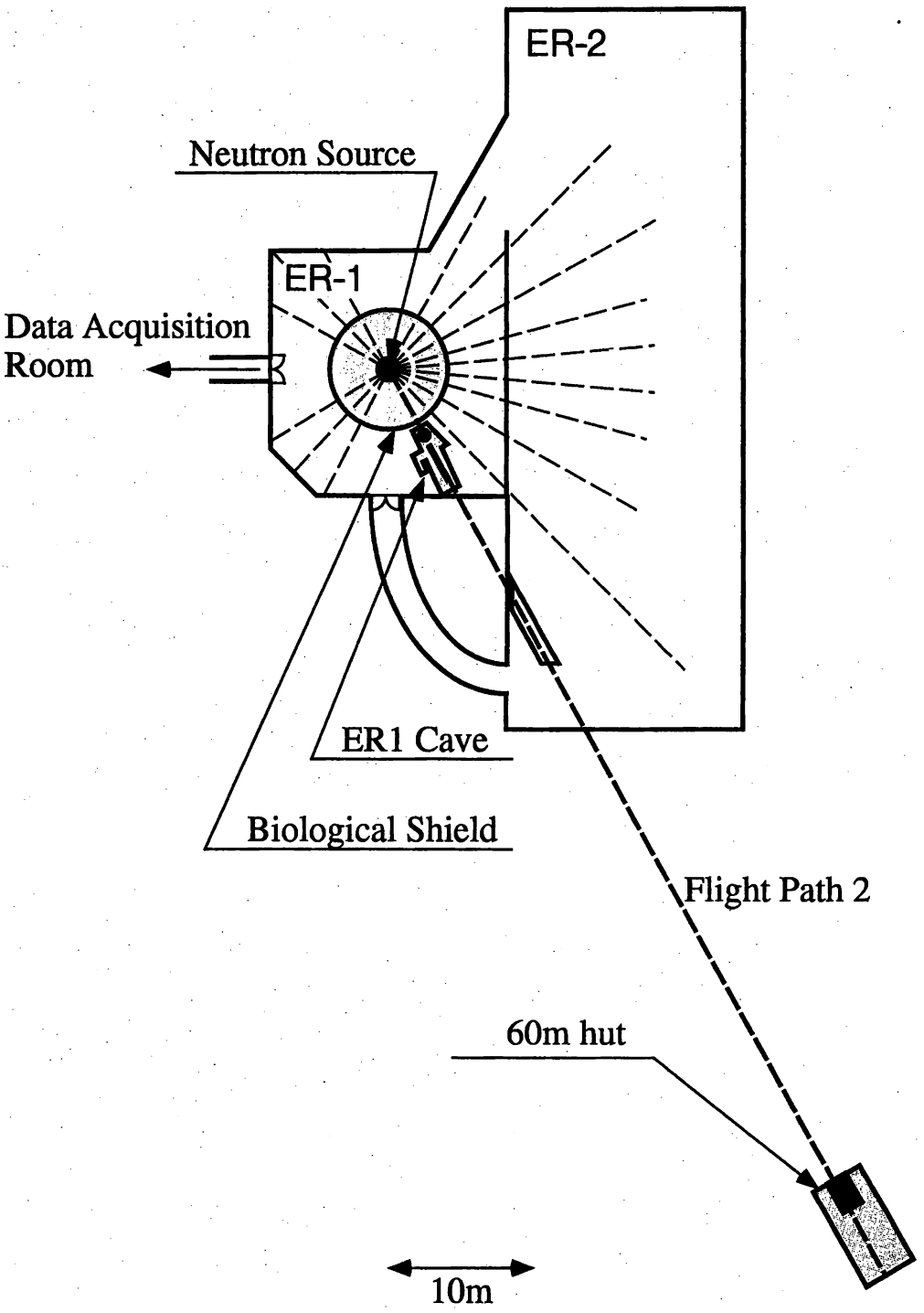

Figure 3.3: Schematic view of Flight Path 2 beam line. Flight Path 2 is the longest beam line of neutrons. ER1 cave

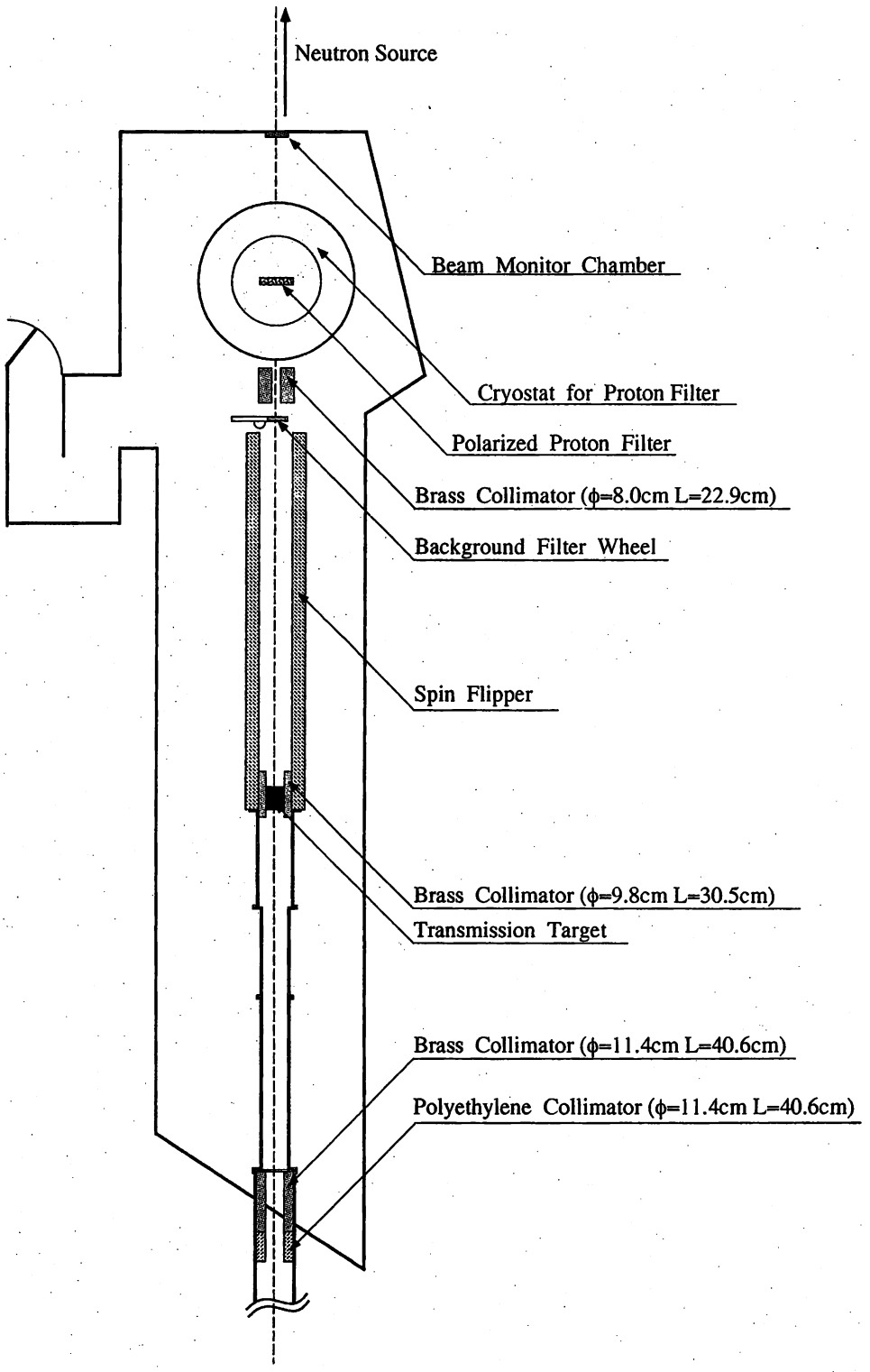

Figure 3.4: Schematic view of the ER1 cave

3.3 Beam Monitor

The beam monitor, which consisted of ^3He and ^4He ionization chambers[72], was placed between the biological shield and the neutron polarizer. The size of each chamber was 9.0cm in width, 9.5cm in height, and 4.0cm in thickness (Figure 3.5). The chambers had 1.6mm-thick aluminum windows on the front and back. The pressures of ^3He and ^4He gases in the chambers were 1.01×10^5 Pa (760Torr).

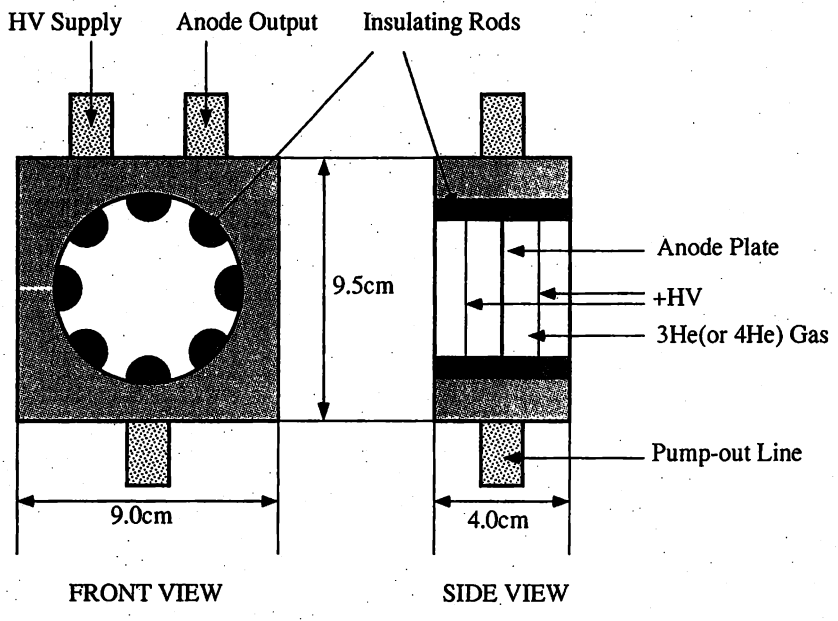

Figure 3.5: Ion chamber for beam monitoring

The ^3He chamber is sensitive to neutrons due to the reaction

$$n + {}^3He \rightarrow p + {}^3H + 0.764MeV. \tag{3.2}$$

The cross section of this reaction is inversely proportional to the square root of the neutron energy. The absorption rate of the neutron of 1eV in the chamber was about 10%. On the other hand, the ^4He chamber is insensitive to neutrons.

Both of the ^3He and ^4He chambers were sensitive to γ-rays originated in Compton scattering on the aluminum windows and in helium gases.

Since the monitor counter was placed very close to the neutron source, counting of individual particle was impossible. Therefore the output DC currents from the anodes of the chambers were measured. The current from each chamber was

converted to pulses with a voltage-to-frequency converter. The output pulses were transmitted to the data acquisition room, where the data acquisition system was located.

The neutron flux was obtained by subtracting the output of the ^4He chamber from that of the ^3He chamber.

The fluctuations due to the change of magnetic field and temperature were measured and found to be negligible[72].

3.4 Neutron Polarizer

It is essential for the experiment to obtain the highly polarized neutron beam in the wide energy range. The polarized proton filter is the most suitable for this purpose[73, 74, 75]. On neutron-proton scattering, the cross section of the neutron whose spin is parallel to proton spin is about 10 times as large as that of the neutron whose spin is anti-parallel, and is almost constant from 1eV to 1keV[76, 73, 77].

When the neutron passes through a polarized proton filter whose polarization is f_p, the total cross section $\sigma_\pm$ of the neutron whose spin is parallel and anti-parallel is written as

$$\sigma_\pm = \sigma_0 \mp f_p \sigma_p, \tag{3.3}$$

where σ_0 is the total cross section for the unpolarized filter, and σ_p is called "the polarization cross section". The transmission of polarized neutron $T_\pm$ through polarized filter whose thickness is t and number density is n is given as

$$\begin{aligned} T_\pm &= e^{-n\sigma_\pm t} = e^{-n\sigma_0 t} e^{\pm f_p n \sigma_p t} \\ &= T_{unpol} e^{\pm f_p n \sigma_p t}, \end{aligned} \tag{3.4}$$

where $T_{unpol} = e^{-n\sigma_0 t}$ is the transmission through the unpolarized proton filter. Therefore the total transmission T_{pol} through the polarized filter is

$$\begin{aligned} T_{pol} &\equiv \frac{1}{2}(T_+ + T_-) \\ &= T_{unpol} \frac{1}{2}(e^{f_p n \sigma_p t} + e^{-f_p n \sigma_p t}) \\ &= T_{unpol} \cosh(f_p n \sigma_p t), \end{aligned} \tag{3.5}$$

and the polarization of the transmitted neutron f_n is,

$$\begin{aligned} f_n &= \frac{T_+ - T_-}{T_+ + T_-} = \tanh(f_p n \sigma_p t) \\ &= \sqrt{1 - \frac{T_{unpol}^2}{T_{pol}^2}}. \end{aligned} \tag{3.6}$$

We used irradiated solid ammonia as filter material[61]. It has advantages over other materials in dilution factor and hydrogen density.

The dynamic nuclear polarization (DNP) was used to polarize protons in the material. The DNP is the method to polarize nuclear spins by transferring the

electron spin polarization to nuclei by means of microwave irradiation. Paramagnetic radicals necessary for the DNP process were doped by irradiation of the electron beam of $\sim 3 \times 10^{16}$ electrons/cm^2.

A side view of the cryostat is shown in Figure 3.6. The filter materials were in the shape of beads of 1-2mm in diameter. These were packed in a cylindrical disk of 80mm in diameter and 13mm in thickness. The packing factor was 0.63. The materials were cooled down to 1K in ^{4}He bath. The cooling power of about 2W at 1K was obtained by pumping ^4He with the speed of $8200m^3/h$. The ^{4}He reservoir surrounding the 1K bath contained the split-coil superconducting magnet which made 5Tesla field at the filter position. The field homogeneity was measured to be 1.3×10^{-4} over a volume of 8cm in diameter and 2cm in length. The 140GHz microwaves of 20mW/cm^3 were applied to the target.

We obtained the proton polarization of about 85%. The build-up time of the proton polarization was about 8 minutes.

The proton polarization was monitored with a Q-meter, whose signals were taken with a data acquisition system on Digital MicroVAX II. The calibration of the NMR system was done by the transmission enhancement measurement. First we measured the effective thickness ($n\sigma t$) of the proton filter by measuring the transmission of neutrons. Then we took the ratio T_{pol}/T_{unpol}. It should be proportional to $\cosh(f_p n\sigma_p t)$ (see Equation (3.5)). Since σ_p is 16.7mb[73], we obtained the proton polarization f_p.

The absolute neutron polarization was obtained by means of the transmission enhancement measurement with Equation (3.6). The neutron polarization was confirmed by the measurement of the known value of parity violation effect at the 0.734-eV p-wave resonance of ^{139}La.

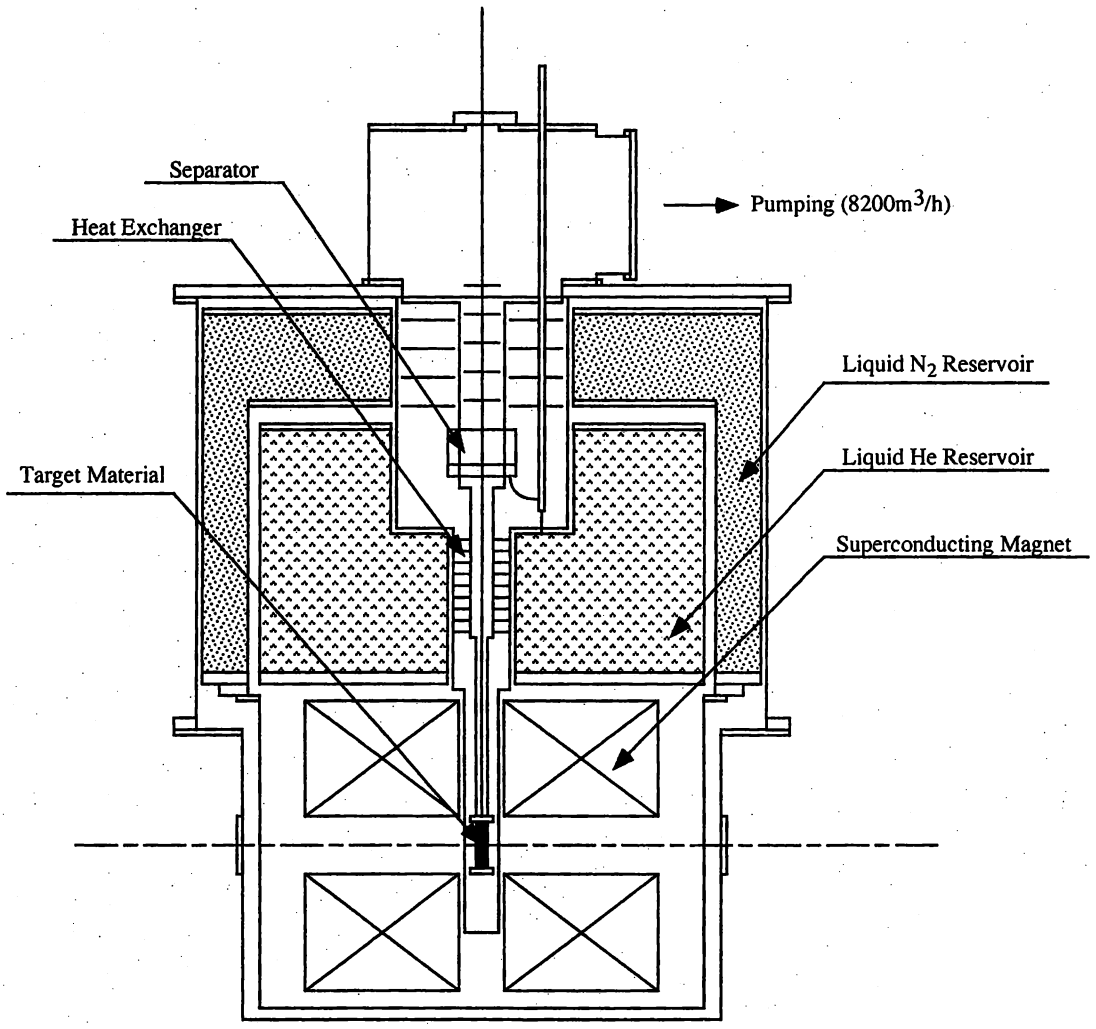

Figure 3.6: Schematic view of the cryostat of the polarized proton filter

3.5 Spin Flipper

In order to measure longitudinal asymmetries of p-wave resonances, it is necessary to reverse the direction of longitudinally polarized neutron spin frequently and efficiently. To satisfy this requirement, the spin flipper was developed and used for our experiment[62].

The spin flipper consists of eight concentric solenoidal coils of different lengths and six pairs of transverse coils (Figure 3.7). In order to accommodate the stray field from the neutron polarizer, the geometry of the solenoidal coils is not symmetric with respect to the center of spin flipper.

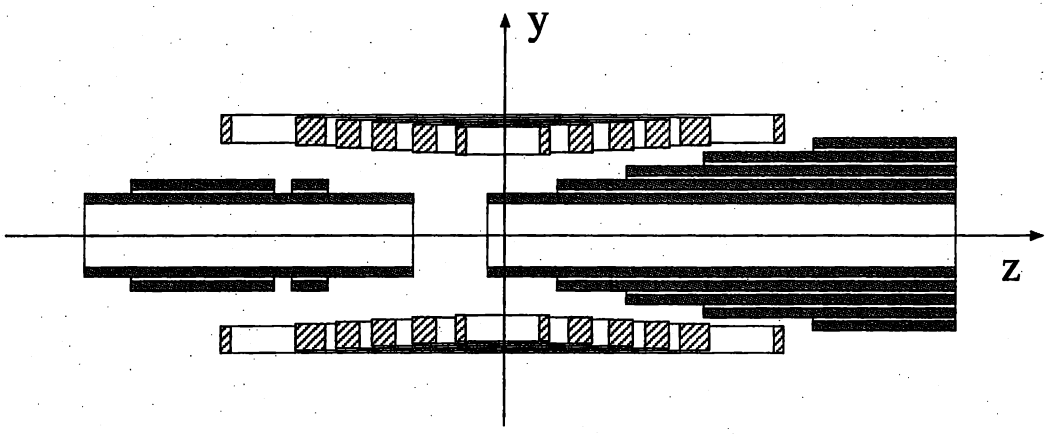

Figure 3.7: Schematic cross sectional view of the spin flipper (drawn not to scale). The solenoidal coils(shaded parts) produce a longitudinal field B_z . The pairs of transverse coils(hatched parts) produce a transverse field B_y. In order to accommodate the stray field from the neutron polarizer the geometry of the solenoidal coils is not symmetric with respect to the center of spin flipper.

The solenoidal coils stayed on always, while the transverse coils was switched to be either on or off, depending on the spin flipper state. When the transverse coils were on, the spin flipper was in the "flip" state, and when they were off, the spin flipper was in "non-flip" state.

The solenoidal coils along the neutron beam produces longitudinal field B_z, whose direction is reversed in the middle of the flipper. On the central axis, B_z has the strength as

$$B_z = \begin{cases} B & (z < -L/2) \\ -B\sin(\pi z/L) & (-L/2 < z < L/2), \\ -B & (L/2 < z) \end{cases} \tag{3.7}$$

where B is about 100G, and L is about 2m.

The transverse coils produce the transverse field B_y, whose strength is,

$$B_y = \begin{cases} 0 & (z < -L/2) \\ B\cos(\pi z/L) & (-L/2 < z < L/2), \\ 0 & (L/2 < z) \end{cases} \tag{3.8}$$

where B and L are the same as Equation (3.7)

The spin flipper was in "flip" state when transverse coils were turned on and smoothly changing magnetic field was produced along the beamline. In this case, the neutron spin followed the magnetic field adiabatically, and the direction of spin was rotated by 180 degrees as the neutron passed through the spin flipper (Figure 3.8).

In case the spin flipper was in the "non-flip" state, there was only the longitudinal field. Therefore the direction of neutron spin didn't change (Figure 3.9).

The efficiency of this spin reversal system was calculated[62], and found to be more than 93% for the neutron energy between 1eV to 350eV.

In order to minimize the effect of the gain drift of the detector, the spin states were alternated every 10 seconds with the sequences as

$$\mathrm{N(0)}\rightarrow\mathrm{F(+)}\rightarrow\mathrm{F(+)}\rightarrow\mathrm{N(0)}\rightarrow\ \mathrm{F(-)}\rightarrow\mathrm{N(0)}\rightarrow\mathrm{N(0)}\rightarrow\mathrm{F(-)},$$

where N(0) means the "non-flip" state, and F($\pm$) means the "flip" state. The signs show the directions of the transverse field.

The currents in the solenoidal coils and the transverse coils were monitored during the experiment.

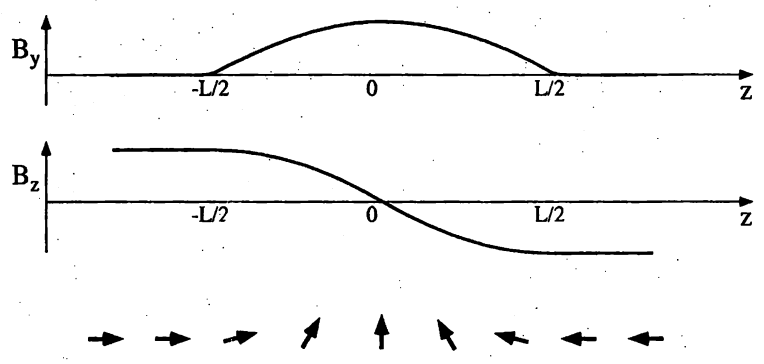

Figure 3.8: Schematic representation of magnetic fields of the spin flipper in the "flip" state. The arrows indicate the direction of spin as the neutron travels through the spin flipper in the "flip" state.

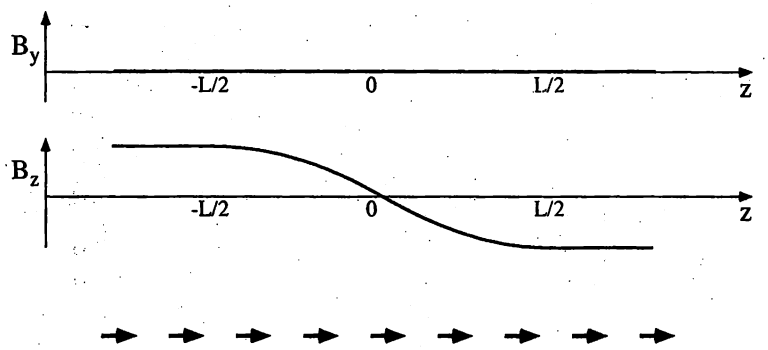

Figure 3.9: Schematic representation of magnetic fields of the spin flipper in the "non-flip" state. The arrows indicate the direction of spin as the neutron travels through the spin flipper in the "non-flip" state.

3.6 Neutron Counter

Neutrons transmitted through the target were detected with the neutron counter placed at about 56m away from the neutron source. The neutron counter was assembled with a scintillator chamber and 55 detectors as shown in Figure 3.10[63].

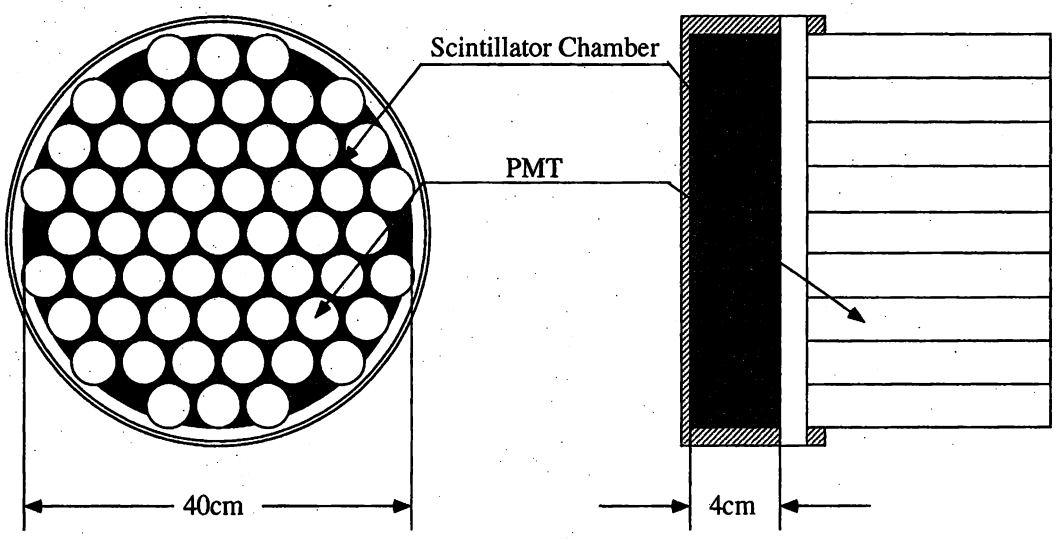

Figure 3.10: Neutron detector system (see the text)

The liquid scintillator doped with 8% ^{10}B in weight was contained in an aluminum cylinder whose diameter was 43cm and depth was 4cm. The diameter of the effective area of the scintillator was 40cm. The scintillator was segmented to 55 hexagonal grids. A photomultiplier tube (PMT) was attached to each grid with a cookie light guide. The segmented arrangement made possible to handle the instantaneous counting rate as high as 500MHz.

Incident neutrons lose the energy in the scintillator due to elastic scattering on protons (thermalization), then are captured by ^{10}B via following reaction

$$\begin{aligned} n + {}^{10}B \rightarrow {}^{7}Li^{*} + \alpha + 2.31MeV \\ \downarrow \\ {}^{7}Li + \gamma(0.482MeV). \end{aligned} \tag{3.9}$$

The scintillation light produced by the α-particle, ^{7}Li, and 0.48MeV γ-ray was detected with Amperex XP2262B PMTs whose diameter were 2 inches. The HV for the tubes were supplied from LeCroy1440 system controlled remotely. The bases

for the tubes were designed to minimize the saturation and baseline shift due to very high counting rate attributed to the fast neutron burst. An air-duct pipe was connected to each base in order to remove heat from the base.

The low-pass filters of 5ns were connected between PMTs and discriminators to improve the discrimination between neutron pulses and single photo-electron pulses. The filter had little effect on the neutron pulse but suppressed the single photo-electron noise, because the width of neutron pulse was about 20 nsec whereas the width of noise was about 3 nsec. The HV for the tubes were adjusted so that the typical pulse height of signal by neutron capture by ^{10}B was 40mV. The signals larger than 30mV were discriminated and converted to NIM pulses whose widths were 5 nsec. Then the pulses were transmitted to the data acquisition room where data acquisition systems were located.

The neutron which entered the scintillator needs finite time to be captured by ^{10}B. This time is called the thermalization time. Since the cross section of neutron capture by ^{10}B is proportional to $1/v_n$ where v_n is the neutron velocity, the thermalization time λ does not depend upon the neutron energy as seen in the following equation

$$\frac{1}{\lambda} = -\frac{dN_n(v_n)}{dt} = -\frac{dN_n(v_n)}{dx}\frac{dx}{dt} \tag{3.10}$$

$$\propto \sigma(v_n) \cdot v_n \tag{3.11}$$

$$= const, \tag{3.12}$$

where $N_n(v_n)$ denotes the number of neutron whose velocity is v_n. x is the flight length. The thermalization time was obtained by comparing the transmission spectra of several resonances observed with the ^{10}B detector and those with a ^{6}Li-glass detector which has no thermalization process[63]. The measured thermalization time was about 410nsec independent of neutron energy.

When the neutron detector has finite dead time τ, the observed yield of neutron Y is written as

$$Y = Re^{-R\tau} \tag{3.13}$$

where R is the number of neutrons per second into the detector.

The dead time τ has been extracted from observed yields with different beam

intensities. The yields Y_1 and Y_2 for different beam intensities are expressed as

$$\begin{aligned} Y_1 &= CM_1 e^{-CM_1\tau} \\ Y_2 &= CM_2 e^{-CM_2\tau}, \end{aligned} \tag{3.14}$$

where M_1,M_2 are the counting rates of the beam monitor, C is constant. The dead time τ has been derived from Equation (3.14) as

$$\tau = \frac{M_1}{M_2 - M_1}\frac{1}{Y_1(t)}\ln\frac{Y_1 M_2}{Y_2 M_1}\exp\left(\frac{M_1}{M_1 - M_2}\ln\frac{Y_1 M_2}{Y_2 M_1}\right). \tag{3.15}$$

The dead time τ for the data obtained in 1995 has been found to be 13nsec. Measured spectra have been corrected by Equation (3.13).

The efficiency of the detector was obtained by comparing the efficiency of the ^6Li-glass detector whose efficiency was well known, and was found to be almost 100% [63].

3.7 Data Acquisition System

A Digital MicroVAX II system running XSYS data acquisition (DAQ) package on VMS operation system were used for data acquisition. The MicroVAX II was connected to MBD(Multi-Branch Driver), which communicated with CAMAC crates. The data acquisition system were located in the data acquisition room, which was about 160m away from the neutron counter.

A signal synchronized with the incident proton burst was provided to the data room. It was called the t_0 pulse. The data acquisition process was initiated with the t_0 pulse.

As mentioned in Section 3.6, a typical instantaneous counting rate of total 55 detector was as high as 500MHz. Such a high counting rate cannot be handled with a conventional multichannel scaler. Therefore a transient digitizer was used to accumulate data.

The NIM pulses from the transmission detectors were discriminated again at data acquisition room to reshape the pulses. The output pulses from the discriminators were fed to a linear signal combiner. In the linear combiner, each pulse was filtered to be a broad Gaussian shaped pulse whose width was 100ns at the half maximum point. The broadened pulses from 55 detectors were linearly summed to make a analog signal whose voltage was proportional to the counting rate of the transmission detector.

The output was then fed to the transient digitizer. The transient digitizer had a 12-bit flush analog-to-digital converter (FADC) to digitize the voltage with intervals determined by an external clock. The sampling interval ("dwell time") was chosen to be either 100nsec, 200nsec, 500nsec or 1μ depending on the region of neutron energies to be measured. The digitized signals were added into an 8192-channel memory module, and the histogram of the counting rate of the transmission detector as a function of time from t_0 pulse (TOF spectrum) was created in the memory module.

To eliminate noises and backgrounds, a fake pulse, t_0' pulse, was invoked 1/60 sec after the t_0 pulse, and the same measurement was repeated. The neutron corresponding to this energy range (<0.06eV) was removed from the beam by the Cd foil of 0.8mm thickness which was placed between the neutron polarizer and the spin flipper. Therefore the output signals had their origin in the 60Hz pickup noise and

the dark current noise. These digitized signals taken with t_0' pulses were subtracted from the memory module.

The signals of beam monitor counters were read by the CAMAC scalers. The gates of CAMAC scalers were opened by the t_0 pulse and t_0' pulse. The number of pulses with the t_0 pulse was subtracted by those with the t_0' pulse to remove the 60Hz pickup noise and the offset of the V-F converter. The obtained beam flux of each beam pulse was recorded.

After 200 beam pulses were accumulated, the spin flipper state was changed in the sequences described in Section 3.5. After one sequence was finished, the fluctuation of beam flux during that period was checked. If the fluctuation was smaller than 8%, the data were labeled as "good". The neutron transmission spectrum was transferred from memory module to the data acquisition computer and stored in the histogram on the computer. If the fluctuation was larger than 8%, the data was labeled as "bad". The spectrum was stored in a different histogram on the computer, and was not used for analyzing the asymmetries.

Other data such as NMR signals of the neutron polarizer, individual counting rates of neutron detectors, and currents in the coils of the spin flipper were monitored and recorded.

A typical run consisted of 20 spin sequences. It took about 30min. When 20 spin sequences were finished, all the histograms were saved in the disk, and the next run was started.

3.8 Data Taking with the Targets of Sb and I

We obtained the data of transmission with the Sb and I target. These targets were placed at the end of the spin flipper.

As the Sb target, we used three disks with natural abundance (57.3% ^{121}Sb and 42.7% ^{123}Sb), each of which was 60mm thick and 104mm in diameter. Total weight of the target was 10275g. In order to reduce Doppler broadening of the resonances, the targets were stored inside the target chiller which cooled the target with liquid nitrogen to 77K.

The data with the Sb target were taken for about six days. The data for 218 runs, each of which took about 30min to complete, were accumulated with a dwell time of 100nsec. In order to reduce systematic errors, the polarization direction of proton filter was reversed by changing the frequency of the microwaves applied to the proton filter. Almost half of the data were taken with the 'positive' polarization of proton filter, and the other half were taken with the 'negative' polarization.

An enriched ^{121}Sb target(99.48% ^{121}Sb and 0.52% ^{123}Sb) was used for the sake of the resonance identification of the isotopes to which individual resonances correspond. The ^{121}Sb target consisted of metal powder packed in a small aluminum cylinder whose inner diameter was 88.9mm. The weight of the target was 38.1951g. Capture γ-ray detectors were used for this measurement since the thickness of the target was too small to identify p-wave resonances in the transmission experiment.

The ^{127}I consisted of small pieces packed in the cylinder of which the diameter was 114mm and length was 545mm. The weight of the target was 15562g. The data were taken for about five days. The data for 185 runs were accumulated with a dwell time of 100nsec, and the data for 64 runs were accumulated with a dwell time of 1000nsec. Almost half of the data were taken with the 'positive' polarization of proton filter and the other half were taken with the 'negative' polarization.

3.9 Measurement of γ-ray Background

In order to know the γ-ray background associated with the neutron beam, we measured the ratio of the counting rates of the neutron detector with two absorbers of the same material but of different thickness. They were placed between the neutron polarizer and the spin flipper. The thickness of one of the foils was as twice as that of the other.

If neutrons in the beam were absorbed completely on strong resonances ("black resonance") in the absorber foil, all the counts in the resonance regions were attributed to the associated γ-rays. The measurement was carried out with the absorbers of In, Ta, Co and Mn which have many black resonances for the neutron.

Table 3.1 shows the list of the absorbers used for the measurement of γ-ray background with their resonance energies and thickness.

Material	Thickness (mm)	(mm)	Resonance energy (eV)
In	0.127	0.254	1.46
Ta	1.27	2.54	4.3 10.4 24.0 35.0 35.9
Co	2.54	5.08	120.0
Mn	1.524	3.048	336.0

Table 3.1: The resonance energies of absorber materials used for the study of γ-ray background. The thicknesses of the absorbers are also shown.

The counting rates on the black resonances with the two foils of the same material are $N_\gamma e^{-n\sigma t}$ and $N_\gamma e^{-2n\sigma t}$ respectively, where N_γ is the number of γ-rays along the beam and $n\sigma t$ is the attenuation rate of the γ-rays with thinner absorber. Then N_γ was derived from the observed values of $N_\gamma e^{-n\sigma t}$ and $N_\gamma \epsilon^{-2n\sigma t}$ as

$$N_\gamma = \left(N_\gamma e^{-n\sigma t}\right) \cdot \frac{(N_\gamma e^{-n\sigma t})}{(N_\gamma \epsilon^{-2n\sigma t})}. \tag{3.16}$$

By using different materials which have black resonances at different energies, the energy dependence of γ-ray background was deduced. The obtained background

was normalized to the counting rate of the monitor counter. Then it was subtracted from the data.

Chapter 4

Analysis

In this chapter, we describe the procedure of the data analysis. The chapter is divided to three sections. In the first section, the computer code developed for the analysis is explained. The formula for calculation of neutron resonance cross section used in the code and the model describing the energy resolution of the beam line are also given. The second section describes the likelihood analysis to determine the weak spreading width from the experimental data. The third section is devoted to the analysis of data. First, the spectroscopic study to determine resonance energies and neutron widths of p-wave resonances are described. Then the analysis of the parity violation effect in p-wave resonances of the ^{121}Sb, ^{123}Sb and ^{127}I target are described.

4.1 Fitting Code

4.1.1 General Description of the Code

In order to study parity violation effects in p-wave resonances, it is necessary to fit the spectra with high accuracy. Since the experiment was carried out in the energy region where many neutron resonances exist and interfere with each other, the precise multi-level calculation of the cross section must be done. The instrumental response function which describes the energy resolution of the MLNSC facility and the TRIPLE detection system must also be employed in the fitting code, because the observed spectra are often strongly influenced by such instrumental broadening effects.

In order to satisfy these requirements, a new analytical computer code, FITXS has been developed and used for the analyses of the data. FITXS allows us to specify the region of the spectrum to be fitted and to extract the best values of fitting parameters by fitting the spectrum with "modified Marquardt" method[78], which is a standard algorithm for solving non-linear χ^2 minimization problems.

FITXS has several advantages over PVIO which was previously used to analyze the data[39][40][79][80]. First, in FITXS the multi-level Reich-Moore formula [81] described at Section 4.1.2 is employed to derive the neutron cross section, whereas in the old code, the single-level Breit-Wigner formula is used. The use of Reich-Moore formula in FITXS not only improves the accuracy of fitting but also makes possible to fit small p-waves near strong s-waves which can not be fitted in PVIO. Secondly, FITXS are made use of a proper response function which integrates resonance broadening due to the Doppler effect, the time structure of neutron beam, the response of detector system and the electronic devices, whereas in PVIO only the Doppler broadening effect is taken into account as an approximation. The fitting is improved by a proper treatment of the response function, in particular in higher energy region, where the intrinsic width is small compared to the response width. Therefore the values of parity violation obtained with PVIO must be re-analyzed using FITXS. The fitting function of FITXS involves many parameters including the resonance parameters of the target nucleus and of contaminated nuclei, abundance and radius of each nucleus and parameters describing the response function, Properties of the target and beam such as thickness of the target and beamline length, and param-

eters on the background are also included. In addition, asymmetry parameters on p-wave resonances are included for analyses of parity violation.

Since all the parameters listed above are variable in FITXS, it can be used not only for extracting asymmetries, but as a versatile program for many aspects of analysis of data, such as determination of the neutron flight length, study of the response function, and spectroscopic study of resonances in neutron reactions.

4.1.2 Reich-Moore Formalism

The Reich-Moore formula[81] is a general multi-level formula to express the fission, radiative capture and scattering cross sections in neutron reactions. All the interferences between the resonance scattering amplitudes and the underlying potential scattering amplitude are taken into account.

When fission cross section is negligible, the s-wave scattering cross section $\sigma_s^{sc}(E)$ is given as a function of neutron energy E

$$\sigma_s^{sc}(E) = \sum_{J=I-\frac{1}{2}}^{J=I+\frac{1}{2}} \pi \lambda\!\!\!^{-2} g_J \left| 1 - e^{-2ikR} \left[1 + \frac{2if_J(E)}{1 - if_J(E)} \right] \right|^2, \quad (4.1)$$

where

$$f_J(E) = \sum_s \frac{\Gamma_n^s/2}{E_s - E - i\Gamma_\gamma^s/2}, \quad (4.2)$$

where J is the total angular momenta of resonances, k is the incident neutron wave number and $\lambda\!\!\!^{-} = 1/k$, R is the potential scattering radius of target nucleus. g_J is the statistical weight factor given by $g_J = \frac{2J+1}{2(2I+1)}$, where I is the spin of target nucleus. E_s, E_γ^s, E_n^s are resonance energy, gamma width, neutron width of s-wave resonance respectively. The summation at Equation (4.2) is carried out over only s-wave resonances with the same angular momentum J.

The s-wave radiative-capture cross section is given as

$$\sigma_s^{\gamma}(E) = \sum_J 4\pi \lambda\!\!\!^{-2} g_J \frac{Re f_J(E)}{|1 - if_J(E)|^2}, \quad (4.3)$$

where f_J is the same as defined at Equation (4.2).

This formula is widely used in spectroscopic studies of the neutron reactions such as the ENDF-VI evaluation in BNL[82] and the JENDL-3 evaluation in JAERI[83].

4.1.3 Fitting Function of FITXS

The fitting function of FITXS is written as

$$Y(t) = Y_0(t) \otimes R(t) + B(t), \tag{4.4}$$

where t is the flight time of the neutron, $Y_0(t)$ is the yield with infinite energy resolution, $R(t)$ is a instrumental response function and $B(t)$ is the background. $\otimes$ represents the convolution operation.

$Y_0(t)$ for transmission measurement is given by

$$Y_0(t) = F(t)e^{-n\sigma_D(t)} \quad , \tag{4.5}$$

where $F(t)$ is the neutron beam flux, n is the target thickness, $\sigma_D(t)$ is the total cross section broadened by the Doppler effect.

The Doppler broadened total cross section is calculated as a convolution of the cross section $\sigma(v)$ which is calculated using Reich-Moore formula with the Doppler broadening function $D(v)$ as

$$\sigma_D(v) = \sigma(v) \otimes D(v) = \int_{-\infty}^{\infty} \sigma(v-u)\sqrt{\frac{M}{2\pi kT}}e^{\frac{-Mu^2}{2kT}}du, \tag{4.6}$$

where M is the target mass, k is the Boltzmann constant, and T is the effective temperature of the target.

After the convolution above is carried out, the Doppler broadened cross section is converted to a function of t. The yield $Y_0(t)$ is calculated by Equation (4.5). Then the second convolution with the response function $R(t)$ is performed to make the fitting function.

Two convolutions involved in calculating the fitting function do not commute and cannot be performed analytically. These convolutions are numerically carried out using the Fast Fourier Transform (FFT) technique. Spacing of grids on which the convolution is performed are determined to be smaller than any of 1/20 of the width of the Doppler broading function, 1/10 of the neutron width of the resonance and 1/20 of the width of response function, so that the error due to the convolution is negligible.

4.1.4 Response Function

The energy resolution of the neutron beam at LANSCE was studied by Koehler in 1994[84]. Further study on Flight Path 2 was made by Yi-Fen et al.[85], where

comparison between experimental data and Monte-Carlo simulations of neutron moderation processes were made. We applied the extended version of the model to the response function $R(t)$ in FITXS.

The response function $R(t)$ is expressed by a convolution of four response functions.

$$R(t) = R_{PSR}(t) \otimes R_{mod}(t) \otimes R_{det}(t) \otimes R_{inst}(t), \tag{4.7}$$

where $R_{PSR}(t)$ represents the broadening due to the time structure of the proton pulse from the PSR, $R_{mod}(t)$ represents the time structure of neutron beam due to the moderation process in the target system, $R_{det}(t)$ represents the response function of the detector, and $R_{inst}(t)$ represents the response function of the electronics. Each response function is expressed by a Gaussian $f_G(t;\sigma)$, a exponential function $f_E(t;\tau)$, or their convolution. Here $f_G(t;\sigma)$ is defined as

$$f_G(t;\sigma) \equiv \frac{1}{\sqrt{2\pi}\sigma} e^{-t^2/2\sigma^2}. \tag{4.8}$$

And $f_E(t;\tau)$ is defined as

$$f_E(t;\tau) \equiv \frac{1}{\tau} e^{-t\tau} \theta(t), \tag{4.9}$$

where $\theta(t)$ is a step function, that is $\theta(t) = 1$ for $t \geq 0$ and $\theta(t) = 0$ for $t < 0$.

As we noted in Section 3.1, the proton pulse from the PSR has finite width, and its shape is approximated with a Gaussian as

$$R_{PSR}(t) = f_G(t;\zeta), \tag{4.10}$$

and standard deviation of the distribution ζ is independent of the neutron energy. The value $\zeta = 51nsec$ is used for the analysis of data.

The time structure of neutron beam is not symmetric, but it has a low-energy tail due to the moderation process in the neutron source. This asymmetric shape is represented by a convolution of a Gaussian with two exponential terms

$$\begin{aligned} R_{mod}(t) &= f_G(t;\eta) \otimes (f_E(t;\tau_1) + \epsilon f_E(t;\tau_2)) \\ &= f_{GE}(t;\eta,\tau_1) + \epsilon f_{GE}(t;\eta,\tau_2), \end{aligned} \tag{4.11}$$

where η represents the Gaussian broadening in the moderation process in target system, whereas τ_1 and τ_2 represents exponential tails. ϵ stands for the ratio of the

strengths of two exponential parts. The function $f_{GE}(t;\eta.\tau)$ are defined as

$$\begin{aligned} f_{GE}(t;\eta,\tau) &\equiv f_G(t;\eta) \otimes f_E(t;\tau) \\ &= \int_{-\infty}^{\infty} f_G(t-s;\eta) f_E(s;\tau) ds \\ &= \frac{1}{2\tau} e^{t/\tau+\eta^2/2\tau^2} \left(1 - f_{erf}(Z)\right). \end{aligned} \tag{4.12}$$

Z is given by $Z = (\eta/\tau - t/\eta)/\sqrt{2}$. $f_{erf}(Z)$ is the error function defined as

$$f_{erf}(Z) \equiv \frac{2}{\sqrt{\pi}} \int_0^Z e^{-t^2} dt. \tag{4.13}$$

The standard deviation of Gaussian and exponential parameters, which are written as η, τ_1, τ_2 respectively in Equation (4.11) depend on the neutron energy. These parameters are determined experimentally.

As shown in Section 3.6, the neutron entered ^{10}B doped scintillator needs finite thermalization time before detection. The time spread due to the thermalization in the scintillator is written as

$$R_{det}(t) = f_E(t;\lambda), \tag{4.14}$$

where $\lambda = 410$nsec is independent of neutron energy.

The response function of electronics $R_{inst}(t)$ comes from broadening of the pulse in the analog filter inserted in front of the transient digitizer (see Section 3.7). The shape of the output current of the linear combiner is approximated by a Gaussian distribution.

$$R_{inst}(t) = f_G(t;\xi), \tag{4.15}$$

where the standard deviation $\xi = 46$nsec is independent of neutron energy.

First, the Gaussian part of the response function in Equation (4.7) is combined. Then $R(t)$ is calculated as

$$\begin{aligned} R(t) &= R_{PSR}(t) \otimes R_{mod}(t) \otimes R_{det}(t) \otimes R_{inst}(t) \\ &= f_G(t;\zeta) \otimes f_G(t;\eta) \otimes (f_E(t;\tau_1) + \epsilon f_E(t;\tau_2)) \otimes f_E(t;\lambda) \otimes f_G(t;\xi) \\ &= f_G(t;\kappa) \otimes (f_E(t;\tau_1) + \epsilon f_E(t;\tau_2)) \otimes f_E(t;\lambda) \\ &= f_{GEE}(t;\kappa,\tau_1,\lambda) + \epsilon f_{GEE}(t;\kappa,\tau_2,\lambda), \end{aligned} \tag{4.16}$$

where $\kappa^2 = \zeta^2 + \eta^2 + \xi^2$. $f_{GEE}(t;\kappa,\tau,\lambda)$ is defined as;

$$\begin{aligned} f_{GEE}(t;\kappa,\tau,\lambda) &\equiv f_G(t;\kappa) \otimes f_E(t;\tau) \otimes f_E(t;\lambda) \\ &= \int_{-\infty}^{\infty}\int_{-\infty}^{\infty} f_G(t-v-w;\kappa) f_E(v;\tau) f_E(w;\lambda) dv dw \\ &= \frac{1}{2(\lambda-\tau)}\left[e^{t/\lambda+\kappa^2/2\lambda^2}(1-f_{erf}(Z_\lambda))\right. \\ &\qquad \left. -e^{t/\tau+\kappa^2/2\tau^2}(1-f_{erf}(Z_\tau))\right], \end{aligned} \tag{4.17}$$

where $Z_\lambda = (\kappa/\lambda - t/\kappa)/\sqrt{2}$ and $Z_\tau = (\kappa/\tau - t/\kappa)/\sqrt{2}$.

As seen in Equation (4.16), the response function $R(t)$ is parameterized with seven parameters.

Three of them, $\zeta = 51$nsec, $\xi = 46$nsec and $\lambda = 410$nsec are already determined and they are independent of the neutron energy. The other parameters, η, τ_1, τ_2 and ϵ are determined by comparing the results of Monte-Carlo simulation of the spectra and experimental data[85] and also by fitting experimental data with the FITXS code at several neutron energies. ϵ is assumed to be independent of the neutron energy. We have obtained

$$\begin{aligned} \eta &= 0.65 \times E^{-0.48} \mu sec \\ \tau_1 &= 0.99 \times E^{-0.37} \mu sec \\ \tau_2 &= 3.90 \times E^{-0.38} \mu sec \\ \epsilon &= 0.2, \end{aligned} \tag{4.18}$$

where E is the neutron energy in eV.

Contributions of these parameters to the broadening of the resonance shape as well as Doppler broadening are shown in Figure 4.1. Doppler broadening is dominant in low energy region. In high energy region, exponential tails due to the moderations (τ_1 and τ_2) and the thermalization time in the detector (λ) contribute dominantly to the broadening. Thus observed resonance shape becomes asymmetric.

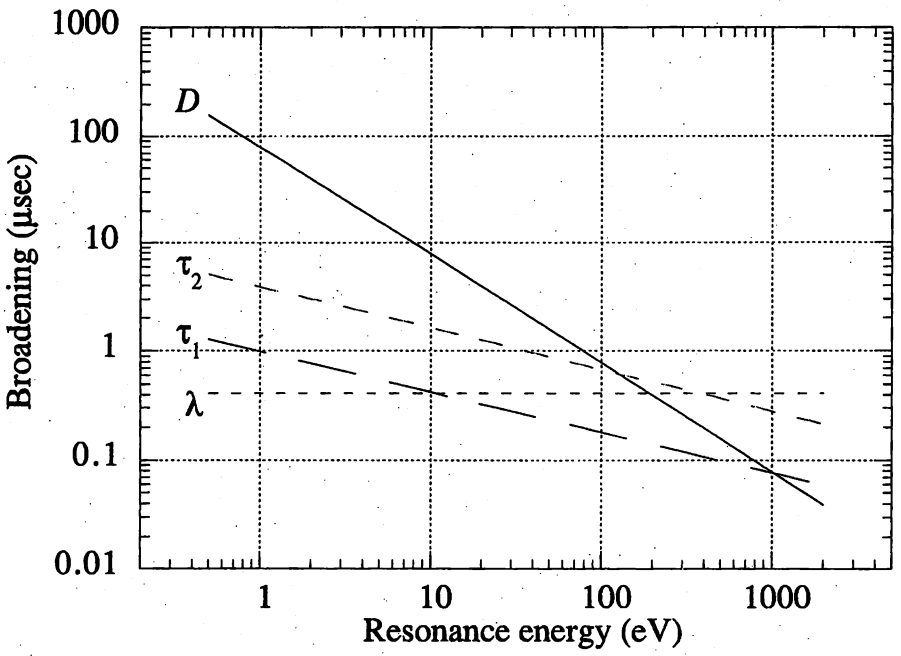

Figure 4.1: Full widths at half maximum of the broadening which contribute to the response shape. Doppler broadening effect (D), exponential tails due to the moderations (τ_1 and τ_2), and thermalization time in the transmission detector (λ) are plotted as a function of the resonance energy. The calculation has been done for ^{121}Sb at target temperature of 100K, and the neutron flight length of 56m.

4.2 Likelihood Analysis

4.2.1 Principle of Maximum Likelihood Method

The maximum likelihood method is a powerful tool for finding the best value of an unknown parameter. It has been applied to extract the value of Γ_W from the experimental data.

Suppose the probability density function of a variable p is written as $y(p|m)$ with a parameter m. If we measure p with a given value of m, the probability to obtain a measured value p_i within the range $[a, b]$ is given by the integral $\int_a^b y(p_i|m)dp_i$.

Then we estimate the value of the unknown parameter m from the measured value p_i. If we write the function $L(m)$ as

$$L(m) = L_i(m) \equiv y(p_i|m) \tag{4.19}$$

the best value of m is given by the value which maximizes $L(m)$. $L(m)$ is called the likelihood function of m.

When a series of independent measurements of p are done, the joint probability density for obtaining a particular set of p_i's is given as

$$y(p_1 \cdots p_n|m) = \prod_i y(p_i|m). \tag{4.20}$$

Therefore the likelihood function $L(m)$ is given by

$$L(m) = \prod_i L_i(m), \tag{4.21}$$

where $L_i(m)$ is given in Equation (4.19).

The error of the best value of m is represented by the region $[m_-, m_+]$ where m_- and m_+ satisfy the equation

$$\ln\left(\frac{L(m_\pm)}{L(m)}\right) = -\frac{1}{2}. \tag{4.22}$$

If $L(m)$ is a Gaussian distribution, the error agrees with the root mean square deviation of the distribution.

4.2.2 Likelihood Function of Γ_W

In Equation (2.1), we took account of only single s-wave resonance to interfere with a p-wave resonance. In general, the longitudinal asymmetry of μ-th p-wave

resonance is written by the sum of the contributions from many s-wave resonances.

$$P_\mu = \sum_\nu \frac{2V_{\nu\mu}}{E_\nu - E_\mu}\sqrt{\frac{\Gamma_\nu}{\Gamma_\mu}}x_\mu \quad (\text{for } J_\nu = J_\mu)$$
$$= \sum_\nu A_{\nu\mu}V_{\nu\mu}x_\mu, \tag{4.23}$$

$$\text{where} \quad A_{\nu\mu} \equiv \frac{2}{E_\nu - E_\mu}\sqrt{\frac{\Gamma_\nu}{\Gamma_\mu}}, \tag{4.24}$$

$$x_\mu \equiv \sqrt{\frac{\Gamma_{\mu 1/2}}{\Gamma_{\mu 1/2} + \Gamma_{\mu 3/2}}}. \tag{4.25}$$

The summation in Equation (4.25) is carried out over only s-wave resonances which have the same spin J as that of the p-wave resonance. For nuclei of which spins are zero, x always eqauls unity.

As shown in Section 2.1, the weak matrix element $V_{\nu\mu}$ obeys a Gaussian distribution with mean zero, and its variance $M^2 = (\Gamma_W D/2\pi)$ is common for all μ. This means all the probability distribution functions of the asymmetries for p-wave resonances have common parameter Γ_W. As described in Section 4.2.1, we can interpret this probability distribution function as the likelihood function $L_\mu(\Gamma_W)$ with the measured value of P_μ. Since $V_{\nu\mu}$'s are independent random variables, the values of P_μ's are independent of each other. Therefore the likelihood function $L(\Gamma_W)$ with the observed asymmetries over many resonances of the same nucleus is given by the product of individual likelihood function $L_\mu(\Gamma_W)$ as shown in Equation (4.21).

Since the spins of p-wave resonances are unknown in most nuclei and x's are unknown except for a few p-wave resonances, the likelihood function $L_\mu(\Gamma_W)$ is complicated function. Bowman et al.[53] formulated $L_\mu(\Gamma_W)$'s according to different amounts of our knowledge of spins and x's of p-wave resonances. These formulas have been applied to the analysis of the data.

For nuclei of which spins are not zero, the likelihood function of Γ_W with measured asymmetry $P_\mu \pm \sigma_\mu$ for μ-th p-wave resonance is given as following.

In the case that we know the spin of p-wave resonance and the value of x_μ, $L_\mu(\Gamma_W)$ is written as

$$L_\mu(\Gamma_W) = \frac{1}{\sqrt{2\pi M^2 A_\mu^2 x_\mu^2 + \sigma_\mu^2}} e^{-\frac{1}{2}\frac{P^2}{M^2 A_\mu^2 x_\mu^2 + \sigma_\mu^2}}, \tag{4.26}$$

where $M^2 = \Gamma_W D/2\pi$. A_μ^2 is defined as

$$A_\mu^2 \equiv \sum_\nu \left(\frac{2}{E_\nu - E_\mu}\right)^2 \frac{\Gamma_\nu}{\Gamma_\mu} \qquad (\text{for } J_\nu = J_\mu), \tag{4.27}$$

where the summation is carried out over all s-wave resonances which have the same spin J as that of the p-wave resonance.

In the case that the value of x_μ is unknown, $L_\mu(\Gamma_W)$ is written as

$$L_\mu(\Gamma_W) = \frac{2}{\pi}\int_0^{\pi/2} \left(\frac{a}{a^2 sin^2\theta + cos^2\theta} \frac{1}{\sqrt{2\pi M^2 A_\mu^2 \sin^2\theta + \sigma_\mu^2}} e^{-\frac{1}{2}\frac{P^2}{M^2 A_\mu^2 \sin^2\theta + \sigma_\mu^2}}\right) d\theta, \tag{4.28}$$

where $x_\mu \equiv \sin\theta$ is expressed in the polar coordinate. The a is the parameter to represent the square root of the ratio of the p-wave strength function of $j = 3/2$ channel and that of $j = 1/2$ channel.

In the case that the spin of the p-wave resonance as well as x_μ are unknown, the likelihood function is more complicated. The weak matrix element may be different for $J = I \pm 1/2$ states because of the difference of level spacing, whereas the weak spreading width Γ_W is considered to be independent of J. Thus M_J is defined as $M_J^2 = \Gamma_W D_J/2\pi$, where D_J is the average level spacing for resonances which have spin J. $L_\mu(\Gamma_W)$ is written as

$$\begin{aligned} L_\mu(\Gamma_W) \;=\; & \left\{ \sum_{J=I\pm 1/2} p_J \frac{2}{\pi}\int_0^{\pi/2} \left(\frac{a}{a^2 sin^2\theta + cos^2\theta}\right. \right. \\ & \left. \frac{1}{\sqrt{2\pi M_J^2 A_\mu^2 \sin^2\theta + \sigma_\mu^2}} e^{-\frac{1}{2}\frac{P^2}{M_J^2 A_\mu^2 \sin^2\theta + \sigma_\mu^2}}\right) d\theta \\ & \left. + \sum_{J=I\pm 3/2} p_J \frac{1}{\sqrt{2\pi\sigma_\mu^2}} e^{-\frac{1}{2}\frac{P^2}{\sigma_\mu^2}} \right\}, \end{aligned} \tag{4.29}$$

where p_J denotes the probability of the p-wave resonance to have spin of J. p_J is estimated by the formula given by Gilbert et al[86] with the parameters determined by Egidy et al for many nuclei[87].

4.3 Analysis of Data

4.3.1 Determination of Resonance Energies

The time-of-flight(TOF) technique has been applied to convert the TOF channels to the corresponding neutron energies. The time-of-flight t, energy E, and flight length L of the neutron are related as

$$\begin{aligned} E &= \frac{1}{2} m_n v_n^2 \\ &= \frac{1}{2} m_n \frac{L^2}{(t - t_0)^2} \qquad (4.30) \\ t\sqrt{E} &= t_0\sqrt{E} + \sqrt{\frac{m_n}{2}} L, \qquad (4.31) \end{aligned}$$

where m_n is the mass of neutron, v_n is the velocity of neutron, and t_0 is the timing offset of the transient digitizer.

L and t_0 have been determined by plotting $t\sqrt{E}$ versus $\sqrt{E}$ for known resonances and applying the linear fit to the data. The linear fit gives t_0 and L. Typical data used for fitting are given in Figure 4.2. The arrival times have been determined by fitting the spectra with the analysis code described in Section 4.1. The resonance energies obtained in previous spectroscopic studies[64] were used for the analysis. Uncertainties of resonance energies and fitting errors of resonance channels account for the errors of the data points. $L = (56.829 \pm 0.030)$m and $t_0 = (3935.0 \pm 144.6)$nsec have been obtained using the transmission data on ^{121}Sb, ^{123}Sb and ^{127}I.

4.3.2 Determination of Neutron Widths of p-wave Resonances

The neutron widths of p-wave resonances have been deduced by fitting the observed data of transmission to the calculated neutron transmission spectra using the FITXS program described in Section 4.1. Since the data for both helicity states have been summed up, the obtained widths have not been affected by possible longitudinal asymmetries on the resonances.

Only the resonance energies and the neutron widths have been variables for fitting data. The TOF parameters and the parameters of the response function have been determined independently. As the radiative widths on p-wave resonances,

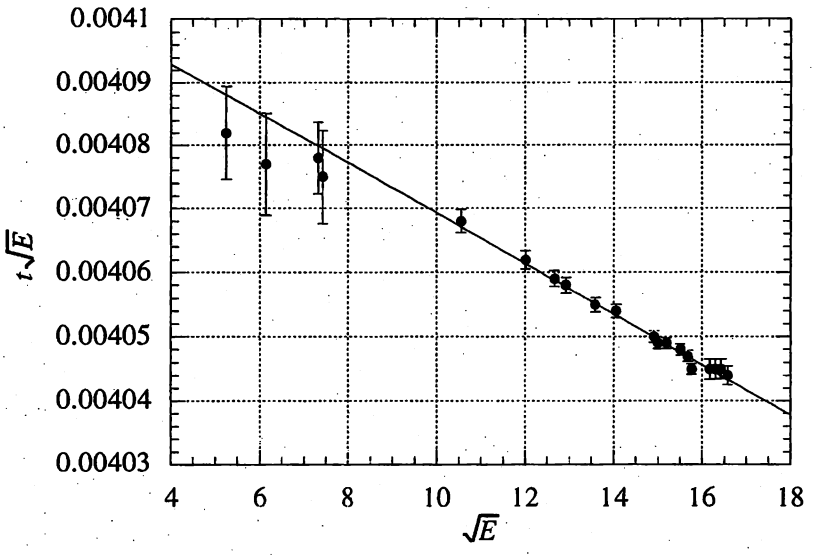

Figure 4.2: Determination of L and t_0 using known resonances. $t\sqrt{E}$ are plotted versus $\sqrt{E}$, where E is the neutron energy and t is the arrival time of neutron.

the typical value obtained from the compilation by Mughabghab et al.[64] has been adopted.

The energies and the neutron widths have been determined by means of this method. Some of these resonances have been found in this experiment for the first time.

Figure 4.3 shows the transmission spectrum for the ^{121}Sb target in the energy region of 90.1eV to 94.0eV, as well as a curve fitted to it with the best values of the parameters of the FITXS program. We have found a new resonance at 92.1eV of which neutron width have been determined to be 17.0×10^{-6}eV.

Figure 4.4 shows the transmission spectrum and a fitted curve around 261.6-eV and 265.8-eV resonances of ^{121}Sb. The resonances show the asymmetric shapes due to the neutron moderation in the moderator and the thermalization in the transmission detector as described in Section 4.1.4. The asymmetric shapes of the resonances have been well reproduced by FITXS.

Figure 4.5 shows a part of the transmission spectrum as well as a fitted curve for ^{127}I. The 137.0-eV resonance has been found for the first time. The figure demonstrates that FITXS is capable of fitting p-wave resonances close to strong s-wave resonances.

The energies and the neutron widths of the resonances obtained in this experiment as well as those by Mughabghab et al.[64] are listed in Table 4.1, 4.2 and 4.3.

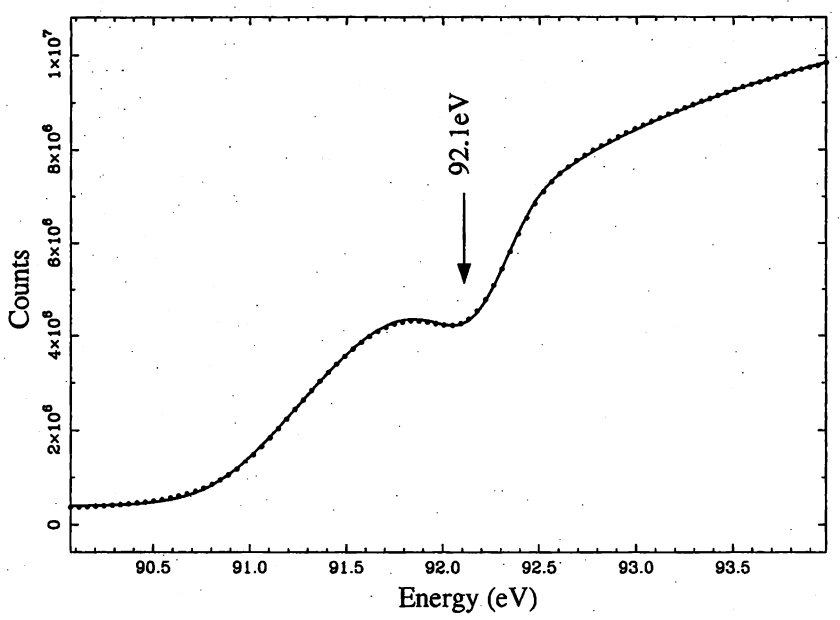

Figure 4.3: The neutron transmission spectrum around the 92.1-eV resonance of ^{121}Sb is shown. The solid line shows the curve obtained by the fitting procedure (see the text). The shape of spectrum near the 92.1-eV resonance is distorted by the neighboring s-wave resonances at 90.3eV.

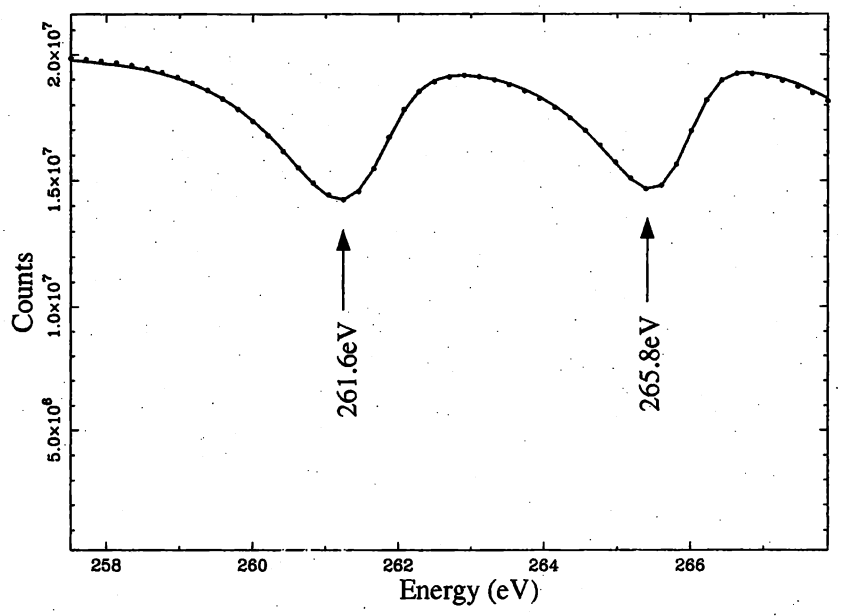

Figure 4.4: The neutron transmission spectrum around the 261.6-eV and 265.8-eV resonances of ^{121}Sb is shown. The solid line shows the curve obtained by the fitting procedure (see the text). The asymmetric shapes of the resonances are reproduced by fitting in which the neutron moderation in the moderator and the thermalization in the neutron detector are taken into account.

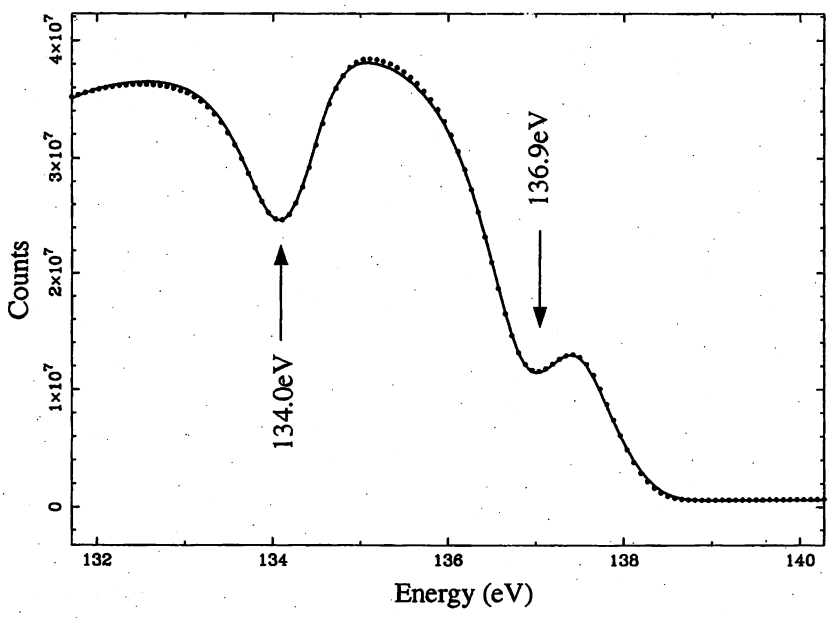

Figure 4.5: The neutron transmission spectrum around the 134.1-eV and 136.9-eV resonances of ^{127}I is shown. The solid line shows the curve obtained by the fitting procedure (see the text). The shape of the spectrum near the resonances is distorted by the neighboring s-wave resonances at 139.7eV.

Resonance energy E_r [eV]		Neutron width $g\Gamma_n$ [10^{-6}eV]	
This work	Mughabghab et al.[64]	This work	Mughabghab et al.[64]
37.90±0.03	37.77±0.15	8.464	8.5±1.5
55.21±0.03	55.1±0.2	14.47	20±5
92.14±0.04	(not listed)	17.0	(not listed)
110.74±0.04*	(not listed)	37.3	(not listed)
141.24±0.03	(not listed)	8.1	(not listed)
174.53±0.03	(not listed)	5.40	(not listed)
177.10±0.03	176.6±0.1	43.0	40±10
184.69±0.03	184.7±0.1	126.0	90±10
200.26±0.03	(not listed)	35.9	(not listed)
228.55±0.03	228.7±1.0	44.1	45±13
235.92±0.03	236.4±1.0	19.2	23±9
245.90±0.04	245.9±0.1	234.6	145±25
248.98±0.04	248.8±0.1	127.8	140±30
261.60±0.04	261.6±0.2	181.1	100±50
265.77±0.05	265.8±0.2	167.2	125±20
269.96±0.05	270.1±0.2	207.7	120±25
274.79±0.05	274.9±0.2	153.5	140±35

*) 110.74eV : very close to the 111.4eV ^{121}Sb s-wave resonance. resonance parameters may have large errors.

Table 4.1: The energies and neutron widths of the p-wave resonances of ^{121}Sb obtained by this experiment and those by Mughabghab et al. are shown.

Resonance energy E_r [eV]		Neutron width $g\Gamma_n$ [10^{-6}eV]	
This work	Mughabghab et al.[64]	This work	Mughabghab et al.[64]
176.40±0.03	176.4±0.1	175.7	140±25
186.08±0.03	186.1±0.1	154.4	160±30
197.70±0.03	197.8±0.1	243.3	195±15
201.95±0.03*	(not listed)	20.9	(not listed)
225.19±0.03	225.1±0.1	160.0	140±20

*) 201.95eV : small p-wave resonance, not found in ^{121}Sb

Table 4.2: The energies and neutron widths of the p-wave resonances of ^{123}Sb obtained by this experiment and those by Mughabghab et al. are shown.

Resonance energy E_r [eV]		Neutron width $g\Gamma_n$ [10^{-6}eV]	
This work	Mughabghab et al.[64]	This work	Mughabghab et al.[64]
7.51±0.01	(not listed)	0.12	(not listed)
10.34±0.01	10.7	2.8	(not listed)
13.93±0.02	(not listed)	1.4	(not listed)
24.63±0.02	(not listed)	0.64	(not listed)
52.20±0.05	(not listed)	0.85	(not listed)
53.82±0.05	53.77±0.12	18.9	17.5±2.5
64.04±0.06	64.18±0.15	7.9	3.5±1.5
85.84±0.07	85.87±0.30	17.4	14.5±2.5
101.14±0.08	(not listed)	13.7	(not listed)
126.03±0.08	(not listed)	2.1	(not listed)
134.13±0.08	134.4±0.4	25.5	29±7.5
136.94±0.08	(not listed)	40.2	(not listed)
145.71±0.08	145.83±0.15	33.5	250±50
153.60±0.08	153.65±0.20	95.7	99±13
223.40±0.08	(not listed)	11.3	(not listed)
256.77±0.08	256.85±0.32	52.3	8±3
274.66±0.08	(not listed)	22.1	(not listed)
282.10±0.08	(not listed)	4.5	(not listed)
351.93±0.11	352.26±0.18	88.1	78±15
353.34±0.11	353.22±0.19	88.7	81±15

Table 4.3: The energies and neutron widths of the p-wave resonances of ^{127}I obtained by this experiment and those by Mughabghab et al. are shown.

4.3.3 Extraction of Asymmetries

The analyses of longitudinal asymmetries have been done for all the resonances of ^{121}Sb, ^{123}Sb and ^{127}I using the FITXS program.

The transmission spectra for p-wave resonances have been fitted by run-by-run basis. In the fitting process, the beam-line parameters and the resonance parameters determined in Section 4.3.1 and Section 4.3.2 have been held fixed for the analysis of each run.

First, the average of two spectra with both helicity states has been fitted in order to obtain the neutron flux of the run. Then the spectra with different helicity states have been fitted separately. The cross sections for p-wave resonance for both helicity states $\sigma_{p\pm}$ are represented by the FITXS program using parameter A as

$$\sigma_{p\pm} = \sigma_p(1 + A^{\pm}), \tag{4.32}$$

where $\pm$ denote the helicity states and σ_p is the cross section for unpolarized neutron which is calculated with the neutron width obtained in Section 4.3.2. In this fitting process, only the parameters $A^{\pm}$ have been varied, and other parameters such as neutron flux or resonance parameters have been held fixed. After fitting has been done for both helicity states, the longitudinal asymmetry for each run has been obtained as

$$P = \frac{1}{f_n}\frac{\sigma_{p+} - \sigma_{p-}}{\sigma_{p+} + \sigma_{p-}} \tag{4.33}$$

$$= \frac{1}{f_n}\frac{A^+ - A^-}{2 + A^+ + A^-}, \tag{4.34}$$

where f_n is the neutron polarization for each run.

This procedure has been carried out for all the runs. The asymmetry P_k and its error δP_k have been obtained for each run k.

A typical example of the distribution of the values obtained from individual runs is shown in Figure 4.6.

The asymmetry for each resonance has been obtained by averaging P_k's with weights given by $1/(\delta P_k)^2$, where δP_k is the statistical error of P_k.

$$\bar{P} = \sum_{k=1}^{N} \frac{P_k}{(\delta P_k)^2} \Big/ \sum_{k=1}^{N} \frac{1}{(\delta P_k)^2}. \tag{4.35}$$

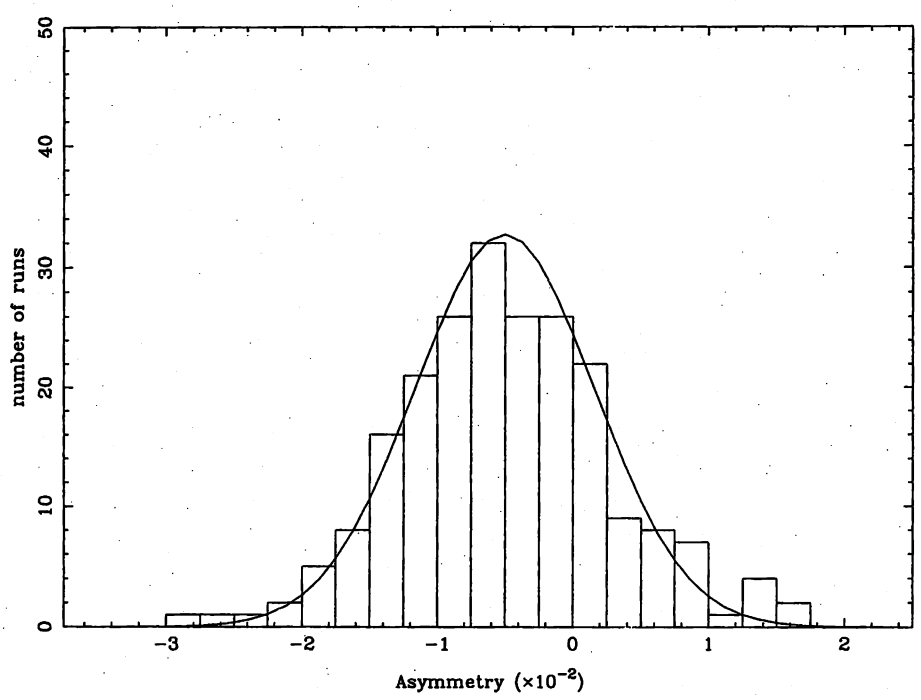

Figure 4.6: A histogram of the value of longitudinal asymmetry obtained in each run for the 92.1eV p-wave resonance of ^{121}Sb. The total number of runs is 218. The longitudinal asymmetry $\bar{P}$ and its error $\delta\bar{P}$ for this resonance has been determined to be $(-5.04 \pm 0.45) \times 10^{-3}$ (before correction of efficiency of spin flipper). The solid line shows the Gaussian curve with the mean value of $\bar{P}$ and the standard deviation $\sqrt{218} \times \delta\bar{P}$.

The statistical error of the asymmetry for all the runs has been calculated as

$$\frac{1}{(\delta\bar{P})^2} = \sum_{k=1}^{N} \frac{1}{(\delta P_k)^2}. \tag{4.36}$$

The Gaussian curve with the mean value $\bar{P}$ and standard deviation $\sqrt{N} \times \delta\bar{P}$ are also shown in Figure 4.6. The magnitude of the variance obtained by this method has been compared with that obtained from the number of neutrons on the resonances, and found to be consistent to each other.

Possible sources of the systematic errors on asymmetries are shown below.

The neutron polarization f_n has been obtained from the NMR amplitude of the polarized proton filter. The NMR system was calibrated by the "transmission enhancement" method. The error of the neutron polarization has been estimated to be about 3%.

Analytical calculation of the efficiency of the spin flipper used for the experiment was done by Bowman et al.[62]. The efficiency has been found to be a function of the neutron energy E_n, beam radius R, magnetic field B and the length of the field L. The efficiency has been calculated with $B = 100G$, $L = 2m$ and $R = 4cm$. The uncertainties of B, R and L have resulted in the uncertainties of the efficiency. Assuming B and L had 5% uncertainties, the error has been estimated to be about (0.1$\sim$ 0.6)%, which depends on the neutron energy.

The fitting routine gives systematic errors if the routine does not reproduce the transmission spectrum well. Since the multi-level formula has been used to calculate the neutron cross sections and the proper response function has been used for the energy resolution of the beam line in FITXS, the errors have been much reduced compared to the ones in the old analysis code in which polynomials were used for the envelope of transmission spectra near p-wave resonances. The accuracy of fitting has been estimated by comparing the observed number of neutrons in the resonance and calculated ones obtained with FITXS. The error for each resonance is about (0.2 $\sim$ 5)% which depends on the resonances.

4.3.4 Extraction of Weak Spreading Width

After the longitudinal asymmetries have been obtained, the likelihood analysis described in Section 4.2 has been applied to extract the weak spreading width for

each nucleus. The energies, neutron widths and spins for s-wave resonances have been obtained from ENDF evaluations[82] for ^{127}I, and from JENDL evaluations[83] for ^{121}Sb and ^{123}Sb. These data have been retrieved from the National Nuclear Data Center (NNDC) Online Service. The experimental results of resonance energies and neutron widths have been used for the p-wave resonances. The spins and partial neutron widths of p-wave resonances are unknown. Thus Equation (4.29) has been used as the likelihood function of Γ_W obtained from the asymmetries.

The probability p_J for the p-wave resonance to have spin J has been calculated using the spin cutoff parameter σ_c[86].

$$\begin{aligned} p_J &= f(J)/\sum_J f(J), \\ f_J &\equiv e^{-J^2/2\sigma_c^2} - e^{-(J+1)^2/2\sigma_c^2} \end{aligned} \tag{4.37}$$

The σ_c was studied for many nuclei by Egidy et al[87], and its smooth dependence on the mass number A was found.

$$\sigma_c = 0.98A^{0.29} \tag{4.38}$$

Using these formula, p_J has been calculated for ^{121}Sb, ^{123}Sb and ^{127}I. The values used in the analysis are listed in Table 4.4.

	Probabilities p_J			
Nucleus	J=I−3/2	J=I−1/2	J=I+1/2	J=I+3/2
^{121}Sb (I=5/2)	0.171	0.251	0.290	0.288
^{123}Sb (I=7/2)	0.231	0.267	0.266	0.236
^{127}I (I=5/2)	0.170	0.250	0.290	0.290

Table 4.4: Probabilities p_J's of p-wave resonances for all possible J's

The parameter a in Equtaion (4.29) represents the square root of the ratio of the p-wave strength functions $S^1_{1/2}$ and $S^1_{3/2}$. The values of $S^1_{1/2}$ and $S^1_{3/2}$ for ^{121}Sb, ^{123}Sb and ^{127}I are obtained by the procedure described in Appendix A. The value $a = 0.652$ has been used for ^{127}I, $a = 0.657$ has been used for ^{121}Sb and ^{123}Sb.

The average level spacings for ^{121}Sb, ^{123}Sb and ^{127}I have been obtained from ENDF and JENDL evaluations. The values used in the analysis are listed in Table 4.5.

Nucleus	Level spacing D_J (eV) $J=I-1/2$	$J=I+1/2$
^{121}Sb (I=5/2)	27.5	22.9
^{123}Sb (I=7/2)	66.6	58.9
^{127}I (I=5/2)	22.2	23.2

Table 4.5: Level spacings of resonances for spin J's

Using the parameters given above, the likelihood function of Γ_W given by the product of Equation (4.29), and the best values of Γ_W are extracted.

Chapter 5

Results and Discussion

5.1 Asymmetries and Weak Spreading Widths of ^{121}Sb, ^{123}Sb, and ^{127}I

The asymmetries of the p-wave resonances for the ^{121}Sb, ^{123}Sb and ^{127}I targets have been obtained by the procedure described in Section 4.3.3. These values and their statistical and systematic errors are listed in Table 5.1, Table 5.2 and Table 5.3. The asymmetries for the p-wave resonances of ^{121}Sb, ^{123}Sb and ^{127}I versus the resonance energies are plotted in Figure 5.1, Figure 5.2 and Figure 5.3 respectively. PNC effects whose significances are larger than 3σ have been observed in five of seventeen p-wave resonances for the ^{121}Sb target, one of five p-wave resonances for the ^{123}Sb target, and seven of twenty p-wave resonances for the ^{127}I target. Since p-wave resonances which have spin $J = I \pm 3/2$ do not interfere with s-wave resonances, it should be noted that about one half of the p-wave resonances can not have PNC effect. Among all the twelve resonances with asymmetries found for the ^{121}Sb, ^{123}Sb and ^{127}I targets, seven resonances have positive asymmetries and five resonances have negative asymmetries.

On the basis of the statistical treatment of weak matrix element described in Chapter 2, the weak spreading widths have been extracted by the likelihood analysis. The likelihood functions of Γ_W deduced from the asymmetries of ^{121}Sb, ^{123}Sb and ^{127}I are plotted in Figure 5.4, Figure 5.5 and Figure 5.6 respectively. The obtained values of Γ_W for ^{121}Sb, ^{123}Sb and ^{127}I are $6.45^{+9.72}_{-3.66} \times 10^{-7}$eV, $1.23^{+15.0}_{-0.96} \times 10^{-7}$eV, and $2.05^{+1.94}_{-0.93} \times 10^{-7}$eV respectively. The errors include the statistical errors of asymmetries only. The systematic errors as well as the uncertainties of p_J, strength functions

$S^1_{1/2}$ and $S^1_{3/2}$, resonance parameters are not included. It is the first experimental determination of Γ_W in the mass region of $A \sim 100$ from the asymmetries which have been obtained in the transmission spectra by means of the analysis using FITXS program.

Resonance energy(eV)	Asymmetry ($\times 10^{-3}$)	Errors($\times 10^{-3}$) statistical	systematic	Statistical significance
37.9	0.180	0.155	0.007	1.2
55.2	-1.334	0.186	0.066	**-7.2**
92.1	-5.138	0.458	0.185	**-11.2**
110.7	21.458	0.604	1.208	**35.5**
141.2	12.578	1.167	0.505	**10.8**
174.5	0.447	0.330	0.046	1.4
177.1	0.309	0.671	0.011	0.5
184.7	-0.511	0.330	0.039	-1.5
200.3	-0.298	0.762	0.012	-0.4
228.6	-0.718	0.754	0.033	-1.0
235.9	-0.496	1.557	0.028	-0.3
245.9	0.169	0.446	0.006	0.4
249.0	1.383	0.519	0.063	2.7
261.6	-0.291	0.365	0.011	-0.8
265.8	0.798	0.476	0.039	1.7
269.0	1.794	0.462	0.080	**3.9**
274.9	1.286	0.502	0.044	2.6

Table 5.1: The asymmetries of the p-wave resonances for the ^{121}Sb target. The statistical errors and systematic errors are also shown. Uncertainties of the spin flipper efficiency, NMR calibration and fitting error are included in the systematic error. Bold numbers indicate asymmetries with statistical significances of greater than 3σ.

Resonance energy(eV)	Asymmetry ($\times 10^{-3}$)	Errors($\times 10^{-3}$) statistical	systematic	Statistical significance
176.4	-0.764	0.424	0.029	-1.8
186.1	-0.121	0.349	0.006	-0.3
197.8	-0.219	0.348	0.008	-0.6
202.0	-4.583	1.174	0.176	**-3.9**
225.1	-0.142	0.448	0.006	-0.3

Table 5.2: The asymmetries of the p-wave resonances for the ^{123}Sb target. The statistical errors and systematic errors are also shown. Uncertainties of the spin flipper efficiency, NMR calibration and fitting error are included in the systematic error. Bold numbers indicate asymmetries with statistical significances of greater than 3σ.

Resonance energy(eV)	Asymmetry ($\times 10^{-3}$)	Errors($\times 10^{-3}$) statistical	systematic	Statistical significance
7.5	1.328	1.410	0.059	0.9
10.3	-0.040	0.252	0.001	-0.2
13.9	0.124	0.398	0.005	0.3
24.6	16.456	1.604	0.879	**10.3**
52.2	1.003	1.839	0.075	0.5
53.8	2.374	0.192	0.104	**12.3**
64.0	0.580	0.196	0.022	2.9
85.8	2.410	0.218	0.075	**11.1**
101.1	0.980	0.313	0.035	**3.1**
126.0	-4.822	1.591	0.156	**-3.0**
134.1	-0.215	0.183	0.011	-1.2
136.9	7.312	0.158	0.250	**46.2**
145.7	0.007	0.336	0.012	0.0
153.6	0.128	0.173	0.005	0.7
223.4	-0.102	1.344	0.005	-0.1
256.8	0.453	0.404	0.019	1.1
274.7	-3.167	1.461	0.112	-2.2
282.1	-4.673	5.304	0.160	-0.9
351.9	-5.389	0.638	0.205	**-8.4**
353.3	0.467	0.618	0.018	0.8

Table 5.3: The asymmetries of the p-wave resonances for the ^{127}I target. The statistical errors and systematic errors are also shown. Uncertainties of the spin flipper efficiency, NMR calibration and fitting error are included in the systematic error. Bold numbers indicate asymmetries with statistical significances of greater than 3σ.

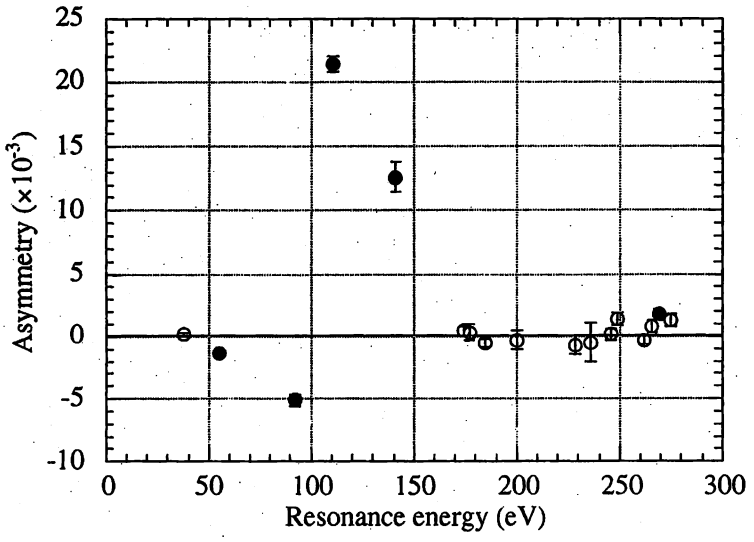

Figure 5.1: The values of asymmetries in the p-wave resonances of ^{121}Sb versus resonance energies are plotted. Closed circles show the asymmetries whose statistical significances are greater than 3σ. The error bars show the statistical errors only.

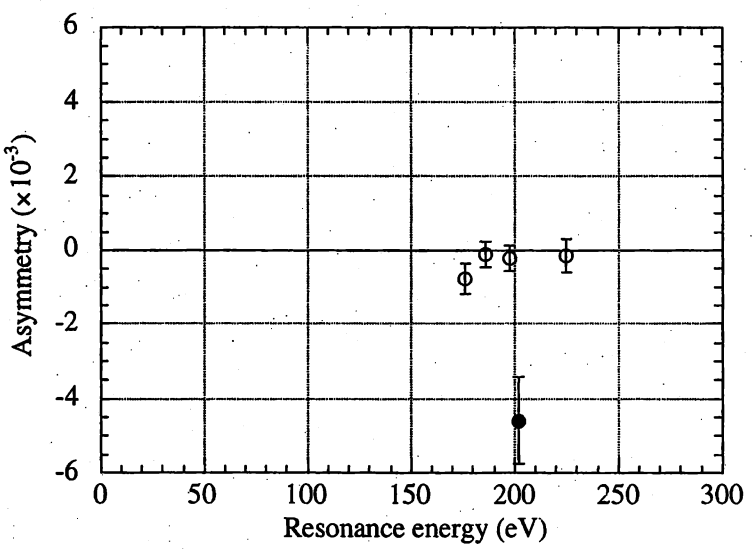

Figure 5.2: The values of asymmetries in the p-wave resonances of ^{123}Sb versus resonance energies are plotted. A Closed circle shows the asymmetry whose statistical significance is greater than 3σ. The error bars show the statistical errors only.

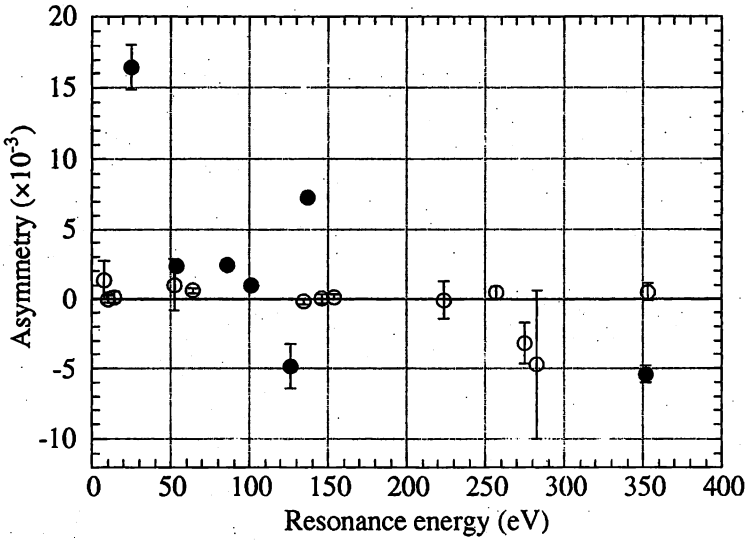

Figure 5.3: The values of asymmetries in the p-wave resonances of ^{127}I versus resonance energies are plotted. Closed circles show the asymmetries whose statistical significances are greater than 3σ. The error bars show the statistical errors only.

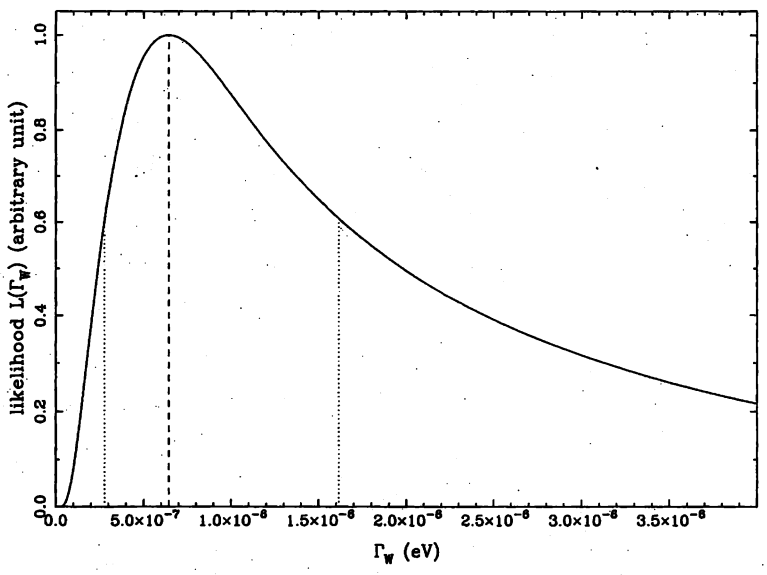

Figure 5.4: Likelihood function of Γ_W for ^{121}Sb deduced from the asymmetries listed in Table 5.1. The dashed line shows the best value of Γ_W which maximize the likelihood function. The dotted line shows the values which satisfy Equation 4.22. Γ_W is calculated to be $6.45^{+9.72}_{-3.66} \times 10^{-7}$eV.

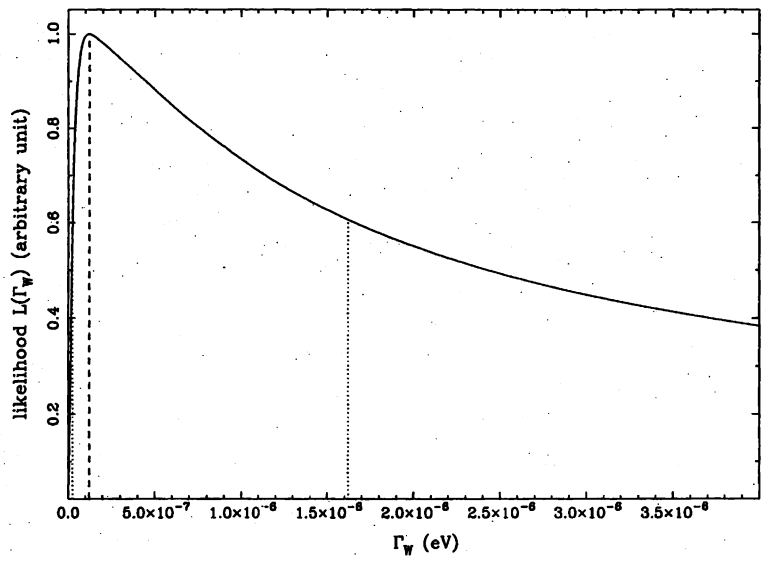

Figure 5.5: Likelihood function of Γ_W for ^{123}Sb deduced from the asymmetries listed in Table 5.2. The dashed line shows the best value of Γ_W which maximize the likelihood function. The dotted line shows the values which satisfy Equation 4.22. Γ_W is calculated to be $1.23^{+15.0}_{-0.96} \times 10^{-7}$eV.

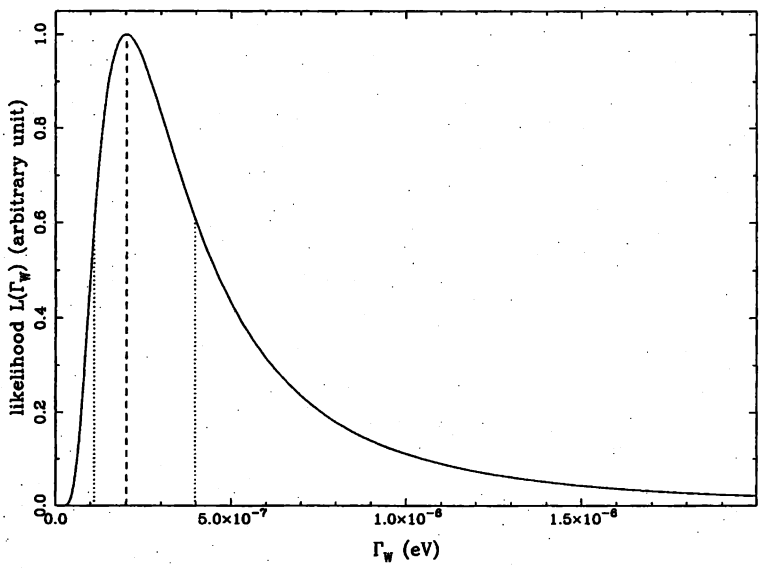

Figure 5.6: Likelihood function of Γ_W for ^{127}I deduced from the asymmetries listed in Table 5.3. The dashed line shows the best value of Γ_W which maximize the likelihood function. The dotted line shows the values which satisfy Equation 4.22. Γ_W is calculated to be $2.05^{+1.94}_{-0.93} \times 10^{-7}$eV.

5.2 Discussion

The number of asymmetries observed in ^{121}Sb, ^{123}Sb and ^{127}I as well as the one observed in other nuclei by TRIPLE Collaboration are listed in Table 5.4. The asymmetries in ^{107}Ag, ^{109}Ag, ^{115}In and ^{232}Th have been obtained by the old analysis code (PVIO). The asymmetries in ^{106}Pd and ^{108}Pd have been measured by the capture γ-ray method.

Target	Number of resonances with asymmetries			References
	total	plus	minus	
^{107}Ag	7	4	3	[79]
^{109}Ag	6	4	2	[79]
^{106}Pd	1	0	1	[88]†
^{108}Pd	0	0	0	[88]†
^{115}In	6	3	3	[79]
^{121}Sb	5	3	2	(this work)
^{123}Sb	1	0	1	(this work)
^{127}I	7	5	2	(this work)
^{131}Xe	1	0	1	[89]
^{232}Th	8	8	0	[80]
^{238}U	5	3	2	[88]

Table 5.4: Number of the p-wave resonances which show parity violating asymmetries observed by TRIPLE Collaboration. The asymmetries whose significances are greater than 3σ are listed. † indicates that the experiment was done by the γ-ray detection method.

These results make it clear that the enhancement of parity violation in the p-wave resonances is not phenomena only in a resonance for ^{139}La and few other targets, but is a prevalent feature of p-wave resonances located near s-wave resonances in the case of neutron absorption reactions.

The enhancement mechanism of PNC effect in compound nuclei can be explained in the framework of the s-p mixing model described in Section 2.1. In this model, the statistical nature of compound nuclei plays a fundamental role in the enhancement mechanism, and the weak matrix element is assumed to be a random variable according to a Gaussian distribution. Therefore the random signs of asymmetries are predicted if the measurements of asymmetries are made over many resonances.

As shown in Table 5.4, the signs of asymmetries have found to be randomly

distributed with an exception of ^{232}Th nucleus. It supports the enhancement mechanism based on the statistical nature of the compound nuclei.

The systematic bias on the signs of the asymmetries in ^{232}Th can be explained by a special mechanism applicable only for the ^{232}Th nucleus. Such a possibility has been investigated by several researchers. Auerbach et al.[43] suggested that peer-shape deformation of the ^{233}Th nucleus gives parity doublets which act as doorway states and leads to the common sign. Desplanques et al.[45] proposed that deformed states are accidentally degenerated and behave as a doorway state. In either case, the signs of asymmetries flip when the resonance energy surpasses the energy of the doorway state. The measurement of asymmetries in high energy region will give light on the problem.

In Table 5.5 Γ_W's for ^{121}Sb, ^{123}Sb and ^{127}I as well as the ones for other nuclei obtained by TRIPLE Collaboration are listed. The values for ^{107}Ag, ^{109}Ag, ^{115}In and ^{232}Th have been derived from the asymmetries obtained using the PVIO analysis code. The values for ^{106}Pd and ^{108}Pd have been derived from the asymmetries measured by the capture γ-ray method. It has been found that most of them have approximately the same value within the errors except the one for ^{106}Pd. In the case for ^{106}Pd, the value of Γ_W is strongly influenced by the large asymmetry at the resonance at 593.4eV. A possible explanation is that the observed 593.4-eV resonance is doublets which consist of an s-wave resonance and a small unresolved p-wave resonance. The asymmetry may arise from this unresolved p-wave resonance[88].

The weak spreading width Γ_W was estimated to be of the order of 10^{-7}eV in Section 2.2 on basis of the statistical nature of compound nuclei. The values in Table 5.5 are in agreement with the one obtained from the estimation above.

The Γ_W for ^{121}Sb, ^{123}Sb and ^{127}I obtained in this work as well as Γ_W for other nucleis obtained by the transmission method are plotted as a function of the mass number A in Figure 5.7. It is shown in the figure that there is no strong dependence of Γ_W on the mass number A in the mass region arounds A=100 and A=230. More precise determination of Γ_W is necessary for studying the detail of the mass dependence of Γ_W.

It should be noted that the present accuracy of Γ_W is mainly limited by the lack of the knowledge of spins of p-wave resonances. If we use Equation (4.28) instead of Equation (4.29), we can reduce the width of the likelihood function $L(\Gamma_W)$ and can

Target	Γ_W ($\times 10^{-7}$ eV)	References
^{107}Ag	$5.5^{+5.3}_{-2.4}$	[79]
^{109}Ag	$7.0^{+18.9}_{-5.2}$	[79]
^{106}Pd	48^{+67}_{-39}	[88]†
^{108}Pd	< 7.0	[88]†
^{115}In	$0.94^{+0.84}_{-0.40}$	[79]
^{121}Sb	$6.45^{+9.72}_{-3.66}$	(this work)
^{123}Sb	$1.23^{+15.0}_{-0.96}$	(this work)
^{127}I	$2.05^{+1.94}_{-0.93}$	(this work)
^{232}Th	$5.5^{+5.6}_{-3.0}$	[39]
	$4.14^{+2.63}_{-1.50}$	[80]
^{238}U	$0.9^{+1.9}_{-0.5}$	[40]
	$1.35^{+0.97}_{-0.64}$	[88]

Table 5.5: Weak spreading widths Γ_W obtained by the TRIPLE Collaboration. The values for ^{107}Ag, ^{109}Ag, ^{113}Cd, ^{115}In and ^{232}Th have been derived from the asymmetries obtained using the old analysis code (PVIO). † indicates that the experiment was done by the γ-ray detection method.

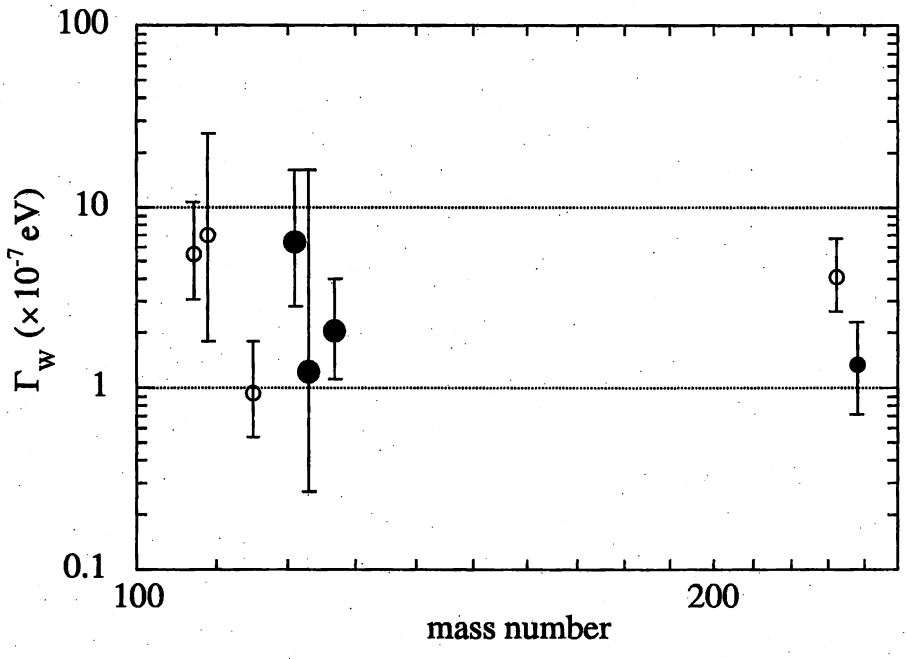

Figure 5.7: Weak spreading width Γ_W versus mass number A. The results of this work is indicated with large circles. Only the data obtained by the transmission method are plotted. Closed circles show the asymmetries obtained by FITXS, whereas open circles correspond to the asymmetries obtained by old PVIO code.

improve the error of Γ_W. A measurement to determine the spins of p-wave resonances of various nuclei used in this experiment is currently performed at GELINA neutron source at Geel, Belgium. They apply the low-level population method[64] by means of capture γ-ray spectroscopy with Ge detectors to determine the spins of p-wave resonances. Using the spin assignments obtained from Geel experiment, we will be able to reduce the errors of Γ_W. In addition, using the new method of fitting the data (FITXS) which has been developped in this work, more precise determinations of the asymmeties for other target nuclei than ^{121}Sb, ^{123}Sb, ^{127}I and ^{238}U will be able to be made. Then we will have clearer picture on the mass dependence of Γ_W.

Chapter 6

Conclusion

In order to study the origin of large enhancement of the parity violation effect in neutron resonance reactions, we have measured asymmetries of the transmissions of longitudinally polarized neutrons in wide energy region on various nuclei around $A \sim 100$ and $A \sim 230$ region. In this paper, we describe the experimental procedure and the results with the ^{121}Sb, ^{123}Sb and ^{127}I targets. Then we discuss the statistical treatment of parity violating effects in neutron resonance reactions using the data with above targets and other data obtained by TRIPLE Collaboration.

The experiment was performed in the energy region of 1eV to 350eV using the pulsed neutron beam at LANSCE. We constructed and used a polarized proton filter for polarizing the neutron beam and a neutron spin flipper with a smoothly changing transverse magnetic field to reverse the direction of the neutron spin frequently. A neutron detector which consisted of liquid scintillator arrays doped with ^{10}B was developed for this experiment. To measure the asymmetries with high statistics, analog signals whose voltages were proportional to the counting rates of the detector were digitized to obtain the intensity of transmitted neutrons.

A new computer code, FITXS, has been developed for the analysis of the experimental data. The multi-level Reich-Moore formula has been used to calculate the neutron cross sections including the interference between many s-wave resonances and potential scattering. It employs proper response functions to describe broadening effects due to the time structure of neutron beam and Doppler broadening. The response of the detector system and the electric devices are also included.

By fitting the p-wave resonances with this code, the longitudinal asymmetries have been extracted for resonances of ^{121}Sb, ^{123}Sb and ^{127}I. Five of seventeen p-wave

resonances in ^{121}Sb, one of five p-wave resonances in ^{123}Sb and seven of twenty p-wave resonances in ^{127}I have been found to have finite asymmetries with statistical significances greater than 3σ. From the data on the above targets and other data obtained by TRIPLE Collaboration, it is concluded that the enhancement of parity violation in the p-wave resonances is not the phenomena only for few resonances but is a prevalent feature of p-wave resonances located near s-wave resonances in the case of neutron absorption reactions.

The signs of these asymmetries for ^{121}Sb, ^{123}Sb and ^{127}I have been found to be random. Seven of twelve asymmetries are positive, while five of twelve asymmetries are negative. No evidence has been found for the "sign effect" which was reported in the asymmetries on ^{232}Th earlier, if all the data of TRIPLE Collaboration have been taken into account.

Based on the statistical view of the compound nucleus, the weak matrix element has been assumed to be a random variable according to a Gaussian distribution with variance M^2. The weak spreading width $\Gamma_W = 2\pi M^2/D$, where D is the level density of the nuclei, has been introduced, and its magnitude has been estimated to be of the order of 10^{-7}. The Γ_W's for ^{121}Sb, ^{123}Sb and ^{127}I have been determined from the experimental values of asymmetries to be $6.45^{+9.72}_{-3.66} \times 10^{-7}$eV, $1.23^{+15.0}_{-0.96} \times 10^{-7}$eV, and $2.05^{+1.94}_{-0.93} \times 10^{-7}$eV respectively. These values as well as the ones obtained from the other TRIPLE data are consistent with each other and agree with estimated value given above. The agreement makes the treatment of the parity violating effect on the basis of the statistical nature of compound nucleus quite convincing.

The mass dependence of Γ_W has been investigated with all the TRIPLE data obtained by the transmission measurement. No strong dependence on the target mass number has been observed, although more precise determination of Γ_W is necessary for studying it in detail.

In summary, we have confirmed that the large enhancement of parity violating effect originates in the interference between p-wave and s-wave resonances.

Acknowledgement

This is my great pleasure to take this opportunity to address my thanks to many people who have supported me to complete this work.

I would like to express my sincere gratitude to Prof. Akira Masaike, who introduced me low energy neutron physics as well as many interesting aspects of physics in wide area. Without his continuous supports, encouragements and insightful advice this work would never have been completed. I am very grateful to Dr. David Bowman, who has been the spokesperson of the TRIPLE collaboration. I have greatly benefited from his invaluable advice and suggestions during all the stage of the experiment and the analysis. I also thank for his warm hospitality during my stay in LANSCE. I would like to thank Prof. Hideto En'yo for discussion for this work. His dedicated attitude for experimental physics affected me much. I am also grateful to Prof. Ken'ichi Imai for his interest in this work and advice. I thank Dr. Haruhiko Funahashi. His interest for wide range of physics has inspired me much.

I sincerely thank to all the members of TRIPLE Collaboration. I am very grateful to Dr. Seppo Penttila for his dedication to the experiment. Without his hard work, the experiment has not be done. I would thank Dr. Eduard Sharapov for his kind and knowledgeable advice on the experiment and the analysis. I thank Dr. Susan Seestrom whose enthusiasm for the experiment has led the collaboration. Special thanks should be delivered to Dr. Yi-Fen Yen who worked hard for every aspects of the experiment. I thank Dr. Bret Crawford, Mr. Tomohito Haseyama, Dr. Lisa Lowie and Dr. Sharon Stephenson for their help on running experiment, discussion on physics and analysis. Especially thanks are due to Bret for his work on the study of response function and help for the analysis code. We, graduate students, have developed good friendship, which made the execution of the experiment enjoyable.

The experience at PEN collaboration has benefited me much for this work. I express thanks to Prof. Yasuhiro Masuda who was the spokesperson for the exper-

iment. I am very grateful to Dr. Hirohiko Shimizu, who has been a role model for me. I thank Prof. Koichiro Asahi, Dr. Kenji Sakai and Dr. Hiromi Sato. I have learned much from their works and the discussion with them.

I wish to thank all the members of the group for particles and nuclei at Kyoto University. Under the guidance of Profs. A. Masaike, H. En'yo and H. Funahashi, the activities of the group cover wide area of physics such as particle and nuclear physics, astrophysics, and solid state physics. I really enjoyed intellectual and energetic discussion on various topics. In particular, I want to express my thanks for my friends Dr. Masataka Iinuma and Mr. Ken'ichi Okumura. We worked together on experiment, shared interests on fundamental physics and have affected much to each other.

I thank Ms. Mari Hayashi for her secretarial works and her hospitality in our group. I also would like to thank Ms. Michiyo Masaike for her warm encouragement and supports for years.

Finally, I express my great thanks for my parents for their understandings and continuous support during my time in graduate study.

This work has been partially supported by Fellowships of the Japan Society for the Promotion of Science for Japanese Junior Scientists and by the Grant-in-Aid for Scientific Research from the Ministry of Education, Science, Sports and Culture of Japan under program numbers 04044082, 04244101 and 06044111.

Appendix A

Neutron Strength Functions

The strength function S^l for the orbital angular momentum l of the incident neutron is given as[64]

$$S^l \equiv \frac{1}{(2l+1)} \frac{1}{\Delta E} \sum_J g_J \Gamma^l_n, \tag{A.1}$$

where J is the spin of the resonance, Γ^l_n is the reduced neutron width of the resonance and g_J is the statistical weight factor $(2J+1)/(2(2I+1))$. The summation is carried over the neutron resonances in the energy interval ΔE, where $\Delta E \gg \Gamma_n$.

The s-wave strength function S^0 is written as

$$S^0 = \frac{1}{\Delta E} \sum g\Gamma^0_n = \frac{\langle g\Gamma^0_n \rangle}{D^0}, \tag{A.2}$$

where $\langle \Gamma^0_n \rangle$ is the average reduced neutron width for the s-wave resonances and D^0 is the average level spacing of s-wave resonances.

The p-wave strength function depends on the total angular momentum of the incident neutron j owing to the spin-orbit potential of the nuclei. Thus S^1 is written as

$$S^1 = \frac{1}{3} \left[\sum_{J=I-1/2}^{I+1/2} \frac{g_J \langle \Gamma^1_{n\,1/2} \rangle}{D^1_J} + \sum_{J=I-3/2}^{I+3/2} \frac{g_J \langle \Gamma^1_{n\,3/2} \rangle}{D^1_J} \right] \tag{A.3}$$

$$= \frac{1}{3} S^1_{1/2} + \frac{2}{3} S^1_{3/2}, \tag{A.4}$$

where $S^1_{1/2}$ and $S^1_{3/2}$ are the strength functions for $j = 1/2$ channel and $j = 3/2$ channel respectively, Γ^1_{nj} is the reduced partial neutron width of the p-wave resonance, and D^1_J is the average level spacing of p-wave resonances whose spins are J.

Popov and Samosvat developed a method for extracting S^0, $S^1_{1/2}$ and $S^1_{3/2}$ from the differential elastic scattering cross sections which were measured for various

Nucleus	Strength function ($\times 10^{-4}$)			Reference
	S^1	$S^1_{1/2}$	$S^1_{3/2}$	
Pd	3.7 ± 0.4	3.6 ± 1.2	3.7 ± 0.2	[90]
Ag	4.5 ± 0.5	5.8 ± 1.0	3.8 ± 0.4	[91]
Cd	4.2 ± 0.3	6.1 ± 0.9	3.3 ± 0.2	[90]
In	4.1 ± 0.4	7.4 ± 0.9	2.5 ± 0.3	[91]
Sb	3.2 ± 0.4	5.1 ± 1.0	2.2 ± 0.3	[91]

Table A.1: p-wave strength functions for the nuclei of which asymmetries have been measured by TRIPLE Collabration.

nuclei in the mass region of $A \sim 100$ [90][91][92]. The values for the nuclei of which asymmetries have been measured by TRIPLE Collabration are listed in Table A.1. The values $S^1_{1/2} = 5.1 \times 10^{-4}$ and $S^1_{3/2} = 2.2 \times 10^{-4}$ have been used for the analysis for ^{121}Sb and ^{123}Sb data.

Since $S^1_{1/2}$ and $S^1_{3/2}$ for ^{127}I are unknown, they have been estimated by the following way. $S^1_{1/2}$'s, which depend on mass number A, were fitted to a Lorentzian with a peak at $A_{1/2}$, width $\Gamma_{1/2}$ and height $S_{1/2}$. The same procedure was carried for $S^1_{3/2}$.

$$\begin{aligned} S^1_{1/2} &= S_{1/2} \frac{\Gamma^2_{1/2}/4}{(A - A_{1/2})^2 + \Gamma^2_{1/2}/4}, \\ S^1_{3/2} &= S_{3/2} \frac{\Gamma^2_{3/2}/4}{(A - A_{3/2})^2 + \Gamma^2_{3/2}/4}, \end{aligned} \tag{A.5}$$

where $S_{1/2} = 6.0 \times 10^{-4}$, $A_{1/2} = 107$, $\Gamma_{1/2} = 45$, and $S_{3/2} = 5.3 \times 10^{-4}$, $A_{3/2} = 94$, $\Gamma_{3/2} = 40$, were obtained by the fitting. Using above values, the $S^1_{1/2}$ and $S^1_{3/2}$ for ^{127}I have been estimated to be $S^1_{1/2} = 3.3 \times 10^{-4}$ and $S^1_{3/2} = 1.4 \times 10^{-4}$, and have been used for the analysis for ^{127}I data.

Appendix B

Fits for ^{127}I data

In this appendix, the neutron transmission spectra and the differences of the transmission spectra with positive and negative helicities. are shown for all the p-wave resonances of ^{127}I in the energy region from 1eV to 350eV.

The neutron transmission spectra around the p-wave resonances are shown in the upper graphs. All the data are summed up in the spectra. The energies and neutron widths of the p-wave resonances are deduced by fitting the spectra obtained by the FITXS program (see Section 4.3.2). The solid lines show the calculated curves with the best values of the resonance parameters ,which are listed in Table 4.3.

The differences of transmission spectra with positive and negative neutron helicities are shown in the lower graphs. The solid lines show the calculated differences obtained by the FITXS program with the best values of the asymmetries of the p-wave resonances observed in the transmission spectra.

Several resonances of Cd are also seen in the neutron transmission spectra. These are due to the Cd foil placed between the neutron polarizer and the spin flipper (see Section 3.7).

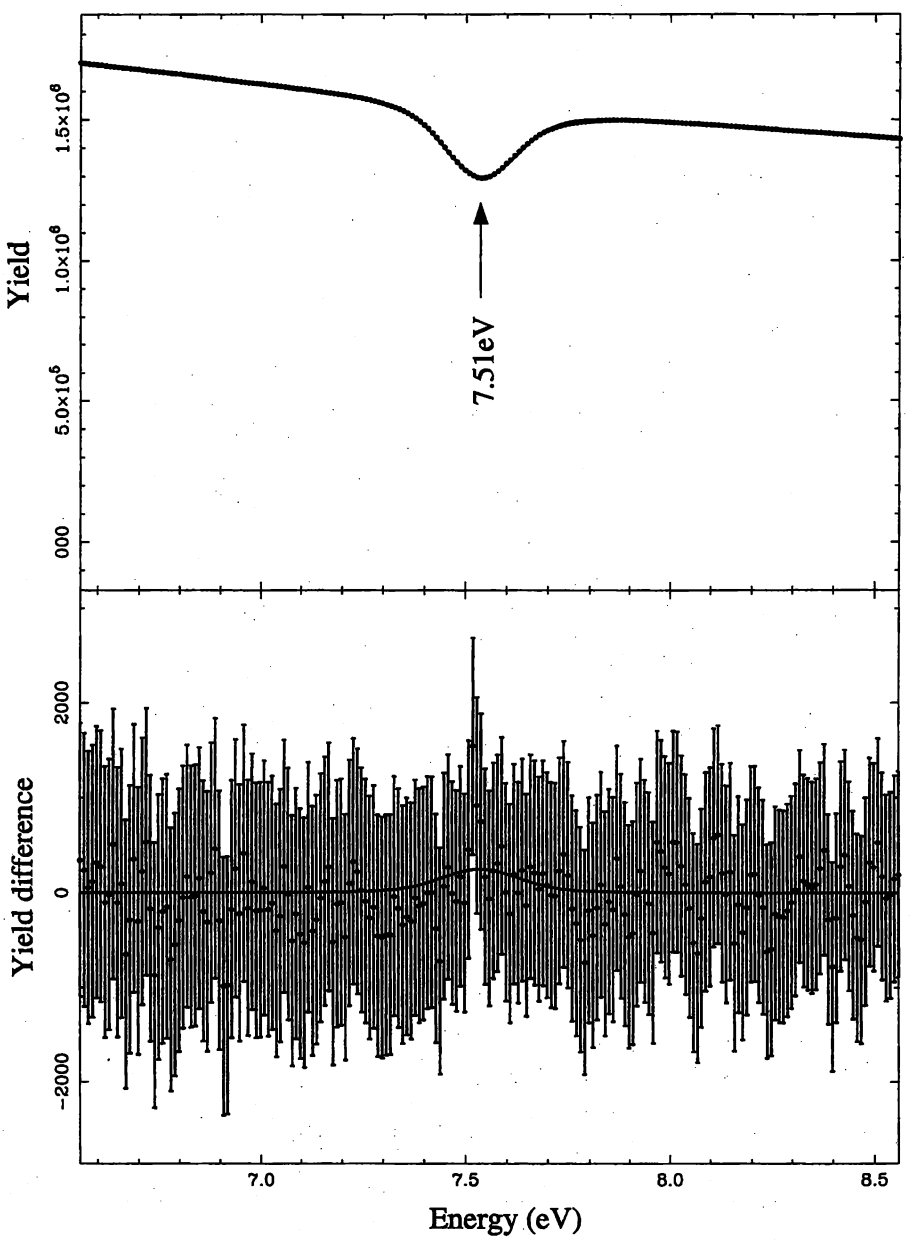

Figure B.1: The spectrum around for the 7.51-eV resonance. The 7.51-eV resonance shows no asymmetry within statistical error.

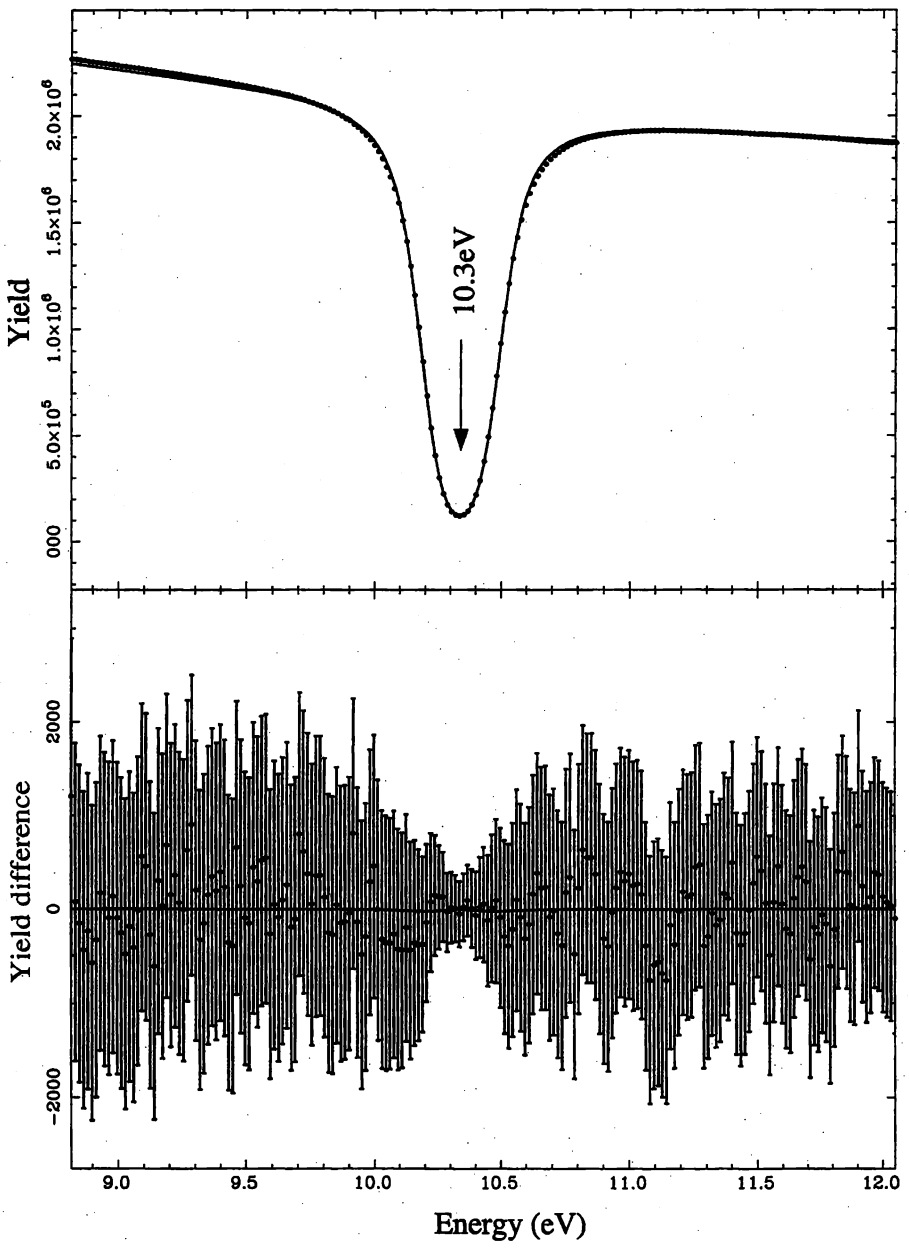

Figure B.2: The spectrum around for the 10.3-eV resonance. The 10.3-eV resonance shows no asymmetry within statistical error.

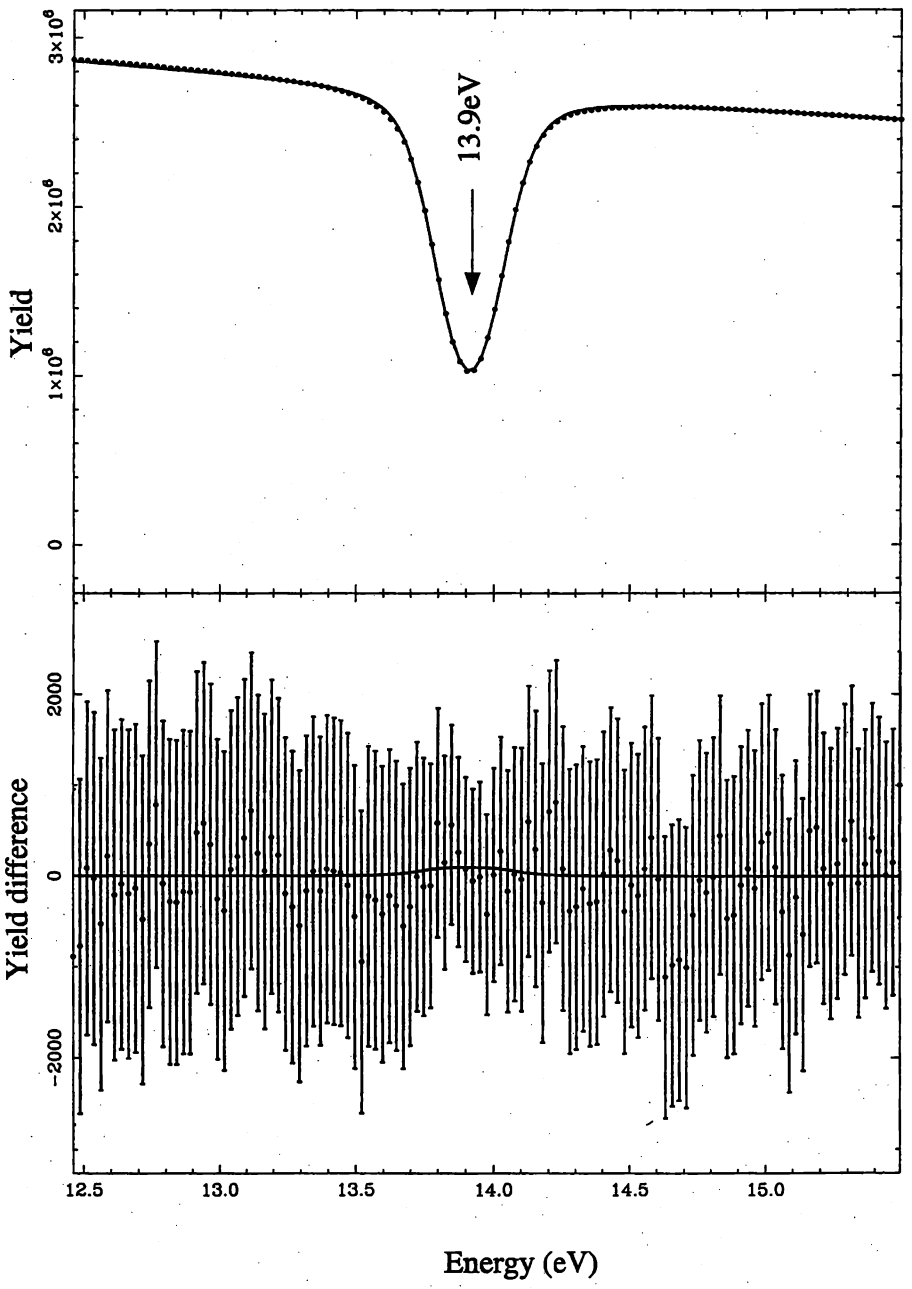

Figure B.3: The spectrum around for the 13.9-eV resonance. The 13.9-eV resonance shows no asymmetry within statistical error.

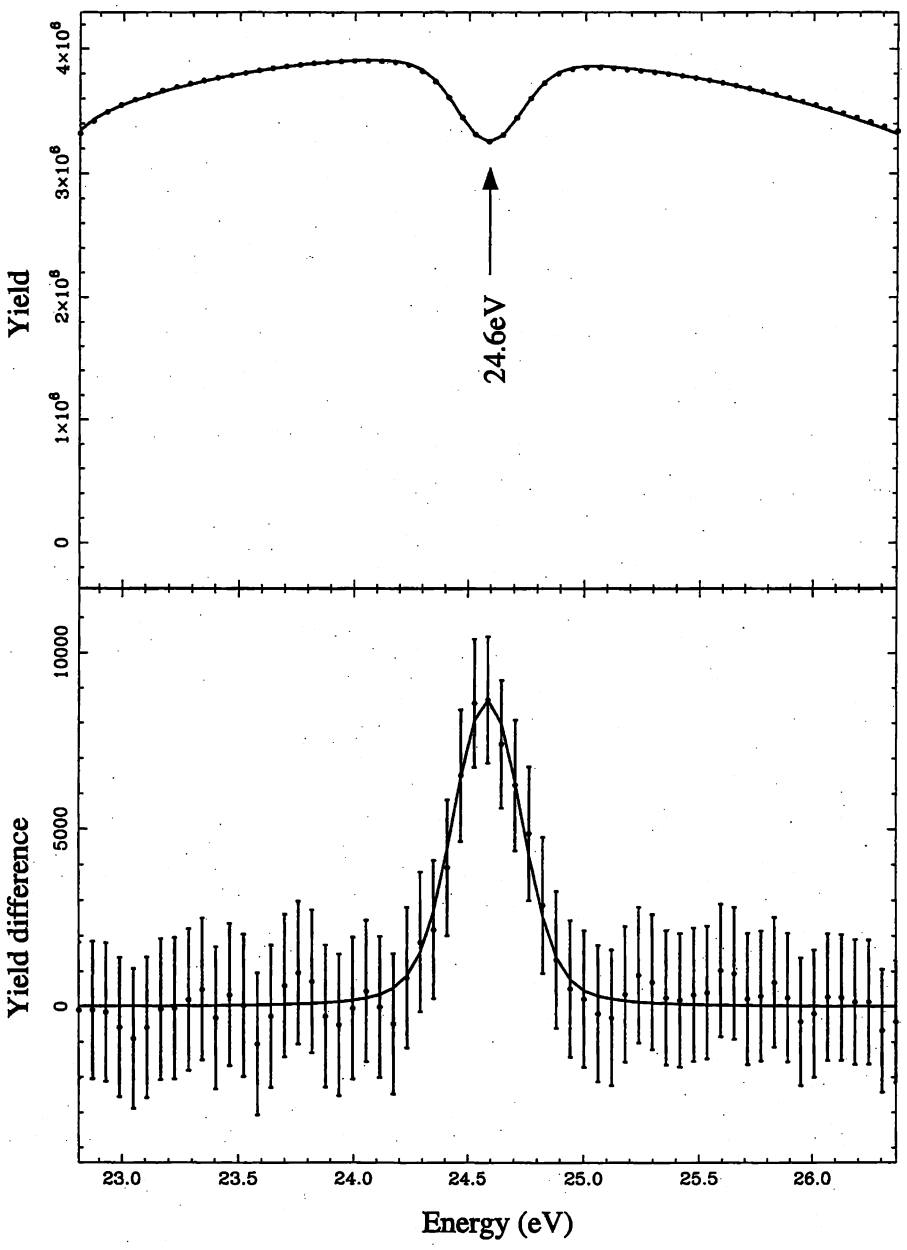

Figure B.4: The spectrum around for the 24.6-eV resonance. The 24.6-eV resonance shows an asymmetry whose statistical significance is 10.3σ.

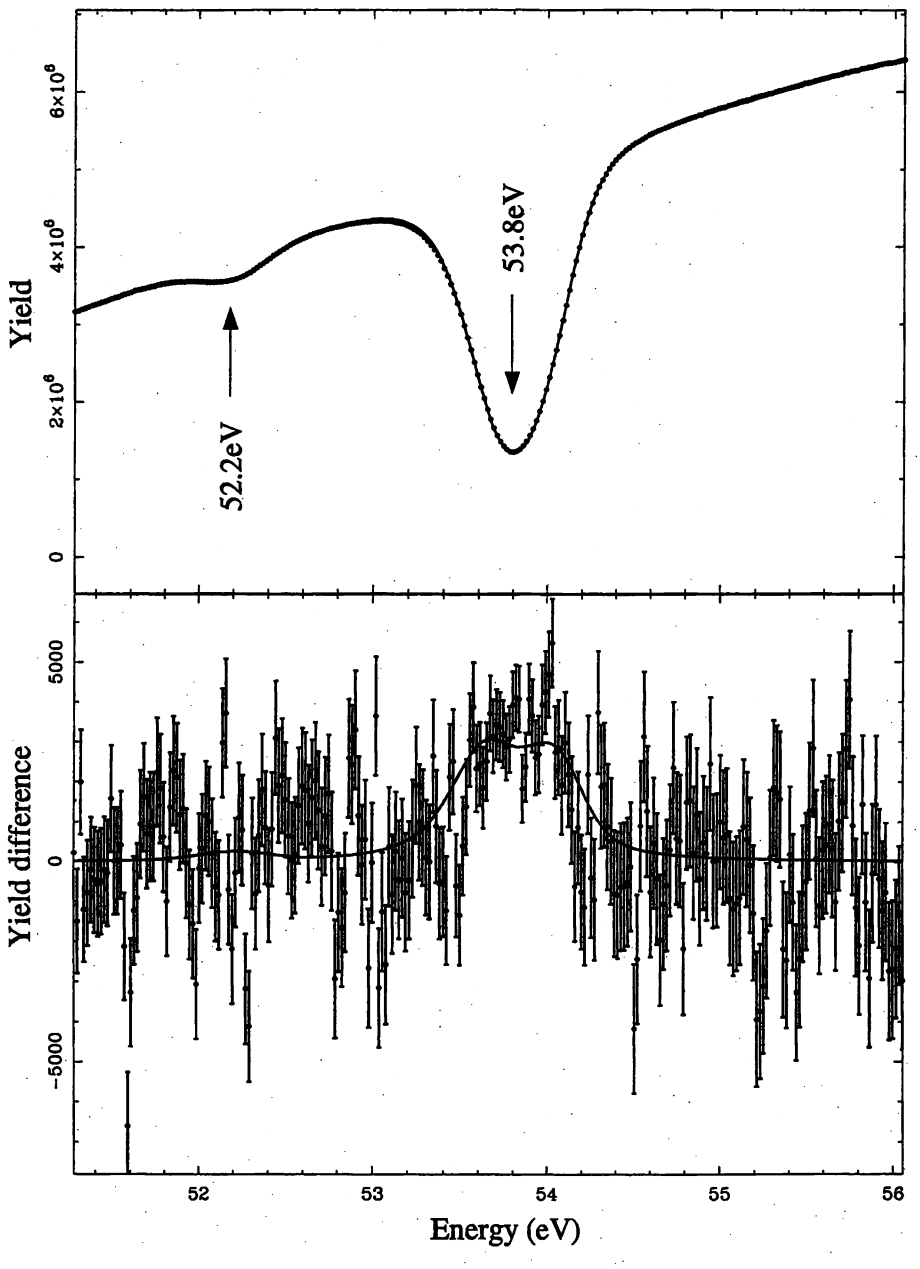

Figure B.5: The spectrum around for the 52.2-eV and 53.8-eV resonances. The 53.8-eV resonance shows a asymmetry whose statistical significance is 12.3σ. The 52.2-eV resonance shows no asymmetry within statistical error. The yield difference is suppressed at the center of the 53.8-eV resonance, since most of the neutrons are absorbed at the center of the resonance.

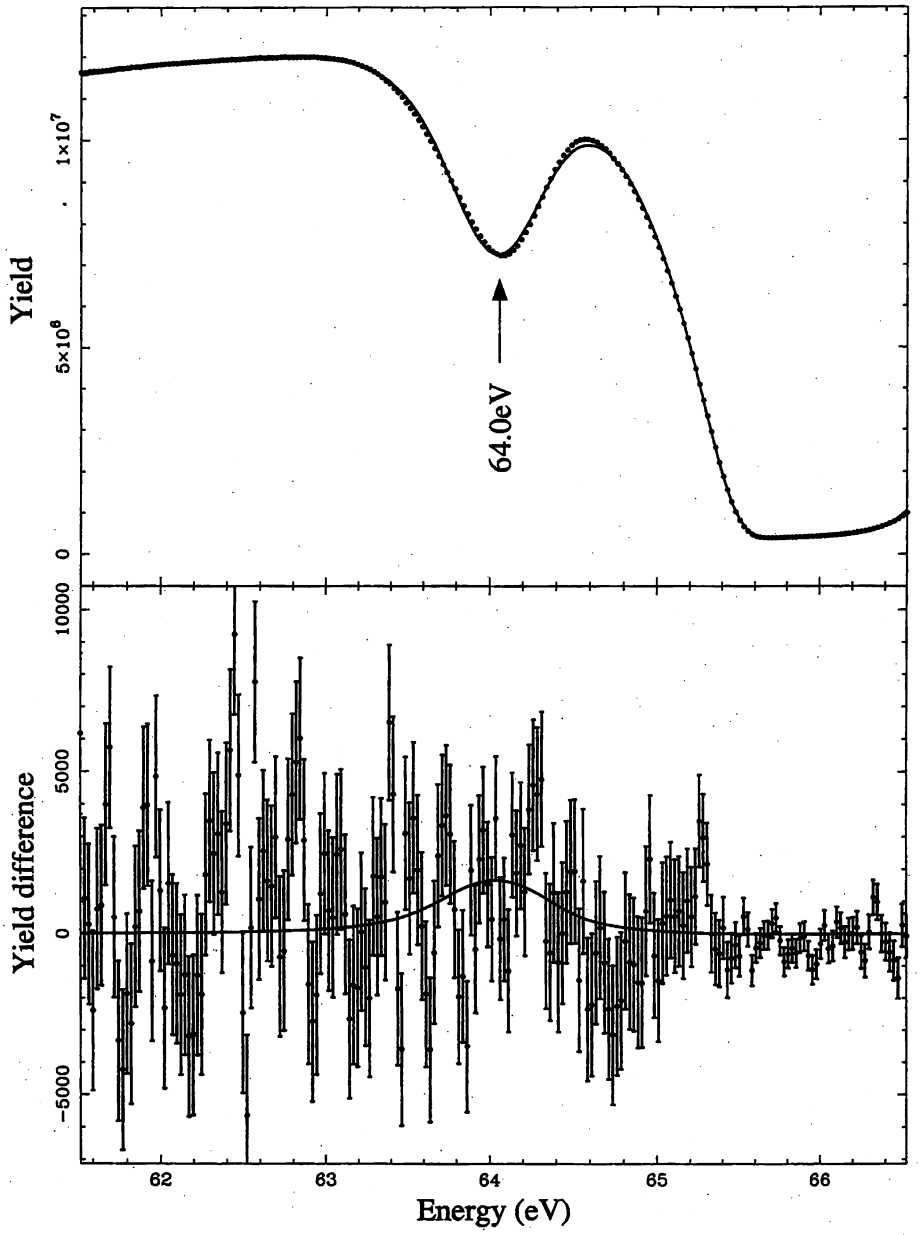

Figure B.6: The spectrum around the 64.0-eV resonance. The statistical significance of the asymmetry of the 64.0-eV resonance is smaller than 3σ.

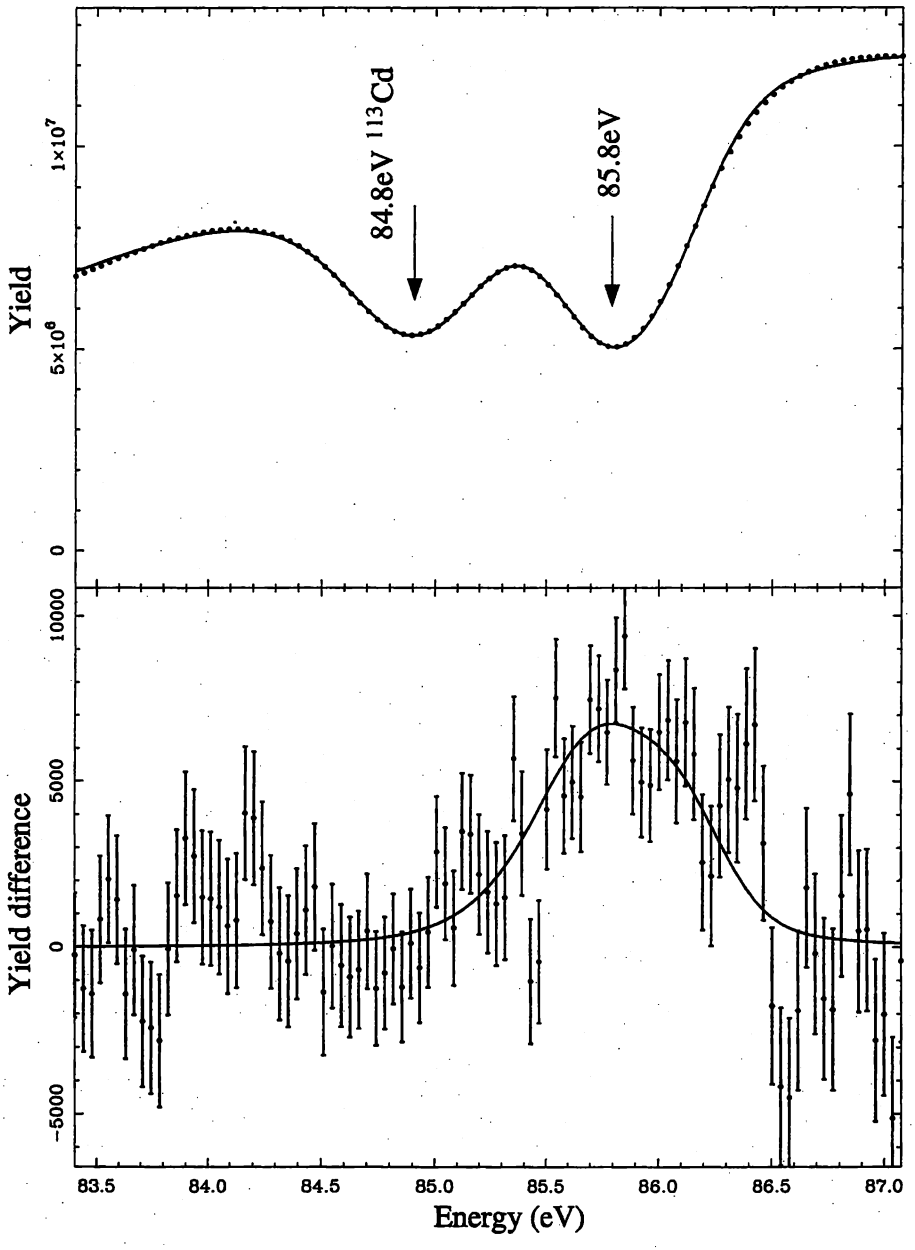

Figure B.7: The spectrum around the 85.8-eV resonance. The neighboring s-wave resonance of ^{113}Cd at 84.8eV is also shown in the spectrum. The 85.8-eV resonance shows a large parity violating asymmetry whose statistical significance is 11.1σ.

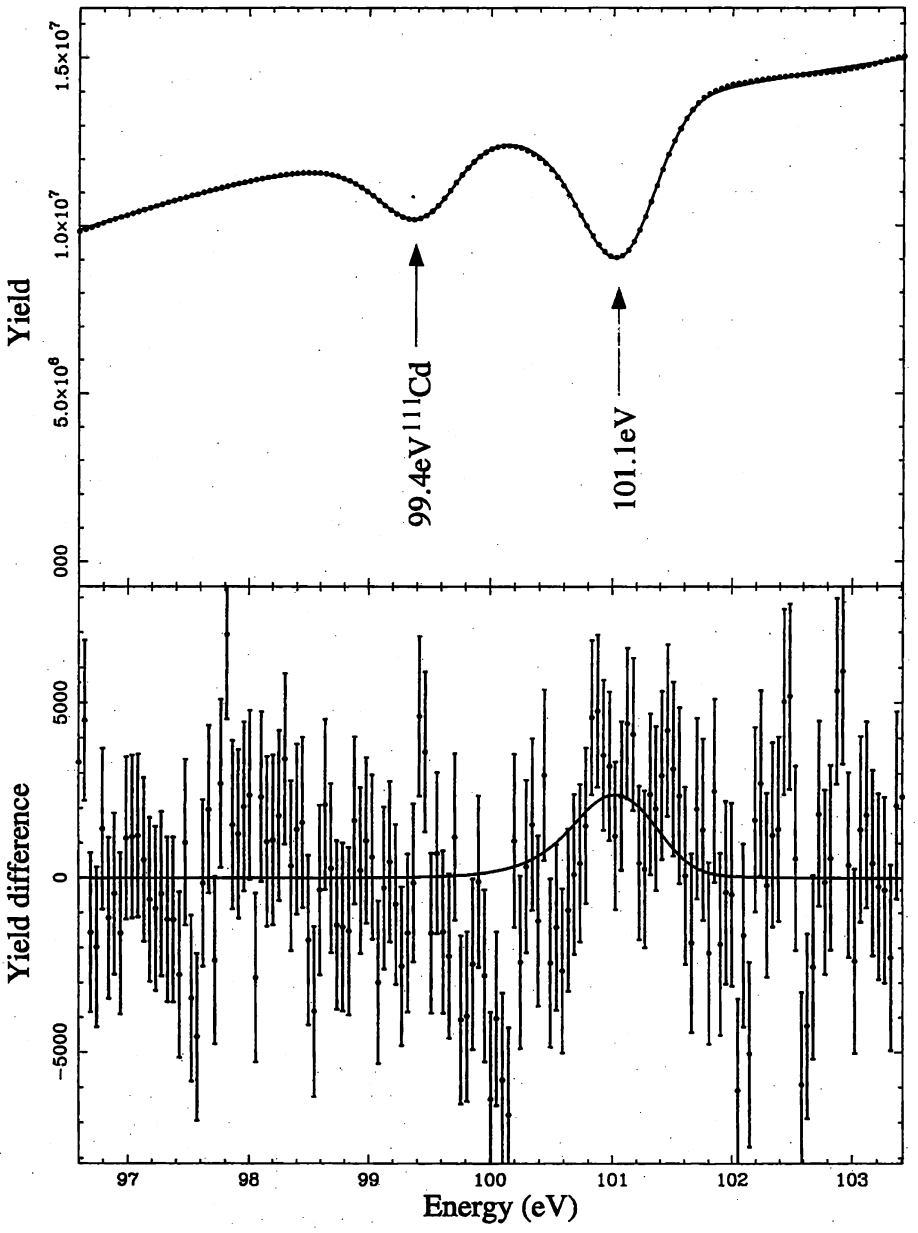

Figure B.8: The spectrum around the 101.1-eV resonance. This analysis gives an asymmetry with statistical significance of 3.1σ.

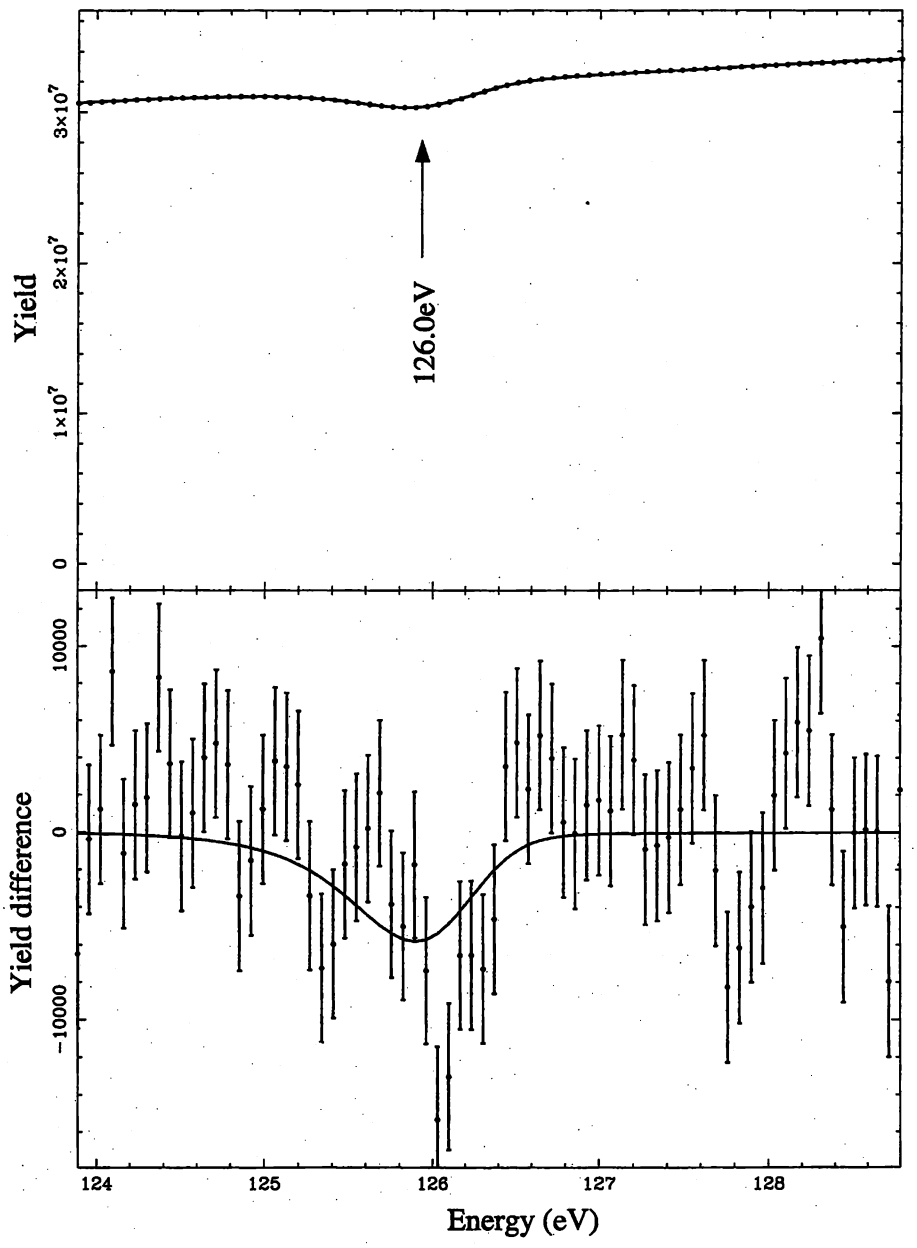

Figure B.9: The spectrum around the 126.0-eV resonance. This analysis gives an asymmetry with statistical significance of 3.0σ.

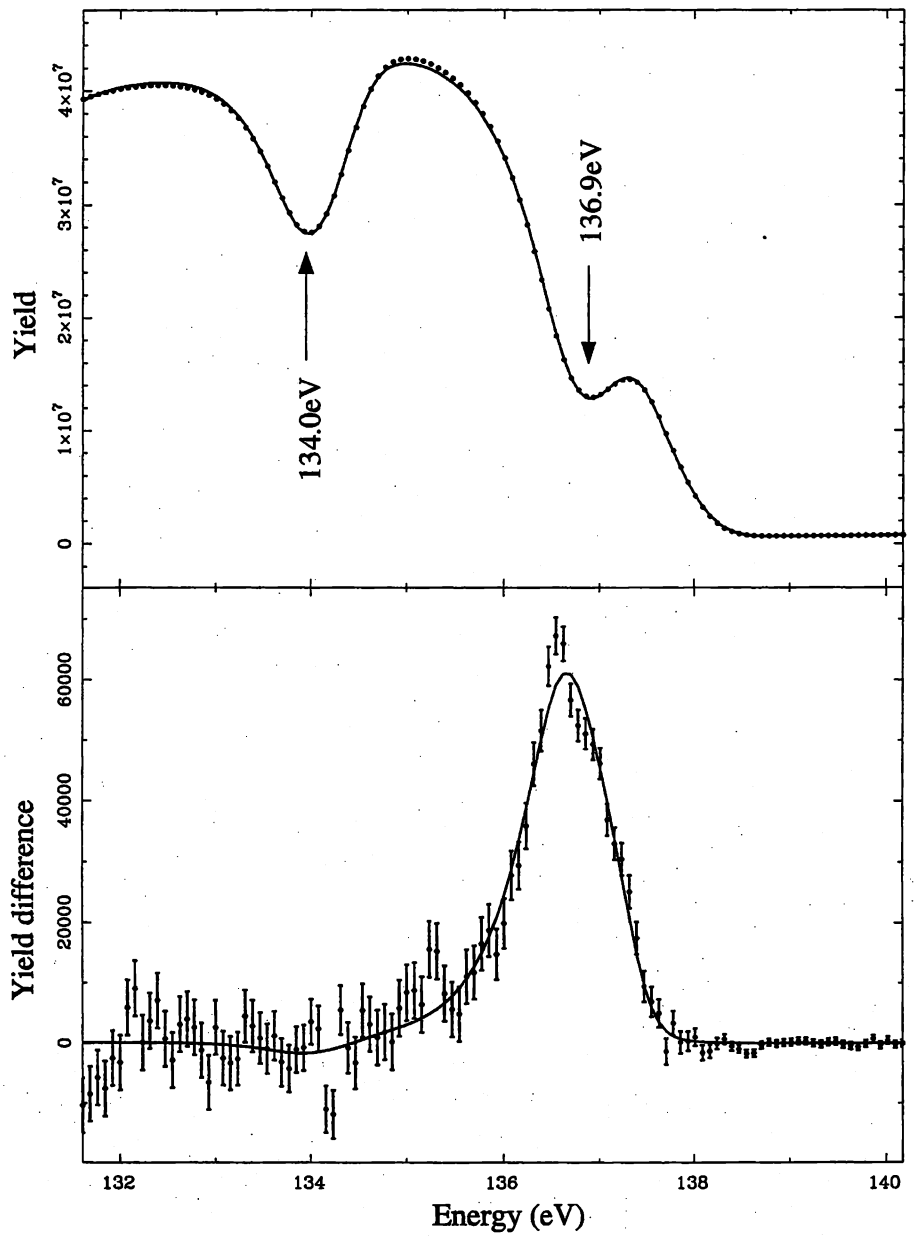

Figure B.10: The spectrum around the 134.0-eV and 136.9-eV resonances. The shape of neutron transmission spectrum is distorted by the neighboring 139.7-eV s-wave resonance of ^{127}I. The 136.9-eV resonance has large parity violating asymmetry whose statistical significance is larger than 46.2σ.

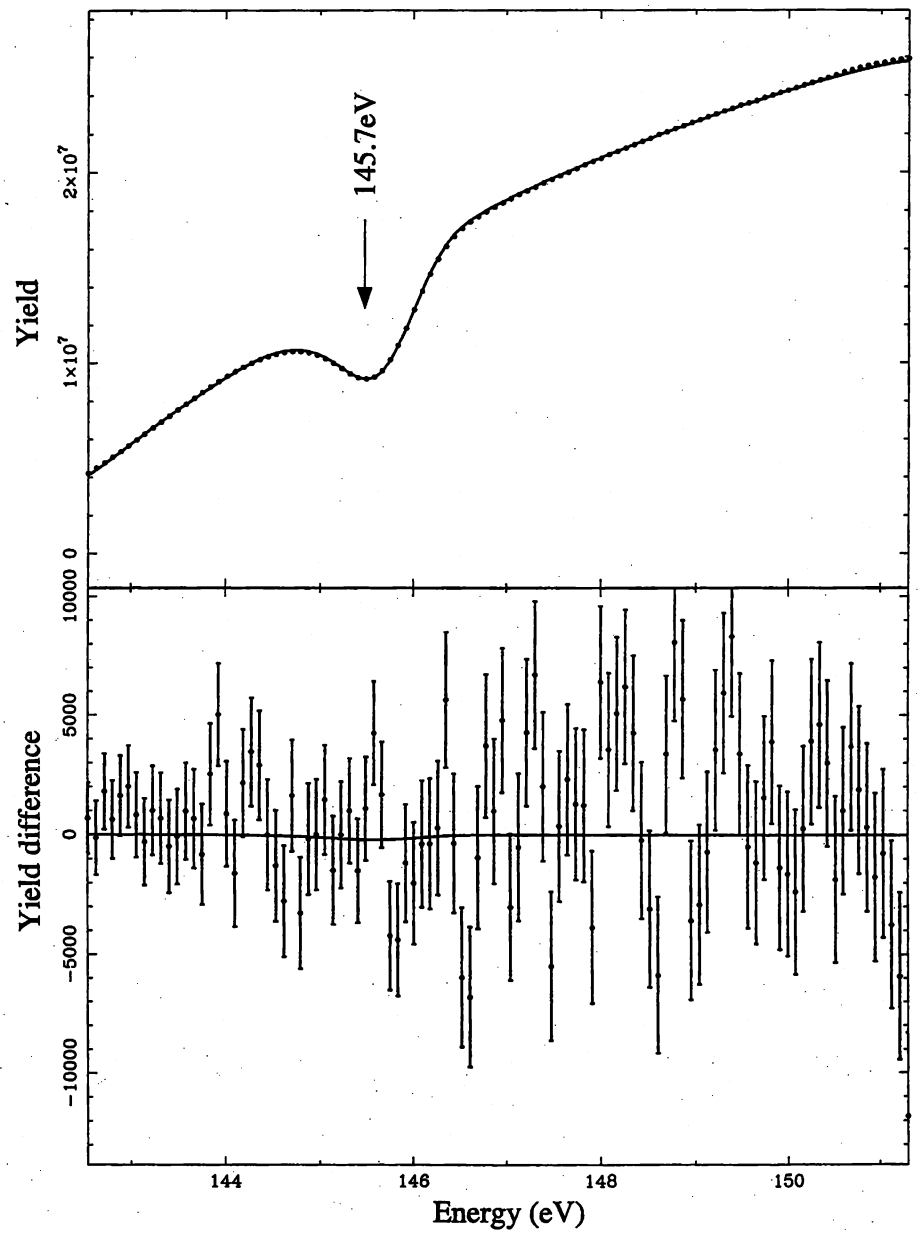

Figure B.11: The spectrum around the 145.7-eV resonance. The resonance shows no parity violating asymmetry within statistical error

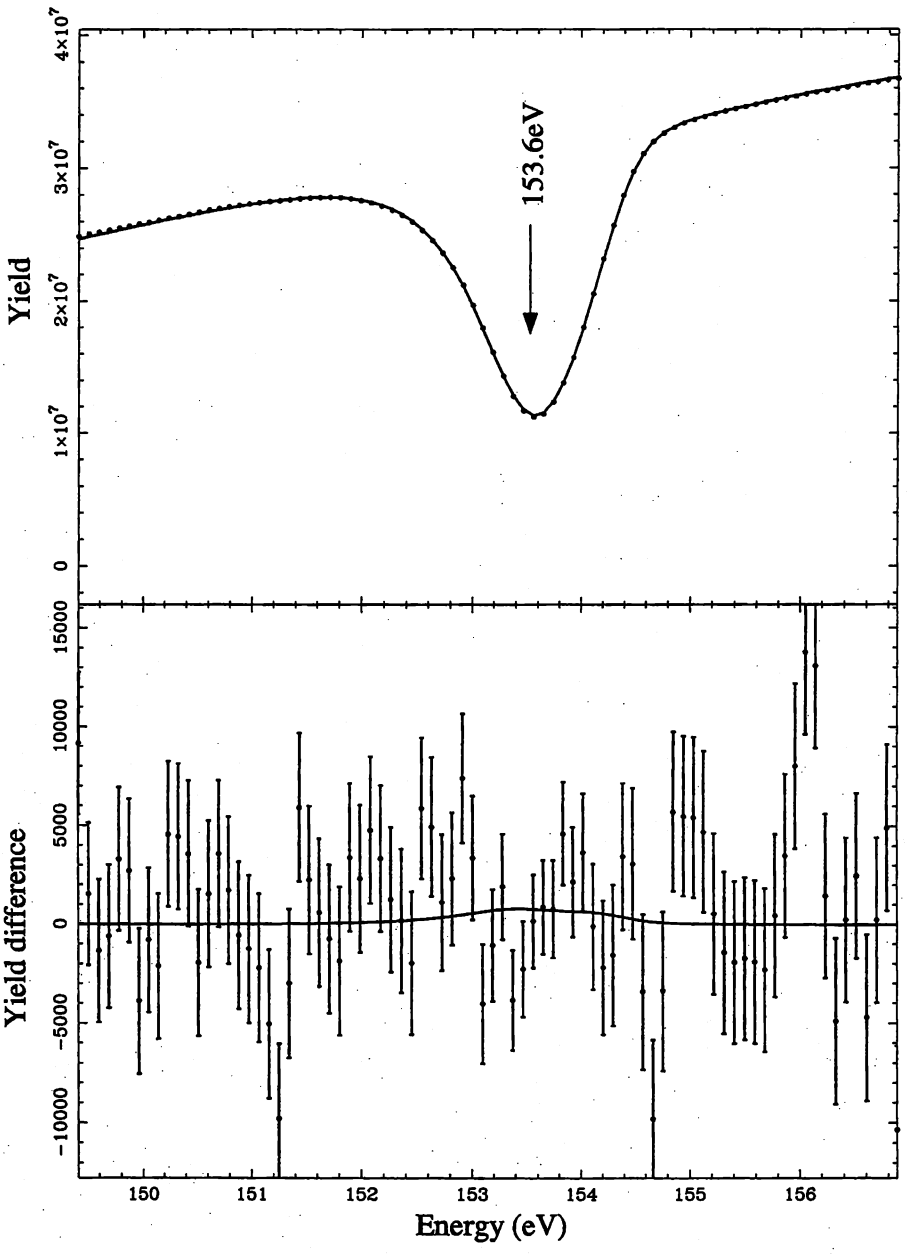

Figure B.12: The spectrum around the 153.6-eV resonance. The resonance shows no parity violating asymmetry within statistical error.

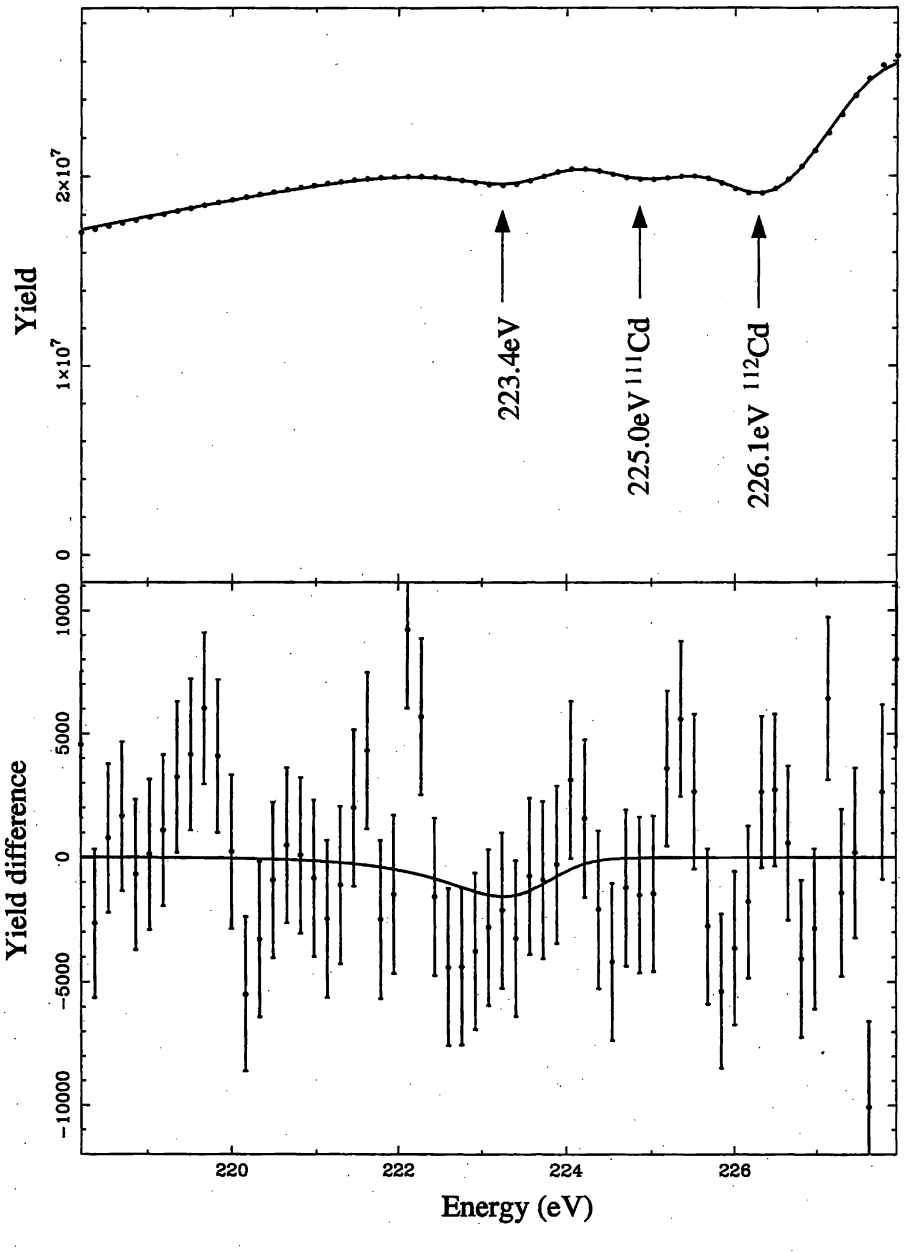

Figure B.13: The spectrum around the 223.4-eV resonance. The shape of spectrum is distorted by the neighboring resonances of ^{111}Cd and ^{112}Cd. The 223.4-eV resonances show no parity violating asymmetry within statistical error.

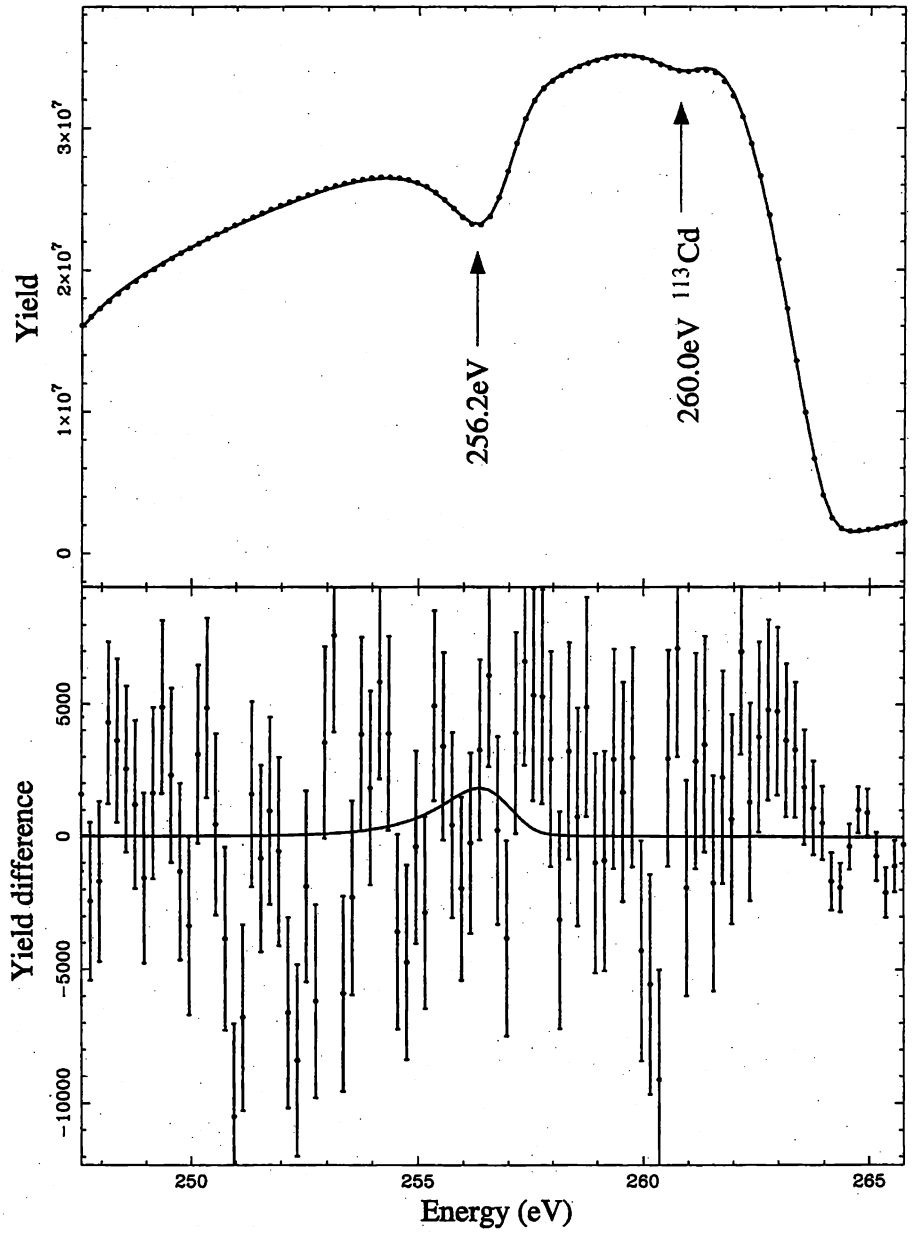

Figure B.14: The spectrum around the 256.2-eV resonance. The resonance shows no parity violating asymmetry within statistical error.

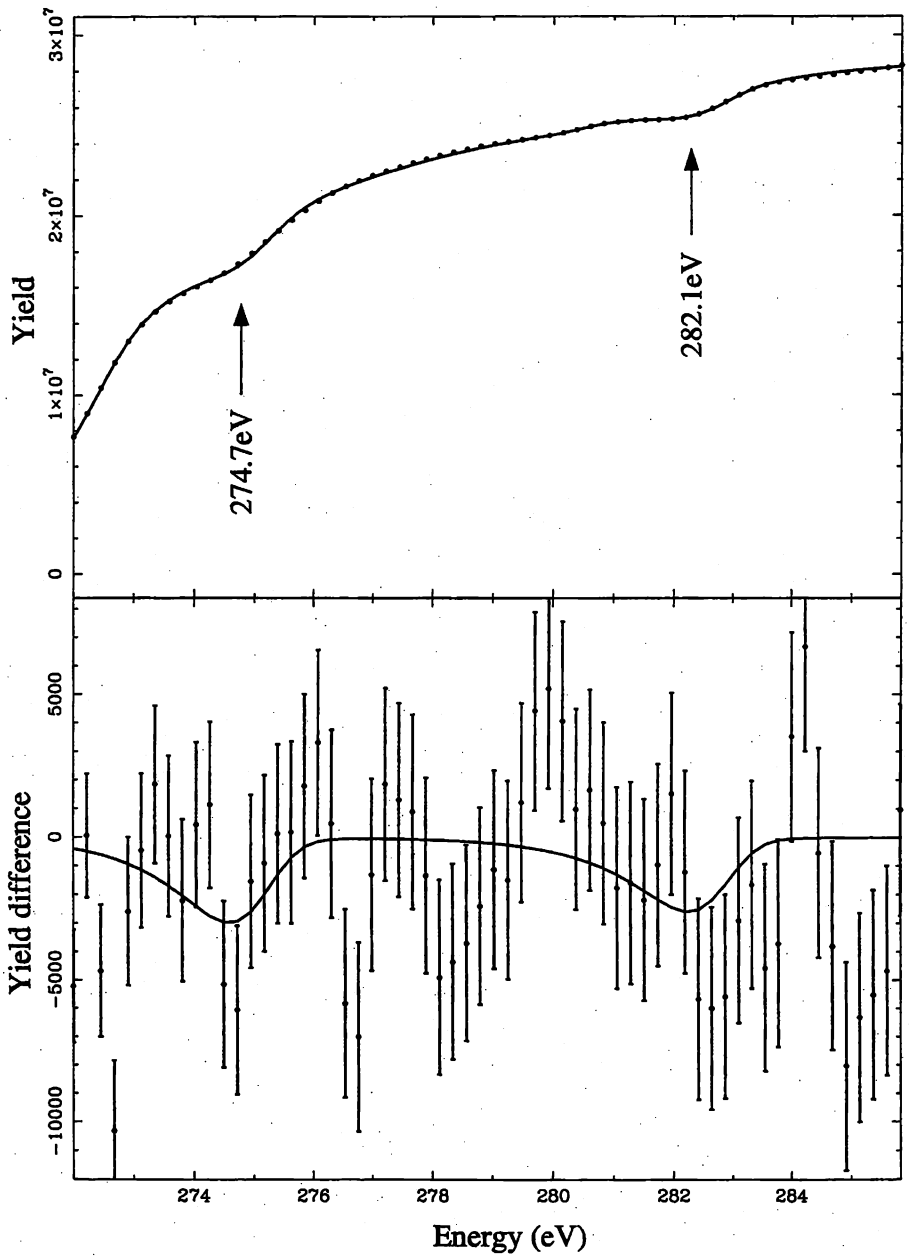

Figure B.15: The spectrum around the 274.7-eV and 282.1-eV resonances. Both resonances shows no parity violating asymmetry within statistical error.

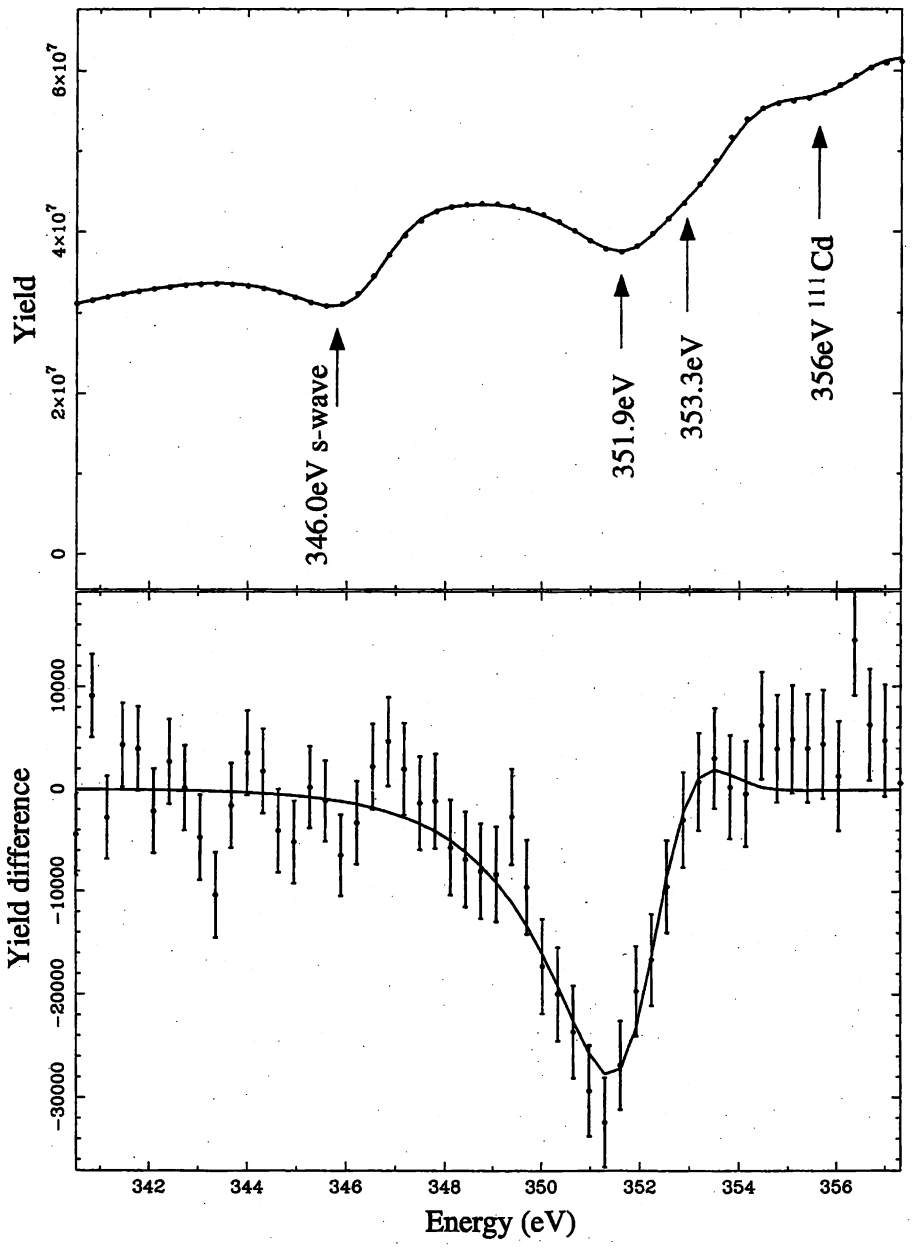

Figure B.16: The spectrum around the 351.9-eV and 353.3-eV resonances. Two resonances are overlapping in the neutron transmission spectrum (shown in upper graph), but the difference of the transmission spectra shows that the 351.9-eV resonance has a large asymmetry whose significance is 8.4σ whereas the 353.3-eV resonance has no asymmetry within statistical error.

Bibliography

[1] C. Wu *et al.*, Physical Review **105**, 1413 (1957).

[2] F. Michel, Physical Review **B133**, B329 (1964).

[3] B. McKellar and P. Pick, Physical Review **D7**, 260 (1973).

[4] M. Konuma, K. Ohta, T. Oka, and Y. Yamamoto, Supplement of the Progress of Theoretical Physics **60**, 203 (1976).

[5] B. Desplanques, J. Donoghue, and B. Holstein, Annals of Physics **124**, 449 (1980).

[6] V. Dubovik and S. Zenkin, Annals of Physics **172**, 100 (1986).

[7] N. Kaiser and G. Meissner, Nuclear Physics **A510**, 699 (1990).

[8] G. Feldman, G. Crawford, J. Dubach, and B. Holstein, Physical Review **C43**, 863 (1991).

[9] D. Kaplan and M. Savage, Nuclear Physics **A556**, 653 (1993).

[10] E. Henley, W.-Y. Hwang, and L. Kisslinger, Physics Letters **B367**, 21 (1996).

[11] V. Lobashov *et al.*, Nuclear Physics **A197**, 241 (1972).

[12] J. Potter *et al.*, Physical Review Letters **33**, 1307 (1974).

[13] D. Nagle *et al.*, in *The 3rd International Symposium on High Energy Physics with Polarized Beam and Polarized Targets*, Vol. 51 of *AIP Conference Proceedings* (AIP, New York, 1978), p. 224.

[14] R. Balzer *et al.*, Physical Review **C30**, 1409 (1984).

[15] S. Kistryn *et al.*, Physical Review Letters **58**, 1616 (1987).

[16] V. Yuan *et al.*, Physics Review Letters **57**, 1680 (1986).

[17] J. Alberi *et al.*, Canadian Jornal of Physics **66**, 542 (1988).

[18] V. Knyazkov *et al.*, Nuclear Physics **A417**, 209 (1984).

[19] S. Page *et al.*, Physical Review **C35**, 1119 (1987).

[20] M. Bini, T. Fazzini, G. Poggi, and N. Taccetti, Physical Review **C38**, (1988).

[21] E. Adelberger *et al.*, Physical Review **C27**, 2833 (1983).

[22] K. Elsener *et al.*, Nuclear Physics **A461**, 579 (1987).

[23] E. Earle *et al.*, Nuclear Physics **A396**, 221c (1983).

[24] Y. Abov *et al.*, Physics Letters **12**, 25 (1964).

[25] V. Alfiminkov *et al.*, JETP Letters **35**, 51 (1982).

[26] Y. Masuda *et al.*, Hyperfine Interactions **34**, 143 (1987).

[27] Y. Masuda, T. Adachi, A. Masaike, and K. Morimoto, Nuclear Physics **A504**, 269 (1989).

[28] H. Shimizu *et al.*, Nuclear Physics **A552**, 293 (1993).

[29] C. Bowman, J. Bowman, and V. Yuan, Physical Review **C39**, 1721 (1989).

[30] O. Sushkov and V. Flambaum, Soviet Physics Uspekhi **25**, 1 (1982).

[31] V. Bunakov and V. Gudkov, Nuclear Physics **A401**, 93 (1983).

[32] V. Flambaum and O. Sushkov, Nuclear Physics **A412**, 13 (1984).

[33] H. Kasari and Y. Yamaguchi, Progress of Theoretical Physics **95**, 1145 (1996), and references in the paper.

[34] L. Stodolsky, Nuclear Physics **B197**, 213 (1982).

[35] L. Stodolsky, Physics Letters **B172**, 5 (1986).

[36] T. Maekawa *et al.*, Nuclear Instruments and Methods in Physics Research **A336**, 115 (1995).

[37] M. Iinuma, (1997), (private communication).

[38] C. Francle *et al.*, Physical Review Letters **67**, 564 (1991).

[39] C. Francle *et al.*, Physical Review **C46**, 779 (1992).

[40] X. Zhu *et al.*, Physics Review **C46**, 768 (1992).

[41] J. Bowman *et al.*, Physical Review Letters **68**, 780 (1992).

[42] N. Auerbach and J. Bowman, Physical Review **C46**. 2582 (1992).

[43] N. Auebach, J. Bowman, and V. Spevak, Physical Review Letters **74**, 2638 (1995).

[44] V. Flambaum and G. Gribakin, Progress in Particle and Nuclear Physics **35**, 1 (1995).

[45] B. Desplanques and S. Noguera, Nuclear Physics **A598**, 139 (1996).

[46] V. Flambaum and O. Sushkov, Nuclear Physics **A435**, 352 (1985).

[47] J. Vanhoy, E. Bilpuch, J. J.F. Shriner, and G. Mitchell, Zeitschrift fur Physik **A331**, 1 (1988).

[48] Y. Matsuda, Master's thesis, Kyoto University, 1992, (in Japanese).

[49] T. Adachi *et al.*, Nuclear Physics **A577**, 433c (1994).

[50] V. Alfimenkov *et al.*, Soviet Journal of Nuclear Physics **52**, 589 (1990).

[51] L. Smotritsky and V. Dobrynin, in *Neutron Spectroscopy, Nuclear Structure, Related Topics*, JINR (JINR, Dubna, Russia, 1994).

[52] J. Bowman and E. Sharapov, in *Time Reversal Invariance and Parity Violation in Neutron Reactions*, edited by C. Gould, J. Bowman, and Y. Popov (World Scientific, Singapore, 1994), p. 8.

[53] J. Bowman, E. Sharapov, and L. Lowie, Physical Review **C53**, 285 (1996).

[54] M. Johnson, J. Bowman, and S. Yoo, Physical Review Letters **67**, 310 (1991).

[55] V. Flambaum and O. Vorov, Physical Review Letters **26**, 4051 (1993).

[56] V. Flambaum and O. Vorov, Physical Review **C51**, 1521 (1995).

[57] N. Auerbach, Physical Review **C45**, R514 (1992).

[58] N. Auerbach and O. Vorov, Physics Letters **B391**, 249 (1997).

[59] A. Michaudon and S. Wender, Los Alamos Report, LA-90-4355 (1990).

[60] P. Lisowski, C. Bowman, G. Russell, and S. Wender, Nuclear Science and Engineering **106**, 208 (1990).

[61] S. Penttila *et al.*, in *High Energy Spin Physics*. No. 343 in *AIP Conference Proceedings*, edited by K. J. Heller and S. L. Smith (AIP, New York, 1994), p. 532.

[62] J. Bowman, S. Penttila, and W. Tippens, Nuclear Instruments and Methods in Physics Research **A369**, 195 (1996).

[63] Y.-F. Yen *et al.*, in *Time Reversal Invariance and Parity Violation in Neutron Reactions* (World Scentific, Singapore, 1994), p. 210.

[64] S. Mughabghab, M. Divadeenam, and N. Holden, *Neutron Cross Sections* (Academic Press, New York, 1988), Vol. 1A and 1B.

[65] C. Porter, *Statistical Theries of Spectra-Flactuations* (Academic Press, New York, 1965).

[66] M. Metha, *Random Matrix - Revised and Enlarged, 2nd Edition* (Academic Press, New York, 1991).

[67] J. Vanhoy, J. J.F. Shriner, E. Bilpuch, and G. Mitchell, Zeitschrift fur Physik **A333**, 229 (1989).

[68] G. Lawrence *et al.*, in *Proc. of International Collaboration on Advanced Neutron Sources IX* (Swiss Institute for Nuclear Research, Switzerland, 1986), p. 85.

[69] G. Russell *et al.*, in *Proc. of International Collaboration on Advanced Neutron Sources IX* (Swiss Institute for Nuclear Research, Switzerland, 1986), p. 177.

[70] G. Russell *et al.*, in *Proc. of International Collaboration on Advanced Neutron Sources X* (Institute of Physics, New York, 1988), Vol. 97, p. 483.

[71] N. Roberson *et al.*, Nuclear Instruments and Methods in Physics Research **A326**, 549 (1993).

[72] J. Szymanski *et al.*, Nuclear Instruments and Methods in Physics Research **A340**, 564 (1994).

[73] V. Lushchikov, Y. Taran, and F. Shapiro, Soviet Journal of Nuclear Physics **10**, 669 (1970).

[74] S. Hiramatsu *et al.*, Journal of the Physical Society of Japan **45**, 949 (1978).

[75] S. Ishimoto *et al.*, Japanese Journal of Applied Physics **25**, 246 (1986).

[76] Y. Taran and F. Shapiro, Soviet Physics JETP **17**, 1467 (1963).

[77] N. Hoshizaki and A. Masaike, Japanese Journal of Applied Physics **25**, 244 (1986).

[78] D. Marquardt, Journal of the Society for Industrial and Applied Mathematics **11**, 431 (1963).

[79] L. Y. Lowie, Ph.D. thesis, North Carolina State University, 1996.

[80] S. Stephenson, Ph.D. thesis, North Carolina State University, 1996.

[81] C. Reich and M. Moore, Physical Review **111**, 929 (1958).

[82] BNL Report, BNL-NCD-17541 (1991).

[83] T. Nakagawa *et al.*, J. Nucl. Sci. Technol. **32**, 1259 (1995).

[84] P. Koehler, Nuclear Instruments and Methods in Physics Research **A350**, 511 (1994).

[85] Y.-F. Yen, E. Pitcher, and J. Bowman (unpublished).

[86] A. Gilbert and A. Cameron, Canadian Journal of Physics **43**, 1446 (1965).

[87] T. von Egidy, H. Schmidt, and A. Behkami, Nuclear Physics **A481**, 189 (1988).

[88] B. E. Crawford, Ph.D. thesis, Duke University, 1997.

[89] J. Szymanski *et al.*, Physical Review **C53**, R2576 (1996).

[90] A. Popov and G. Samosvat, in *Nuclear Data for Basic and Applied Science*, edited by P. Young *et al.* (Gordon and Breach, New York, 1986), p. 621.

[91] A. Popov and G. Samosvat, Soviet Journal of Nuclear Physics **45**, 944 (1987).

[92] L. Mitsyna, A. Popov, and G. Samosvat, in *Nuclear Data for Science and Technology*, edited by S. Igarashi (JAERI, Tokai, Japan, 1988), p. 111.